Summer 2014

Design of Optical Access for the Application of Laser Doppler Velocimetry in a Low Specific Speed Centrifugal Compressor

Bryce Ashton Heckaman
Purdue University

Recommended Citation

Heckaman, Bryce Ashton, "Design of Optical Access for the Application of Laser Doppler Velocimetry in a Low Specific Speed Centrifugal Compressor" (2014). *Open Access Theses*. 436.
https://docs.lib.purdue.edu/open_access_theses/436

Graduate School ETD Form 9
(Revised 01/14)

PURDUE UNIVERSITY
GRADUATE SCHOOL
Thesis/Dissertation Acceptance

This is to certify that the thesis/dissertation prepared

By Bryce Ashton Heckaman

Entitled
DESIGN OF OPTICAL ACCESS FOR THE APPLICATION OF LASER DOPPLER VELOCIMETRY IN A LOW SPECIFIC SPEED CENTRIFUGAL COMPRESSOR

For the degree of Master of Science in Mechanical Engineering

Is approved by the final examining committee:

Nicole Key

Eckhard Groll

Jun Chen

To the best of my knowledge and as understood by the student in the *Thesis/Dissertation Agreement. Publication Delay, and Certification/Disclaimer (Graduate School Form 32)*, this thesis/dissertation adheres to the provisions of Purdue University's "Policy on Integrity in Research" and the use of copyrighted material.

Approved by Major Professor(s): Nicole Key

Approved by: David C. Anderson 06/16/2014

Head of the Department Graduate Program Date

DESIGN OF OPTICAL ACCESS FOR THE APPLICATION OF LASER DOPPLER VELOCIMETRY IN A LOW SPECIFIC SPEED CENTRIFUGAL COMPRESSOR

A Thesis

Submitted to the Faculty

of

Purdue University

by

Bryce Ashton Heckaman

In Partial Fulfillment of the

Requirements for the Degree

of

Master of Science in Mechanical Engineering

August 2014

Purdue University

West Lafayette, Indiana

ACKNOWLEDGEMENTS

I would first and foremost like to thank my advisor Prof. Nicole Key, for this valuable research opportunity she has provided me. I appreciate Prof. Eckhard Groll and Prof. Jun Chen for serving on my advisory committee. I want to thank Rolls-Royce and specifically Mark Whitlock for their financial support and guidance, which made this research possible. A special thanks to Scott Meyer and Rob McGuire at Zucrow for the mechanical advice and expertise they provided me. I am very grateful for the technical assistance and guidance offered by John Fabian throughout this project. And of course, I am thankful to my lab mates: Reid, Evan, Patrick, Natalie, Bill, and Lou for all of their friendship and advice. I especially would like to thank Dave for being a wonderful office mate over the last two years and Nick for his motivation and also his computational resources that have made this research possible. I would like to express my gratitude to my climbing buddy Jeanne for all of our weekend adventures together. A huge thanks goes out to Matt for the many exploits we have shared together, both inside and outside of the lab. I want to thank my parents Lynn and Kathy, and my sisters Alayna and Emmy for all of the support and encouragement they have always provided me. Finally, I am truly thankful to Theresa for all of her love and support. She has been with me when times were easy and when times were difficult. I would not have been able to do this without her.

TABLE OF CONTENTS

Page

Page

Page

LIST OF TABLES

Table Page

LIST OF FIGURES

Figure Page

Figure Page

Figure Page

Figure Page

NOMENCLATURE

Symbol	**Description**
AC	Alternating Current
ϕ	Angle normal to flow path
θ	Beam angle
D_L	Beam diameter
r_{mean}	Bolt circle radius
CPM	Central Processing Module
CSTAR	Centrifugal Stage Aerodynamic Research
Δz	Change in axial deflection
$\Delta r'$	Change in radial deflection
$\Delta r'$	Change in tip clearance deflection
CEESI	Colorado Engineering Experiment Station Inc.
CFD	Computational Fluid Dynamics
ρ	Density
d	Diameter
DEHS	Di-ethyl-hexyl-sebacate
dP	Differential pressure
DSA	Digital Sensor Array

Symbol	**Description**
DC	Direct Current
C_d	Discharge Coefficient
ε	Expansion factor
FEA	Finite Element Analysis
V	Flow velocity
a	Fluid acceleration
F	Focal length
FLA	Forward Looking Aft
FM	Frequency Modulation
δ_f	Fringe spacing
gpm	Gallons per minute
R	Gas constant
HP	Horsepower
ips	Inches per second
LDV	Laser Doppler Velocimetry
L2F	Laser-2-Focus
M	Mach number
$\dot{m}$	Mass flow rate
MHD	Max Hot Day
N_f	Number of fringes
ρ_p	Particle density
d_p	Particle diameter

Symbol	**Description**
U_p	Particle velocity
t_{plane}	Plane stress width
A_{plenum}	Plenum cross-sectional area
PSL	Polystyrene Latex
δ	Probe volume diameter
γ	Ratio of specific heats
K	Resistance coefficient
rpm	revolutions per minute
Re	Reynolds number
RMS	Root Mean Square
P	Static pressure
T	Static temperature
TDC	Top Dead Center
P_o	Total pressure
U_s	Velocity lag
U	Velocity of fluid
μ	Viscosity
λ	Wavelength
l	Wire opening length

ABSTRACT

Heckaman, Bryce A. M.S.M.E., Purdue University, August 2014. Design of Optical Access for the Application of Laser Doppler Velocimetry in a Low Specific Speed Centrifugal Compressor. Major Professor: Dr. Nicole Key, School of Mechanical Engineering.

The objective of this research has been to design optical access for the application of laser Doppler velocimetry (LDV) in a low specific speed centrifugal compressor. The ability to acquire non-intrusive flow measurements will provide valuable insight into tip leakage flow, secondary flow, and impeller/diffuser interactions within the centrifugal compressor. The current research facility houses a new low specific speed centrifugal compressor which design is based off a compressor that would be installed as the last stage of a high-pressure compressor.

The LDV optical access has been designed and includes two fused silica windows that are housed in stainless steel holders and conform to the flow path of the compressor shroud. The two windows will allow three-component velocity measurements of 85% of the impeller flow path, the vaneless space, and two vaned diffuser passages. Finite element analysis (FEA) was performed in ANSYS to validate the stress and deflection of the shroud for the new window design. A manufacture has been selected to fabricate the window assemblies.

In addition to the design of the LDV optical access, several improvements have been made to the existing facility. Such improvements include the development of the facility oil system, the design of a new inlet plenum, and installation of the newly acquired centrifugal compressor. High precision measurement devices have also been adapted by the facility such as a long-form venturi, a high accuracy tip clearance measurement system, and a three-component LDV system. The current state of the facility has been documented. The design and capabilities of the research compressor have also been provided.

CHAPTER 1 : INTRODUCTION

1.1 Motivation

The gas turbine engine is a critical part of today's industry. It is used to power aircraft, trains, ships, electrical generators, and even tanks. Because of its large prevalence and application, this type of engine is constantly facing the need to change and adapt to customer demands. Currently, the design of modern gas turbine engines is driven by challenging requirements from consumers to provide higher performance at lower specific fuel consumption. To meet these requirements, a need exists for highly efficient compressors featuring higher overall pressure rises with larger power-to-weight ratios.

The performance of centrifugal compressors depends heavily on the fluid interactions occurring within the impeller and diffuser. Due to the high radial accelerations and tip leakage flows present in centrifugal compressors, these interactions are often complex and not well understood. Because of this, further research on the flow physics occurring inside these machines is critical to achieving higher overall efficiencies and wider operating ranges for centrifugal compressors. Accurate measurements of the flow field within the impeller and diffuser govern the development of the computational fluid models used by designers to predict compressor performance. These models allow engineers to produce more efficient and robust designs.

Several techniques have been developed to measure and characterize the flow inside of turbomachinery. These various measurement techniques can be classified as being either intrusive or non-intrusive. Intrusive flow measurement techniques consist of probes that are physically placed in the fluid and include instrumentation such as hot wires, rakes, and pitot probes. Unfortunately, the presence of an instrument in the flow will result in alterations to the flow field due to probe blockage. An example of this discrepancy was observed by Gizzi [1] when velocity measurements acquired with fast response pressure sensors at the exit of a centrifugal compressor impeller were influenced by resultant pressure fluctuations from vortex shedding off the probe. Another major disadvantage to the intrusive measurement technique is that it cannot be applied in areas with rotating machinery, such as inside an impeller blade passage. Fortunately, non-intrusive techniques have been developed that are better suited for these type of measurements.

Non-intrusive techniques, as the name might suggest, are methods of acquiring measurements without influencing the flow. Typically, these techniques utilize lasers to illuminate seeding particles to scatter light to receiving optics. Methods such as these are ideal for turbomachinery research because they can be applied within rotating passages and high temperature environments commonly found in compressors and turbines. Examples of non-intrusive measurement techniques include Laser-Doppler-Velocimetry (LDV), Laser-2-Focus-Velocimetry (L2F), and Particle-Image-Velocimetry (PIV). In the following sections, the application of both LDV and L2F in centrifugal compressors will be discussed.

1.2 Laser Doppler Velocimetry (LDV)

Laser Doppler velocimetry, also known as laser Doppler anemometry (LDA), is a point measurement technique that provides non-intrusive transient velocity data. It utilizes the Doppler shift resulting from the superposition of two light waves of different frequencies to obtain velocity measurements in the flow field. The implementation of LDV is sometimes difficult when geometrically complex optical access is introduced due to the tendency of light waves to refract or alter direction with changes in its transmission medium. This can be overcome with proper alignment and calibration of the measurement volume location, however. LDV systems can be purchased commercially and applied to a wide range of applications.

Figure 1.1 illustrates the intersection of two LDV lasers, each of equal frequency. The space generated at the crossing of the two beams is known as the measurement volume. The intersection of the two incident beams creates a fringe pattern of alternating low and high intensity light. The distance between the fringe peaks is constant and the value known. When a seed particle passes through the measurement volume, light is scattered back to a photodetector to generate a signal burst with intensities that fluctuate depending on the fringe intensity. When passed through a bandpass frequency filter, the frequency of this sinusoidal signal is measured. Because the intensity of the signal corresponds to the fringe spacing, the velocity of the seed particle can be calculated taking the product of the known fringe spacing and the measured signal frequency.

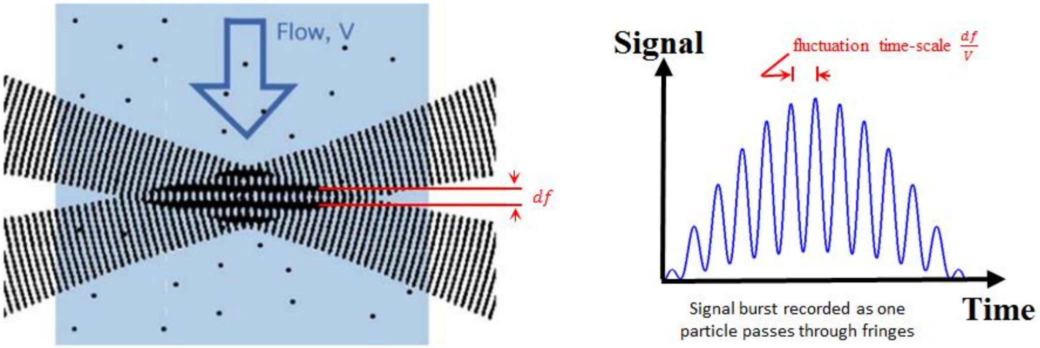

Figure 1.1: Fringe model produced by crossing two beams and the burst signal produced by a seed particle passing through the measurement volume, adapted from [2].

One problem with this set up, however, is that there exists an ambiguity in the direction of the fluid particle velocity since a particle with a negative velocity will produce the same Doppler frequency as a particle with positive velocity. Therefore, only the absolute velocity can be measured. This ambiguity, however, can be removed by shifting the frequency of one of the beams. By shifting the frequency slightly, the fringe pattern will appear to move. Figure 1.2 illustrates an LDV probe that utilizes frequency shifted beams, and Figure 1.3 depicts the resultant fringe pattern. When a seed particle travels through the measurement volume, the burst signal produced will be a combination of the particle velocity and the fringe velocity. Since the direction and magnitude of the fringe velocity is known, the direction of the fluid particle can be determined.

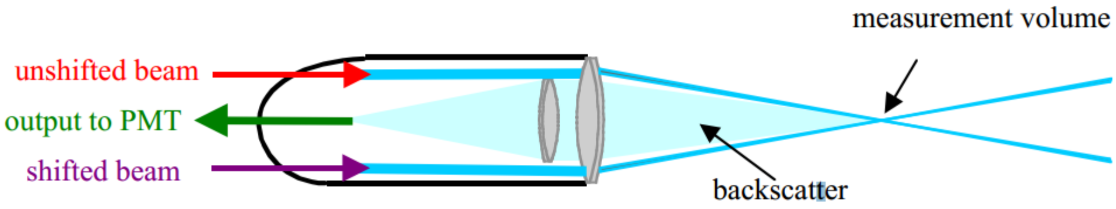

Figure 1.2: Laser Doppler anemometry probe with a shifted beam, from [2].

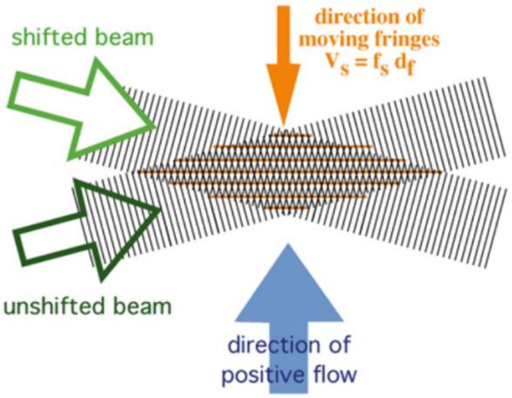

Figure 1.3: Directional ambiguity removed using Doppler shifting, from [2].

The location of the receiving optics depends on the method of scattering used. Forward scattering requires the photodetector to be positioned directly opposite of the beam source. This method is less common due to limited optical access and the need to align the photodetector with the transmitting optics. Back scattering is often the chosen alternative for LDV applications. This method integrates the photodetector with the beam source, removing the need to align the receiving and transmitting optics every time the LDV system is set up. It also considerably reduces the space required for set up as well as the need to provide optical access for two probes.

Multi-dimensional measurements are possible if the setup incorporates additional pairs of beams. This can be accomplished by utilizing multiple probes or probes that emit more than one set of beams. Probes that emit two sets of beams can resolve two components of velocity in the flow field. When paired with a 1D probe, all three components of velocity can be obtained. This set up requires precise knowledge of each probe's position relative to the other and the probe volume location to accurately transform each velocity component to a meaningful coordinate system. The probes also need to be angularly offset by a significant distance, normally at least 30 degrees, to reduce the error in resolving the three velocity components. This requires an increase in the size of the optical access to accommodate both beams. Due to the additional expense for equipment and the time-consuming nature of alignment and realignment of the probes, three-component LDV is not as common as two-component LDV.

1.3 Laser-2-Focus Velocimetry

As mentioned previously, laser-2-focus (L2F) is another widely accepted laser-based non-intrusive measurement technique. Because of its close ties to laser Doppler velocimetry, it's worth mentioning here.

The L2F technique is very similar to LDV in that it utilizes the incident light scattered by seeding particles in a flow field to obtain velocity measurements. However, instead of relying on the Doppler shift of the fringe pattern generated by crossing two laser beams, L2F uses a beam splitter to produce two parallel beams that are then focused to create two adjacent spots that are a known distance apart, refer to Figure 1.4 for a depiction of an L2F anemometer probe that would produce these two parallel beams. Figure 1.5 illustrates an exaggerated view of the two parallel probe volumes generated by L2F. The thinnest section of the beam marks its focal point. When seeding particles pass through each spot, the time between each burst of scattered light is measured and used to calculate a component of the particle's velocity. To obtain the magnitude and direction of flow at the measurement location, the L2F probe is typically rotated about its optical axis, and the measurement is repeated. The data collected are then used to produce a histogram of the velocity measurements and flow angles. The peak value of this distribution represents the average velocity magnitude and flow angle.

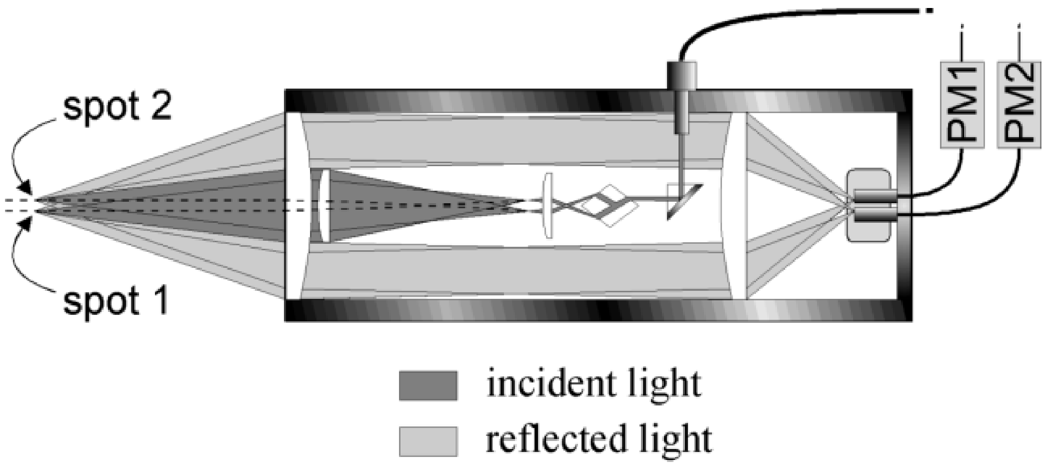

Figure 1.4: Laser-2-Focus anemometer probe model, from [3].

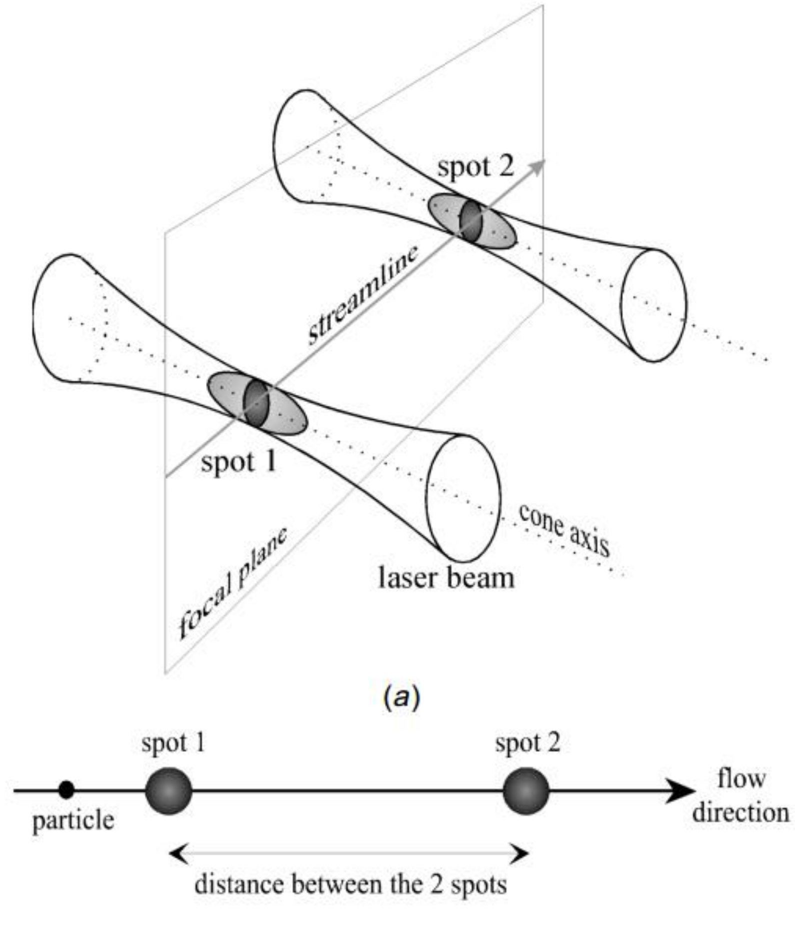

Figure 1.5: Depiction of L2F measurement volume, from [3].

Though this method results in a much higher signal-to-noise ratio than LDV, false signals can be produced by seeding particles that do not travel in the plane of the two beams. For this reason, the application of L2F in highly turbulent flows where the lateral mean velocity components are large is very limited. It also means that a statistical method is required to remove the random noise that is generated by these non-planar particles resulting in a time-averaged measurement and lower sampling rate [4, 5].

1.4 Seeding Particles for Laser-Based Anemometry

It is important to point out that laser velocimetry is not completely non-intrusive. In situations when the number of visible particles in the flow is insufficient to act as tracers, it is common to artificially seed the flow field to sufficiently scatter light back to the receiving optics for measurement. Unfortunately, this results in an indirect measurement of the fluid velocity as the optics are actually measuring the particle velocity. One common source of error is the influence that gravity has on the seeding when the particle density, $\rho_{P,}$ is different from the fluid density, ρ. Particle lag is another source of discrepancy when using seeding particles. In continuously accelerating fluid, the velocity lag of a particle and be shown by:

$$U_s = U_p - U = \frac{d_p^2(\rho_P - \rho)}{18\mu}\boldsymbol{a}, \tag{1.1}$$

where U_P is the particle velocity, U is the fluid velocity, μ the dynamic viscosity, d_P the particle diameter, and $\boldsymbol{a}$ the acceleration of the fluid. This expression would indicate that particles with smaller diameters have less induced drag and, therefore, would be best suited for flow seeding. However, if the particle is too small, then the light scattered back to the receiving optics is insufficient to measure the particle velocity. The amount of light scattered by small particles is dependent on the ratio of the refractive index of the particles to that of the surrounding medium and the particles size, shape, and orientation. Therefore, a compromise between the lag of the particle and its ability to scatter light is needed when choosing seeding particles.

In addition, the seed particle must be appropriately chosen to suit the measurement environment. For example, liquid seeding that is suitable for a low-temperature application may evaporate in a high-temperature application. Solid particles may be more suitable for high-temperature applications, but they tend to agglomerate and are often difficult to disperse. Another consideration is the rate at which the particles are introduced. If the flow is not sufficiently seeded, then the number of particles passing through the measurement volume will be reduced resulting in a limited number of measurements. On the other hand, if the flow contains too many particles, the optical access may become obstructed, preventing the transmitting optics from producing a measurement volume.

Seeding in gas flows is typically more difficult than liquid flows because there is a significant difference in density between the gas and the seed particle. Typically, particles around 1 µm in diameter are chosen for gas seeding and are commonly oil or Di-ethyl-hexyl-sebacate (DEHS) particles. Table 1.1 lists materials that are commonly used as seeding for gas flows. The introduction of seed particles in gas flows can be accomplished in several ways. Dry powders can be dispersed in fluidized beds or air jets. Liquids may be evaporated or atomized into droplets. Atomizers can also be used to inject solid particles or tiny droplets of liquids of high vapor pressure that have been mixed with lower vapor pressure liquids such as water-ethanol that will evaporate before entering the test section. A number of resources for more detailed information on LDV and seeding for laser-based measurements are available [6, 7, 8].

For high-temperatures applications as found in centrifugal compressors, solid seeding particles are preferred. Wernet et al. [9] demonstrated the use of alumina/ethanol dispersion for seeding in a 4:1 pressure ratio centrifugal compressor with a design rotational speed of 21,789 rpm and mass flow rate of 4.5 kg/s. The compressor inlet and exit tip diameters were 210 mm and 431 mm, respectively, and incorporated 15 main blades and 15 splitter blades with a back-sweep of 50˚. The author compared the use of alumina/ethanol with Polystyrene Latex (PSL) as a seeding material for two-component LDV measurements. The study found that due to its higher specific gravity, the alumina particles lagged the flow to a greater extent than the PSL particles. Despite its tendency to lag the flow, the alumina particles were able to withstand much higher temperatures than the PSL particles.

Table 1.1: Seeding materials for gas flows, adapted from [8].

Type	Material	Mean diameter in µm
Solid	Polystyrene	0.5 - 10
	Alumina Al_2O_3	0.2 - 5
	Titania TiO_2	0.1 - 5
	Glass micro-spheres	0.2 - 3
	Glass micro-balloons	30 - 100
	Granules for synthetic coatings	10 - 50
	Dioctylphathalate	1 - 10
	Smoke	< 1
Liquid	Different oils	0.5 - 10
	Di-ethyl-hexyl-sebacate (DEHS)	0.5 - 1.5
	Helium-filled soap bubbles	1000 - 3000

1.5 Applications of Laser Velocimetry in Centrifugal Compressors

LDV is a well-established non-intrusive measurement technique that has been widely used to study the complicated flow phenomena that occurs within centrifugal compressors. It has been around longer than other non-intrusive methods such as PIV.

In 1976, Eckardt [10] used L2F to characterize the flow field inside a high-speed centrifugal compressor impeller. The compressor consisted of an unshrouded impeller with 20 blades (no backsweep), and a tip clearance that varied from 0.8 mm to 0.25 mm due to centrifugal forces and thermal growth during operation. The impeller tip diameter was 400 mm and the compressor incorporated a vaneless diffuser to ensure that the flow throughout the impeller was undisturbed by impeller-diffuser interactions. The compressor operated at 14,000 rpm with a total pressure ratio of 2.1 and tip speeds up to 400 m/s. Eckardt's investigation obtained velocity measurements throughout the blade passages at five different measurement planes, Figure 1.6. The investigation revealed the onset of flow separation in the shroud/suction side corner of the impeller passage. This separation induced the growth of a wake along the suction side of the blade throughout the impeller passage. The secondary flow patterns resulted in non-uniform impeller discharge in the form of a jet/wake interaction. The development of this jet/wake phenomenon throughout the blade passage is depicted in Figure 1.7. At the inlet, the velocity distribution is nearly uniform; however, as the flow progresses through the blade passage, the growth of a wake is apparent. This study represents the first non-intrusive characterization of the jet/wake interaction following a previous investigation in 1975 by Eckardt [11] where the presence of the jet/wake was first found experimentally using hot-wire anemometry.

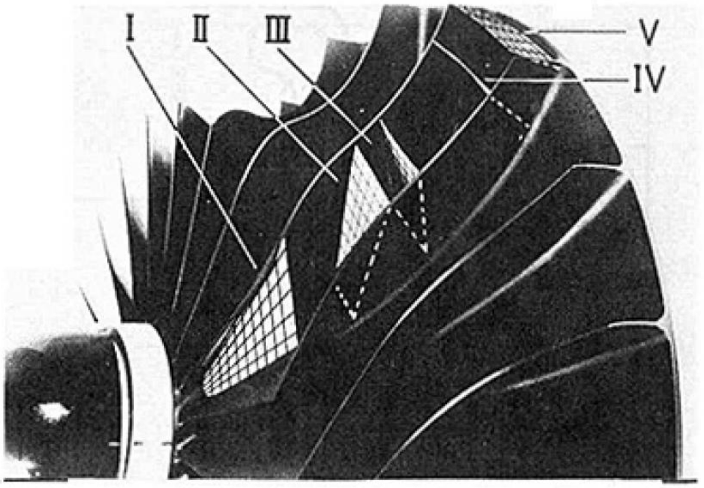

Figure 1.6: Centrifugal compressor impeller used in Eckardt's investigation with optical measurement planes throughout a blade passage, from [10].

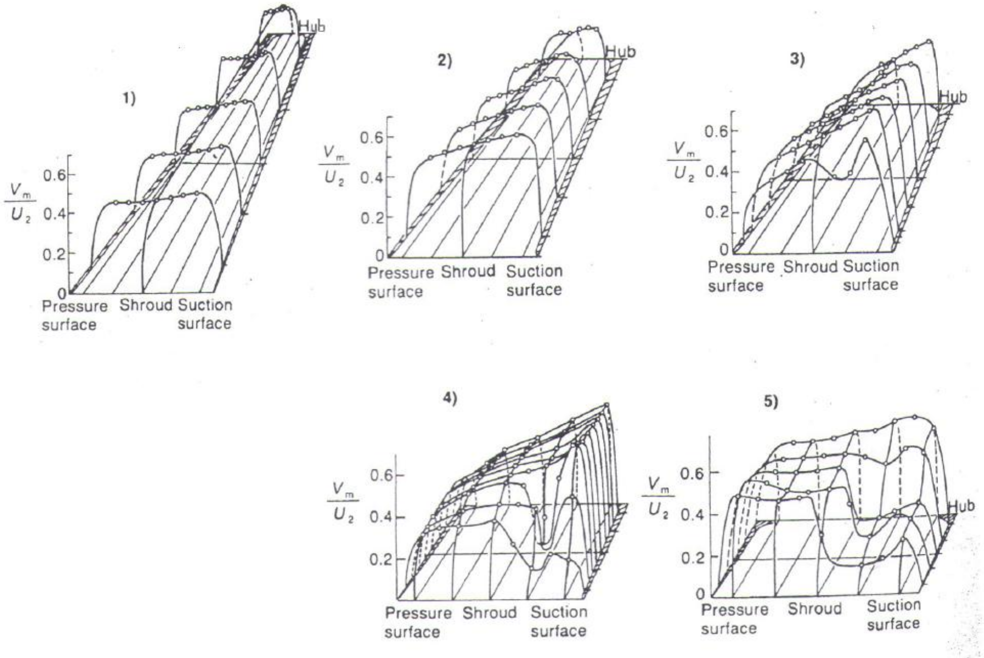

Figure 1.7: L2F velocity measurements by Eckardt in a radial impeller at five measurements planes in the blade passage, from [10].

In 1979, Adler et al. [12] investigated the flow inside of a shrouded backswept centrifugal impeller by employing LDV through a rotating window installed in the shroud disk.

Figure 1.8 depicts the impeller and location of the measurement surfaces. The impeller incorporated ten backswept blades and operated at a speed of 2,810 rpm with a volumetric flow rate of 0.288 m^3/s. The discharge from the impeller was delivered to an oversized volute to avoid upstream influence on the impeller. The compressor was seeded with a 15% (by mass) solution of NaCl in water. Results indicated a more uniform flow throughout the impeller passage and exit despite the presence of inlet distortion. It is believed that the reason for a lack of separation and induced wake zones is due to the absence of the low-momentum tip leakage flow for this shrouded impeller. Tip leakage flows are jets passing over the tops of the blades from pressure side to suction side. In addition, the absence of low-energy tip leakage flow into the blade passage may explain the more uniform discharge flow and absence of the jet/wake phenomena characterized by Eckardt [10].

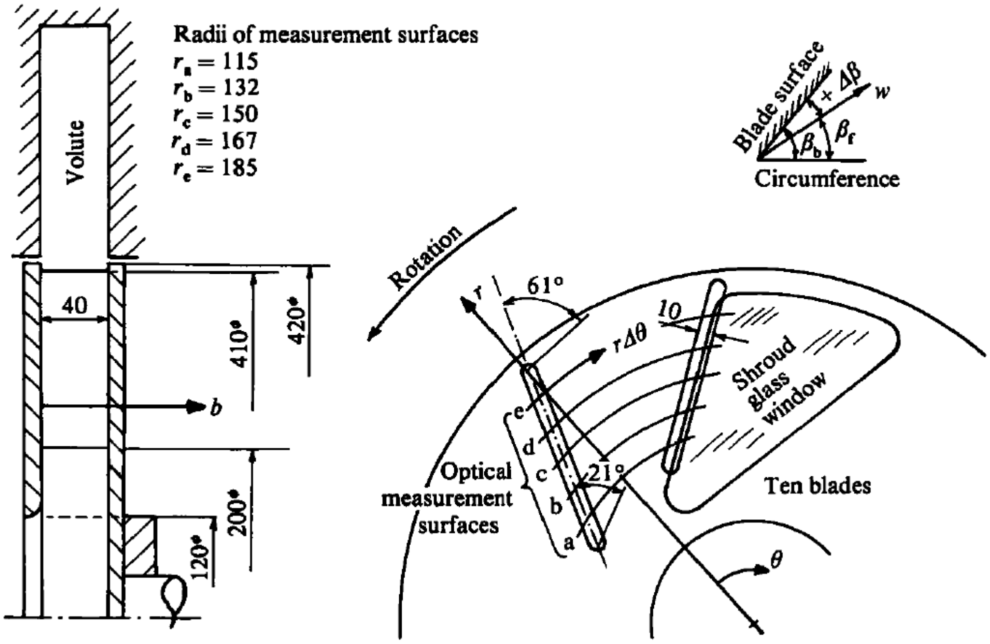

Figure 1.8: Depiction of Alder's closed backswept impeller and rotating window, from [12] (all dimensions in mm).

Measurements of the flow velocity in the vaneless diffuser of a high-speed centrifugal compressor were undertaken by Allos et al. [13] in 1980. The goal of this research was to study the flow field leaving the impeller and suggest how successful the impeller designer was at reducing diffuser inlet distortion. In particular, this project utilized the forward scattering LDV method and the natural seeding of the flow to define the flow conditions in a vaneless diffuser close to the tip of a backswept impeller. The compressor was fitted with a 101.6 mm diameter centrifugal impeller with 16 backswept blades. The test set up to acquire velocity measurements in the vaneless diffuser is depicted in Figure 1.9. Tests were carried out at two operating conditions; 63,000 rpm with blade tip speed of 335 m/s and 73,000 rpm with a blade tip speed of 388 m/s. The authors were able to successfully apply forward scattering LDV to define several blade-to-blade profiles at different radii in the diffuser. The flow analysis showed that the flow had a mean velocity of 400 m/s and varied at a rate up to 20 kHz. Unfortunately, the forward scattering method demonstrated here is not always feasible in turbomachinery applications due the requirement to provide optical access for both the transmitting and receiving optics.

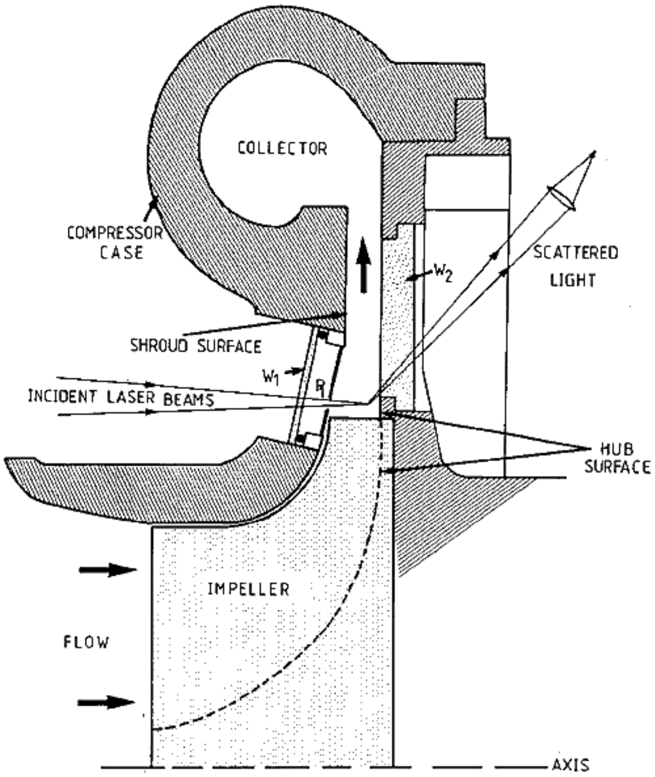

Figure 1.9: Forward scattering laser Doppler technique applied to a vaneless diffuser, from [13].

In 1980 Krain [14] used L2F to study the impeller and diffuser interactions in a centrifugal compressor. His experimental setup included a 400 mm diameter radial impeller with 28 blades, including 14 splitter blades, and both a vaneless and vaned diffuser. The vaned diffuser incorporated 27 wedge shaped vanes with a radius ratio of 1.1 (diffuser leading edge to impeller exit). His researched investigated the effects of the vaned diffuser on the upstream impeller flow field at 14,000 rpm and a mass flow rate of 5.8 kg/s. The investigation found weak influences of the vaned diffuser on the upstream rotor flow field as depicted by the velocity profiles in Figure 1.10. They attribute this is due to the vaned diffuser design, which featured a large diffuser leading edge/impeller exit radius ratio in addition to a low subsonic diffuser leading edge Mach number.

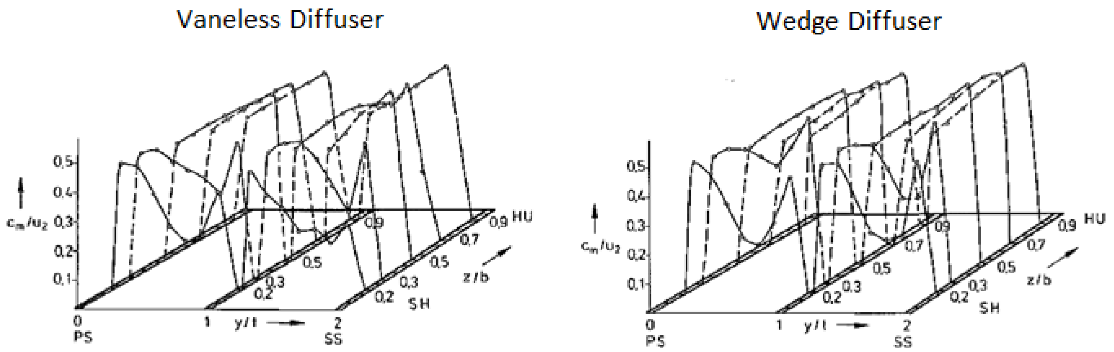
Vaneless Diffuser

Wedge Diffuser

Figure 1.10: L2F velocity measurements by Krain at the exit of a radial impeller, from [14].

Krain [15] also investigated the flow within a backswept impeller of a centrifugal compressor in 1988. The impeller consisted of 24 blades with 30˚ of backsweep. A constant area vaneless diffuser was located downstream of the impeller. Unlike Alder's [12] shrouded impeller design, this was an unshrouded impeller. He found the presence of distorted through-flow patterns and secondary flows within the impeller passage, presumably caused by a vortex flow. Despite the effect of these distorted vortex patterns on the overall rotor character, a relatively smooth velocity profile was identified at the impeller exit indicating that the effects had dissipated before the impeller discharge. Figure 1.11 illustrates this relatively uniform velocity profile at the exit of this backswept impeller. This demonstrates a deviation from the well-known jet/wake phenomena characterized in radial exit impellers by Eckardt [10] and Krain [14]. Uniform impeller exit flow is highly desirable in turbomachinery applications since it produces fewer losses and more predictable behavior when transitioning from the impeller to the diffuser.

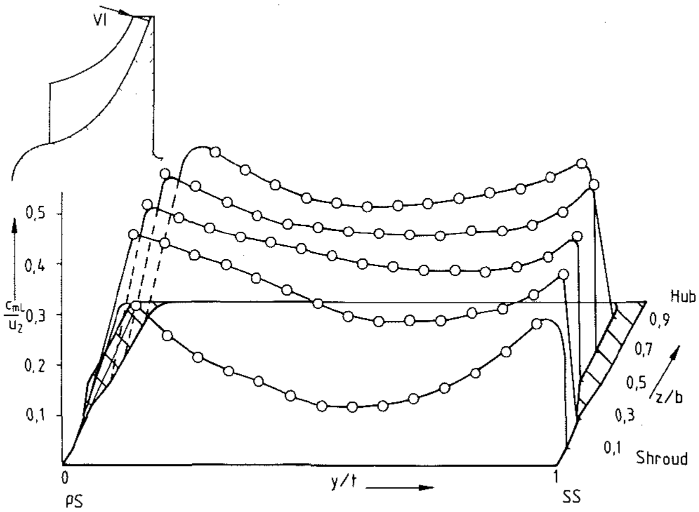

Figure 1.11: Velocity profile at the exit of a backswept impeller at design speed by Krain [15] ($\dot{m}$ = 4.0 kg/s).

A study utilizing LDV to characterize the difference in shrouded and unshrouded radial pump impellers was undertaken in 1987 by Hamkins et al. [16]. Measurements in shrouded and unshrouded versions of a radial pump were acquired at different locations and flow rates. The investigation revealed that the suction side channel wake region was significantly smaller in the unshrouded impeller when compared to the closed impeller. Also, the slip was higher in the unshrouded impeller. Slip is defined as the deviation between the impeller blade angle and the angle at which fluid leaves the impeller blade. Presumably the reason for the smaller channel wake region is due to the existence of tip leakage flows in the unshrouded impeller. This leakage jet mixes the suction side boundary layer back into the main flow. The lack of this jet in shrouded compressors tends to allow the boundary layer fluid to accumulate on the suction side of the blade causing an increase in the size of the channel wake region. This is contrary to what was suggested in Alder's investigation of a shrouded centrifugal impeller; however, differences in impeller blading designs between the two studies may contribute to the conflicting results.

In 1989, Fagan et al. [17] performed a comparative study between L2F and LDV in a centrifugal compressor. The compressor included a shrouded impeller with a radial exit. The compressor operated at 1800 rpm and a total pressure ratio of 1.03. Both L2F and LDV data were obtained to quantify the flow field throughout the compressor. The investigators found that the L2F system was limited by its inability to make measurements in flows with turbulence intensities greater than 15%. In contrast, L2F is able to obtain measurements significantly closer to stationary surfaces than LDV. On the other hand, LDV was able to acquire measurements closer to rotating surfaces. An additional limitation to L2F was that the sampling rate was an order of magnitude lower than that of LDV since it required more data points to generate the two-dimensional probability density distribution. The authors indicate, though, that the two-dimensional distributions generated by L2F provide more information than the two one-dimensional distributions generated by LDV. The study concluded that by making several modifications to L2F, it could be a useful tool in the realm of turbomachinery research.

In 1993, Hathaway et al. [18] used a two-component LDV probe to acquire measurements of the flow field in a low-speed centrifugal compressor. The low-speed compressor comprised of an impeller with 20 full blades at a backsweep of 55˚ and a vaneless diffuser. The impeller exit diameter was 1.524 m with a blade height of 0.141 m and a constant tip clearance of 2.54 mm. The compressor was operated at 1862 rpm and a mass flow rate of 30 kg/s. The flow was seeded by Polystyrene latex spheres. Three-component velocity measurements were acquired by acquiring measurements in two different laser orientations. The measurements indicated the development of low momentum fluid near the blade surface that migrated outward toward the tip of the blade. Results from CFD confirmed these measurements and indicated that a through-flow momentum wake was formed by fluid that became entrained in the tip leakage jet and convected to the pressure side/shroud corner of the impeller passage. The application of CFD with LDV was able to provide insight into the flow phenomena occurring in areas, where LDV measurements are difficult or impossible, such as the blade tip gap. Likewise, the measurements produced by LDV are able to help validate the computational models used to predict the flow physics in these areas.

A similar study was performed on a high-speed centrifugal compressor in 1997 by Skoch et al. [19]. The impeller contained 15 main blades with 15 splitter blades and had 50˚ of backsweep. The exit impeller diameter was 431 mm, and exit blade height was 17 mm. The compressor was operated at 21,789 rpm and a flow rate of 4.54 kg/s. The impeller had an exit tip speed of 492 m/s and an inlet relative Mach number of 0.9 at the tip and 0.45 at the hub. A single-component LDV probe without frequency shifting was utilized to obtain velocity measurements in the blade passage. The flow was seeded with a liquid dispersion of Aluminum-oxide powder. Skoch was interested in whether the initiation of the through-flow momentum wake observed in Hathaway's larger low-speed compressor could also be found in a smaller high-speed compressor. Results indicated that the flow field was indeed very similar to that documented by Hathaway's larger low-speed compressor. Skoch also formulated that this through-flow momentum wake may begin further upstream than originally suggested for other high-speed compressors. In addition, Skoch did not observe a velocity profile at the impeller discharge that was consistent with Eckardt's jet/wake model.

In 2003, Ibaraki et al. [20] used LDV to conduct detailed flow measurements in a transonic centrifugal compressor impeller. The flow inside of these high-pressure ratio compressors are typically accompanied with a transonic flow region within the inducer of the impeller. The unshrouded transonic impeller contained seven main blades, each with two splitter blades, and the vaned diffuser included 19 vanes. The impeller exit diameter was 373 mm, with an exit blade height of 23.5 mm and 25° of backsweep. The diffuser leading edge diameter was 429 mm. The compressor was operated at a design speed of 24,700 rpm and a pressure ratio of 3.9. The LDV system utilized a two-component probe. The aim of Ibaraki's research was to characterize the interaction between the inducer shock wave and the boundary layer on the blade surface. It was believed that these interactions typically lead to more losses in centrifugal compressors. The investigators, however, were unable to observe any interaction between the shock wave and the boundary layers, but instead they identified an interaction between the shock wave and the tip leakage vortex. This interaction led to an increased total pressure loss in addition to the formation of low-velocity regions near the suction/shroud side of the blades downstream from the shock wave.

In 2008, Schleer et al. [21] obtained three-component LDV measurements inside the vaneless diffuser of a centrifugal compressor. The compressor operated with a design flow rate of 3.5 m^3/s and a pressure ratio of 2.8. The exit impeller diameter was 400 mm with a tip Mach number of 0.6. The investigators were studying the effects of the tip clearance on the diffuser flow field. By shimming the shroud of the compressor, the authors produced both a large tip clearance (2.2 mm, CR = 12.7%) and a small tip clearance (0.7 mm, CR = 4.5%). All measurements were taken with the compressor at a partially loaded condition. Figure 1.12 shows velocity contours of the radial and tangential components in the vaneless diffuser at each tip clearance configuration. Characterizing the large tip clearance configuration, three primary flow regions were identified. Near the suction side of the passage, a tip leakage zone resulting from the leakage through the tip clearance appeared as a blockage. A large channel wake zone was also found and covered most of the blade passage, presumably shifted by the tip clearance zone. This is a deviation from the classical jet-wake model where the channel wake zone represents a much smaller portion of the passage. The third structure identified was a small jet region near the pressure side of the passage. Further downstream, the jet region quickly dissipated leaving behind a stable tip leakage vortex zone and channel wake zone, which remained throughout the diffuser. In addition, the flow near the hub had high radial velocities while the flow near the shroud was locally reversed. For the reduced tip clearance configuration, no flow reversal at the shroud could be identified. Also, the tip clearance zone did not shift the channel wake towards the pressure side of the passage allowing the flow patterns to appear more similar to that predicted by the common jet-wake model.

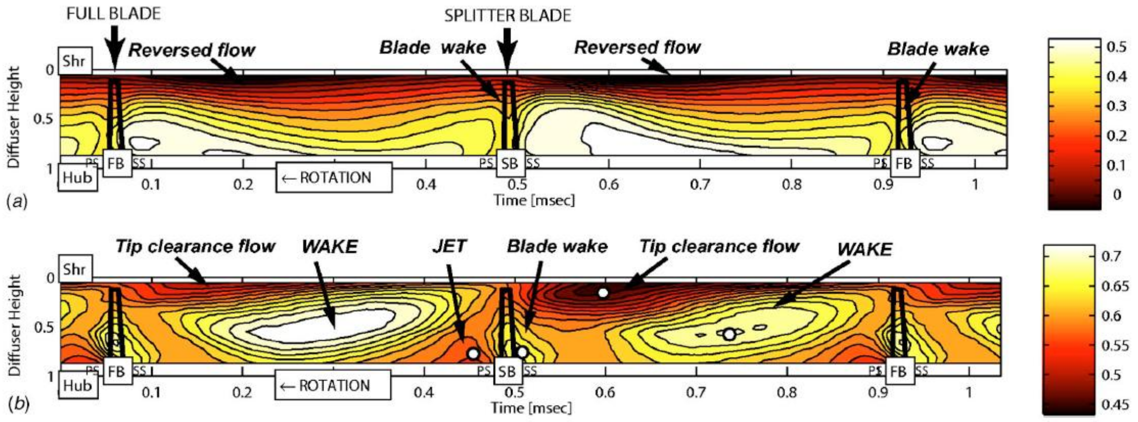

Measured contours of radial and absolute tangential velocities at R/R_2=104% for CR=12.7%

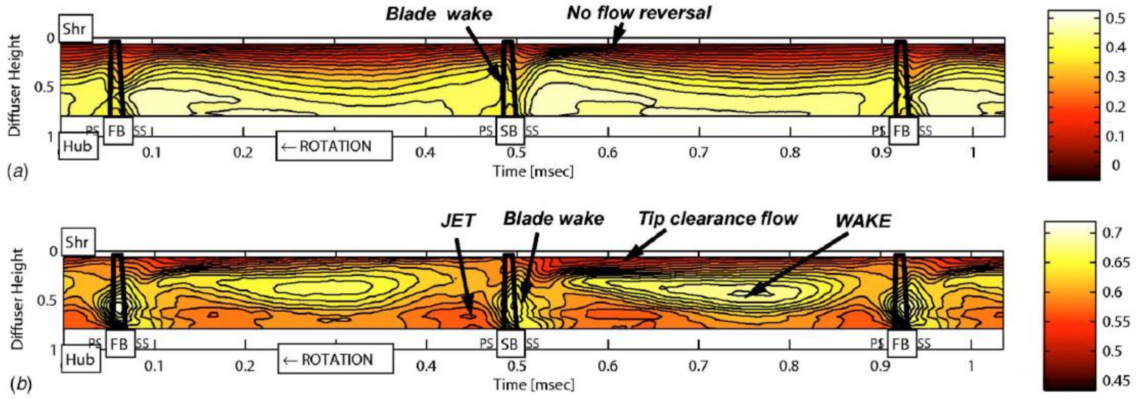

Figure 1.12: Radial and tangential velocity contours by Schleer in the vaneless diffuser of a centrifugal compressor for tip clearance ratios of 4.5% and 12.7%, from [21].

To improve the stable operating range of centrifugal compressors, much research has been conducted near surge. One such study was conducted in 2009 by Bulot et al. [22] on a high-pressure centrifugal compressor near surge. This compressor included a backswept impeller and vaned diffuser. The set up incorporated a four beam LDV system to obtain two-component velocity measurements. The flow was seeded with paraffin oil particles that were injected at the inlet of the facility. Results showed that as the compressor was loaded to stall, changes in the flow structure inside of the impeller were weak and gradual. These changes eventually led to a distorted flow at the impeller exit in terms of flow angle and velocity.

Further study on the inception of surge in centrifugal compressors was conducted by Trebinjac et al. [23] in 2011. The investigators found that near surge, the channel wake from the classical jet-wake model was enlarged. They also found that the time-averaged impeller discharge flow angle was more tangential than at design point. The change in the impeller discharge angle moved the flow trajectory from the diffuser vane suction side to the diffuser vane pressure side resulting in an overloading of the diffuser and an increase in pressure fluctuations at mid-span in the diffuser leading to the onset of surge. These changes in the impeller-diffuser interactions play a significant role in the formation of the flow structures in the impeller. Additional research correlating the inducer flow pattern with this diffuser data is summarized by Buffaz [24].

The role of laser velocimetry as a non-intrusive means to characterize and elucidate the flow phenomena inside centrifugal compressors is vital to the future of turbomachinery development. Without it, most of the present understanding of flow physics would not exist.

1.6 Research Objective

The objective of this research is to modify an existing high-speed, high performance centrifugal compressor research facility to house a Rolls Royce centrifugal research compressor. The facility originally utilized a timed-out Rolls Royce model 250 C28 compressor assembly, which is a production model used in helicopter engines.

Primary modifications to the existing facility include implementation of a new oil system for the compressor and gearbox, replacement of the original throttle and exhaust system, a new inlet plenum for flow conditioning, and instrumentation and sensor upgrades. In addition to the modifications to the existing facility, this thesis documents the capabilities and design of the new Rolls Royce centrifugal compressor and the procedures for its safe operation.

The Rolls Royce centrifugal research compressor is intended to accommodate future impeller and diffuser designs and additional instrumentation. In the future, three-component LDV will be utilized technique to characterize flow phenomena in the impeller and diffuser of the compressor. Therefore, this has necessitated a design for the optical access required to incorporate such an LDV system into future builds. Two potential designs for this future optical access are presented and validated in this thesis.

CHAPTER 2 : RESEARCH FACILITY DESIGN

2.1 Facility Layout

The centrifugal compressor research facility is located in Zucrow Laboratories at Purdue University. The facility includes a 21 by 15 foot test cell with a 10 foot ceiling and control center. The test cell houses an AC motor, a gearbox, an inlet plenum, a research compressor, and peripheral equipment necessary to operate the facility. The AC motor is powered by a variable frequency drive located in the lab. All of the primary components in the test cell are supported on a bedplate to isolate vibrations from the building. The control center is set up outside of the test cell to protect the operator in the event of a malfunction. The control center includes two computers for performance and health monitoring, an AC motor control pedestal, and various data acquisition devices. In addition to the test cell and the control center, two heat exchangers are located outside of the building for oil cooling purposes. Figure 2.1 and Figure 2.2 show the centrifugal compressor research facility and its primary components.

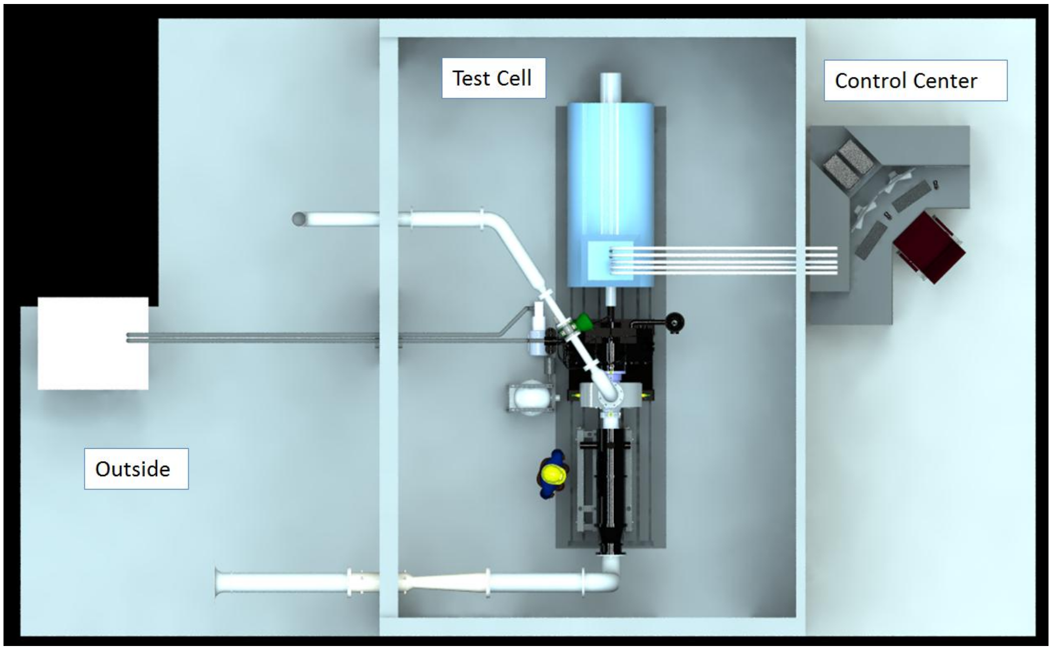

Figure 2.1: Top view of Purdue centrifugal compressor research facility.

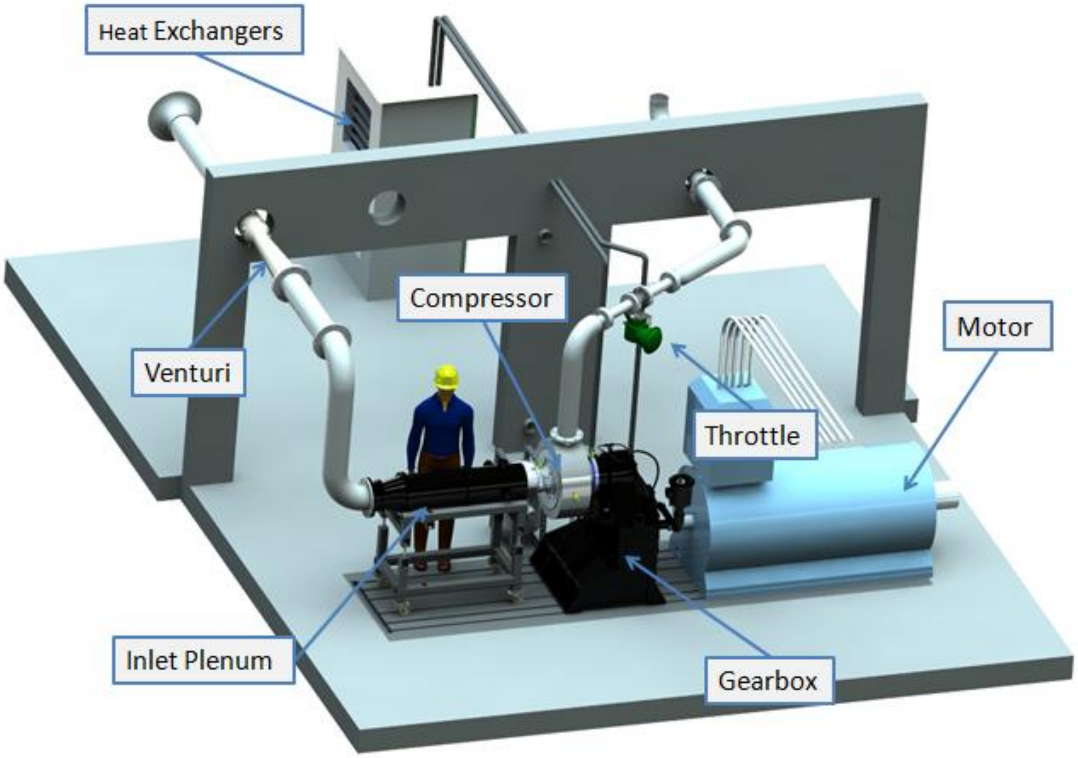

Figure 2.2: Purdue centrifugal compressor test cell layout.

2.2 Research Compressor

The centrifugal research compressor used in this facility is known as CSTAR which stands for Centrifugal Stage Aerodynamic Research. The design is based off of a lower specific speed compressor used in an overall high pressure ratio engine. This type of compressor is sometimes used as the last stage in high overall pressure ratio engines because radial compressors are able to achieve pressure rises through centrifugal effects in conditions that would limit axial stages. An example of one of these limiting conditions would be in rear compressor stages where tip clearances are a larger relative to blade height, often resulting in greater end wall loss for axial stages. Centrifugal compressors are more suitable for low specific flow with high head rise while axial compressors perform better for high specific flow with low head rise. Because the flow in the rear stages of an axial compressor is typically low corrected flow, this is an area where a centrifugal compressor may be more efficient. It is essential to understand the flow in these types of centrifugal compressors to achieve higher overall pressure ratios.

The CSTAR compressor was designed to be employed in a research environment. Unlike aircraft compressors, where size and weight restrictions often result in complex assemblies, CSTAR was designed to be easily operated and disassembled in house. This capability allows Purdue to perform research on current and future designs more efficiently. For example, operators will be able to change different impellers and diffusers on site, avoiding the hassles associated with outsourcing such operations. In addition to its versatile design, the research compressor has instrumentation in areas that are normally inaccessible in aircraft compressors.

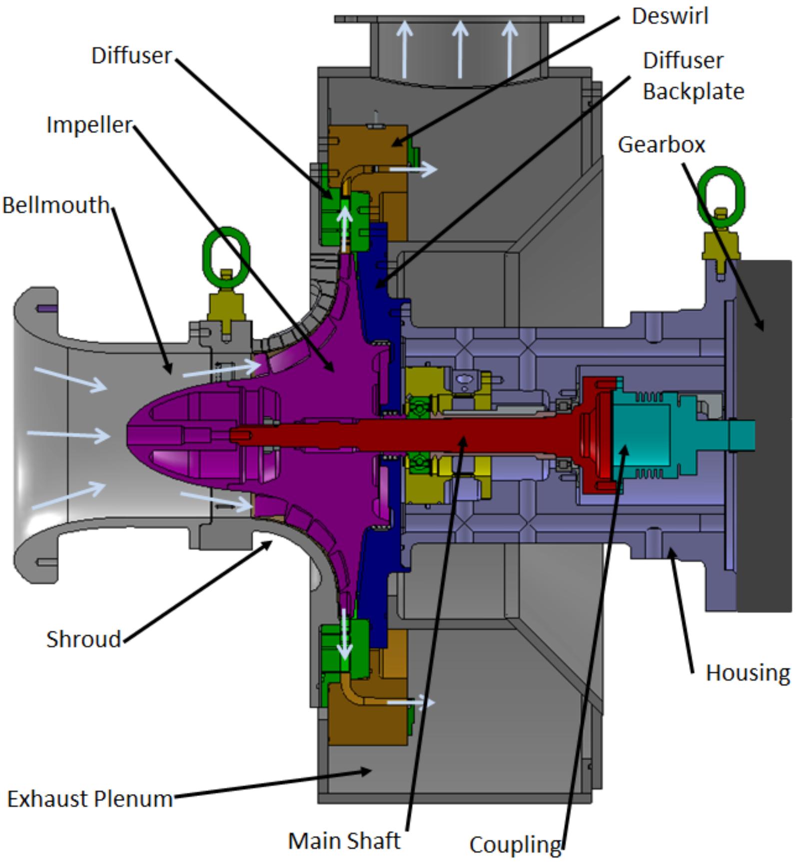

Figure 2.3: Compressor cross-section.

A cross-section view of the CSTAR compressor is shown in Figure 2.3. The research compressor consists of two main systems: the flow path and the drive system. The flow path is made up of the bellmouth, impeller, vane and vaneless diffuser, and deswirl. The bellmouth feeds uniform flow from an inlet plenum chamber to the impeller. It is designed to gradually increase the velocity of the upstream air while avoiding excessive turbulence or pressure drop. The impeller is made up of an equal number of blades and splitters. The impeller uses the rotational speed to raise the energy which then increases the static and total pressure. At the impeller exit, air travels through a vaneless space to the diffuser inlet. The diffuser of the CSTAR compressor contains wedge-shaped vanes that make up a channel diffuser. These vanes are able to further increase the static pressure of the fluid by diffusing the flow. Air leaving the diffuser is turned 90 degrees and directed to the exhaust plenum by the deswirl.

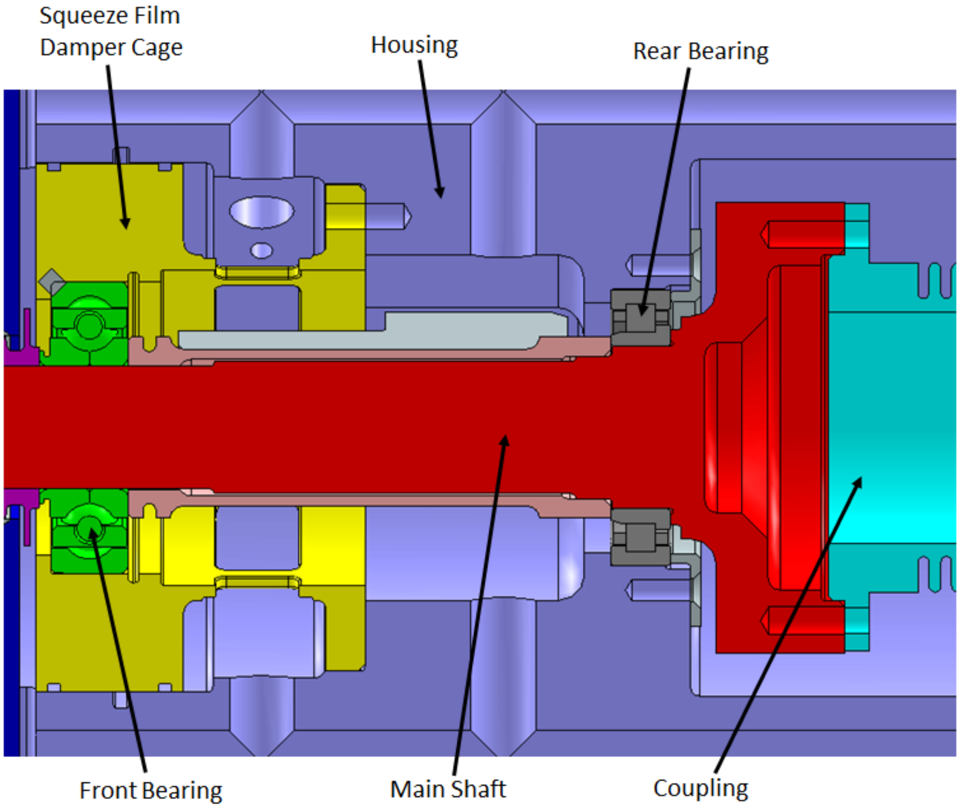

Figure 2.4: Section view of drive system.

Figure 2.4 shows a cross-section view of the Drive System. The function of the drive system is to couple the impeller to a speed-increasing gearbox. The primary components of the drive system include the housing, main shaft, front bearing, rear bearing, and flexible coupling. The housing serves as the main support for the entire research compressor. It holds the compressor cantilevered from the gearbox and encloses the remaining components of the drive system, specifically the main shaft. The purpose of the main shaft is to support and drive the impeller. The alignment and play of the main shaft is determined by the front and rear bearings. The front bearing is a deep groove ball bearing that supports high thrust loads of axial motion. It prevents the impeller from coming in contact with the shroud. The front bearing is held in place by a squeeze film damping squirrel cage. This cage is used to dampen vibrations in the axial and radial directions. It functions by utilizing a thin film of oil between its outer surface and the drive housing that acts as a damper for the components. The rear bearing is a cylindrical roller bearing that allows movement of the shaft in the axial direction, while dampening motion in the radial directions. Supporting the shaft in this way provides enough movement in the axial direction to compensate for contraction of the main shaft at high speeds as well as backlash due to damping in the front bearing. The rear bearing is supported by the drive housing. The flexible coupling is located between the main shaft and the gearbox. It serves two primary purposes. First, it acts as the interface to transmit torque from the gearbox spline to the main shaft. Second, flexible couplings can accommodate some misalignment. This will help protect the compressor from slight misalignments between the main shaft and the gearbox spline.

2.3 Motor and Gearbox

The CSTAR compressor has a design point speed of 22,500 rpm. To run at these speeds, an AC motor and speed increasing gearbox are utilized to drive the entire system. The AC motor is powered by a liquid-cooled variable frequency drive with a maximum voltage output of 480 VAC at 60 Hz. The motor is capable of running up to 1792 rpm at 1400 hp and provides a constant torque of 4101 ft-lbf throughout the entire speed range. The facility is able to control the speed of the motor to within 0.01% of its full range from a pedestal outside of the test cell. The speed increasing gearbox couples the motor to the research compressor. The gearbox has a gear ratio of 30.46:1 allowing the facility to run compressors up to 54,000 rpm. The gearbox also acts as a structural support for the compressor. The compressor is cantilevered to the gearbox by a large 6 bolt flange and pilot surface.

2.4 Primary and Secondary Air Systems

This open system has a steady supply of unconditioned air as the working fluid. This system includes the air intake, the inlet plenum, the compressor flow path, and the compressor discharge.

2.4.1 Air Intake

The main purpose of the air intake is to direct outdoor ambient air to an inlet plenum. The outside air is drawn through a polyester media filter that can prevent foreign particles as small as 7 microns from being ingested into the system. To reduce the pressure drop across the filter, it is attached to a bellmouth that gradually accelerates the flow as it transitions from outside to 8 inch schedule 10 aluminum piping. Downstream of the bellmouth, the relative humidity is measured by a flush mounted hydrometer. At the same location, total temperature, total pressure, and static pressure data are measured and used to calculate static temperature and density. An ASME long-form venturi is located five diameters downstream of this instrumentation and provides mass flow rate measurements of the air intake. It is supported by two ANSI B16.5 Class 150 flanges. Air leaving the venturi then travels through two 90 degree elbows to the inlet plenum where it is straightened before entering the bellmouth of the compressor.

The venturi features an 8.329” inlet diameter and a 4.6926” throat diameter. To ensure an accurate measurement of the mass flow rate, the long form venturi used in the research facility was sent to Colorado Engineering Experiment Station Inc. (CEESI) for calibration. CEESI tested the venturi through a range of throat Reynolds numbers from 1.19e5 to 1.22e6 and inlet pressures from 12.2 to 30 psia to obtain discharge coefficients and expansion factors throughout the range of operation. The calibration was fit with a polynomial curve to determine the discharge coefficient with respect to Reynolds number and the expansion factor with respect to the differential pressure. This calibration will allow accurate measurement of the mass flow rate at design point to within +/- 0.61%. The calibration curve for expansion factor (ε) is:

$$\varepsilon = 1 - 0.93955\frac{dP}{P\gamma}, \tag{2.1}$$

where dP is the differential pressure of the venturi, P is the inlet pressure of the venturi, and γ is the ratio of specific heats. The calibration curve for discharge coefficient (C_d) is:

$$\begin{aligned} C_d = {} & -1.95688E-25Re^4 + 6.10716E-19Re^3 - 6.84047E-13Re^2 \\ & + 3.25299E-7Re + 9.4378E-1, \end{aligned} \tag{2.2}$$

where Re is the Reynolds number at the throat.

2.4.2 Inlet Plenum

The inlet plenum receives air from the air intake and straightens it. It consists of three main sections: an inlet coupling, a wide-angle diffuser, and a plenum chamber, Figure 2.5. The coupling is a removable section that joins the wide-angle diffuser to the 8-inch elbow. Removing this section will provide clearance for the rest of the plenum to detach from the compressor and be taken outside of the test cell during disassembly. The wide-angle diffuser serves to uniformly decelerate the flow before it is received by the 12 inch diameter plenum chamber. Because the transition from 8-inch to 12-inch pipe is so abrupt, there is a risk of end wall boundary layer separation occurring in the wide-angle diffuser. To help avoid separation, a spreader has been incorporated. The spreader is a perforated cone with approximately two thousand 0.25-inch diameter holes and is enclosed by the wide-angle diffuser. The spreader reduces the large-scale turbulence of the upstream air by spreading the single inlet jet from the air intake into thousands of uniformly distributed small jets.

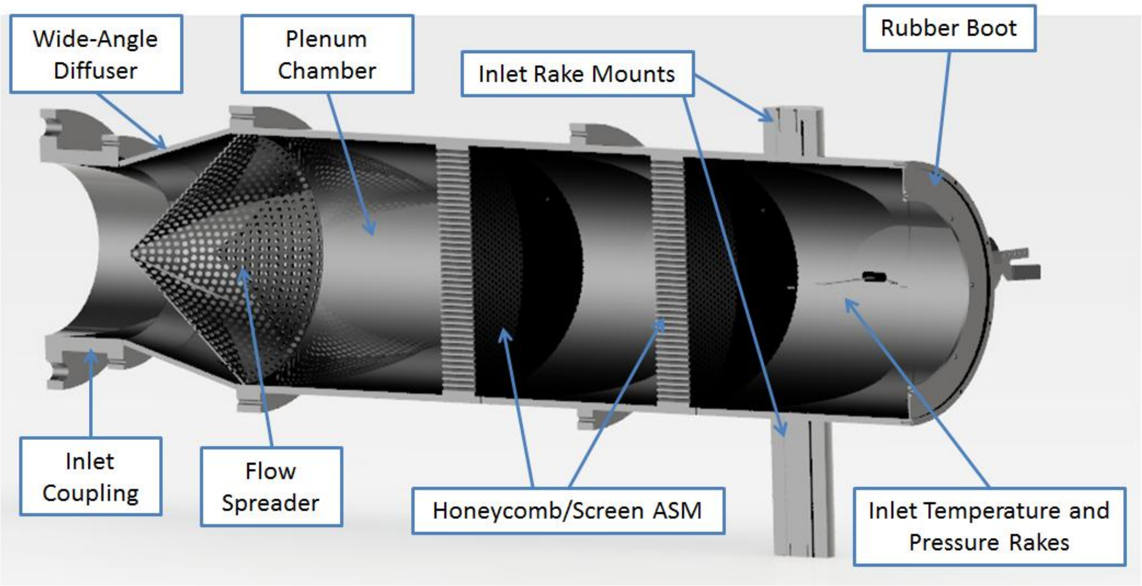

Figure 2.5: Section view of the inlet plenum.

The air leaving the diffuser enters a plenum chamber. The role of the plenum chamber is to settle the flow so that a uniform flow field is delivered to the compressor inlet. The plenum chamber diameter was designed to be as small as possible while still providing an adequate cross sectional area to ensure the entrance Mach number is less than 0.05. This was determined by calculating the static pressure (P), static temperature (T), flow velocity (V), fluid density (ρ) using:

$$P = P_o\left(1 + \frac{\gamma - 1}{2}M^2\right)^{-\frac{\gamma}{\gamma-1}}, \tag{2.3}$$

where P_o is the total pressure and M is the Mach number,

$$T = T_o\left(1 + \frac{\gamma - 1}{2}M^2\right)^{-1}, \tag{2.4}$$

where T_o is the total temperature,

$$V = M\sqrt{\gamma RT}, \tag{2.5}$$

where R is the gas constant, and

$$\rho = \frac{P}{RT}. \tag{2.6}$$

These values were then combined to find the cross-sectional area of the plenum (A_{plenum}) from:

$$A_{plenum} = \frac{\dot{m}}{\rho V}, \tag{2.7}$$

where $\dot{m}$ is the mass flow rate.

To remove non-uniformities from the flow, two sets of honeycomb and screen have been installed in the plenum chamber. The plenum chamber is held together by a custom flange that will allow it to separate into two halves providing better access to these components. The honeycomb is two inches thick, with 0.25-inch cells. Thus, that the length is between 5-10 cell diameters to ensure proper annihilation of lateral components of turbulence, as suggested by [25]. The honeycomb is mounted to the walls of the plenum with three angle brackets. Honeycomb is an effective means to dampen swirl and lateral mean velocity variations, incidentally reducing the turbulence level of the flow. A screen with a 0.0295-inch wire diameter and 0.0787-inch opening size is placed on the downstream side of each honeycomb. From Laws [26], a resistance coefficient (K) of approximately 2.8 will produce a uniform downstream profile regardless of the upstream profile. The resistance coefficient is calculated using the wire diameter (d) and opening size (l) by:

$$K = \frac{0.52(1-\beta^2)}{\beta^2} = 2.88, \tag{2.8}$$

where β is denoted by:

$$\beta = \left(1 - \frac{d}{l}\right)^2. \tag{2.9}$$

The screen imposes a static pressure drop to generate a more uniform velocity field. Total temperature and total pressure rakes are located downstream of the honeycomb to measure the flow uniformity.

A rubber boot is used to connect the plenum chamber to the bellmouth. Using a rubber boot to interface between these two components allows vibrations from the compressor to be isolated. It also reduces the structural loading of the bellmouth, allowing the compressor to remain cantilevered the gearbox. The rubber boot is clamped against the plenum and bellmouth by two inner and outer steel rings. Figure 2.6 depicts the coupling between the bellmouth and inlet plenum.

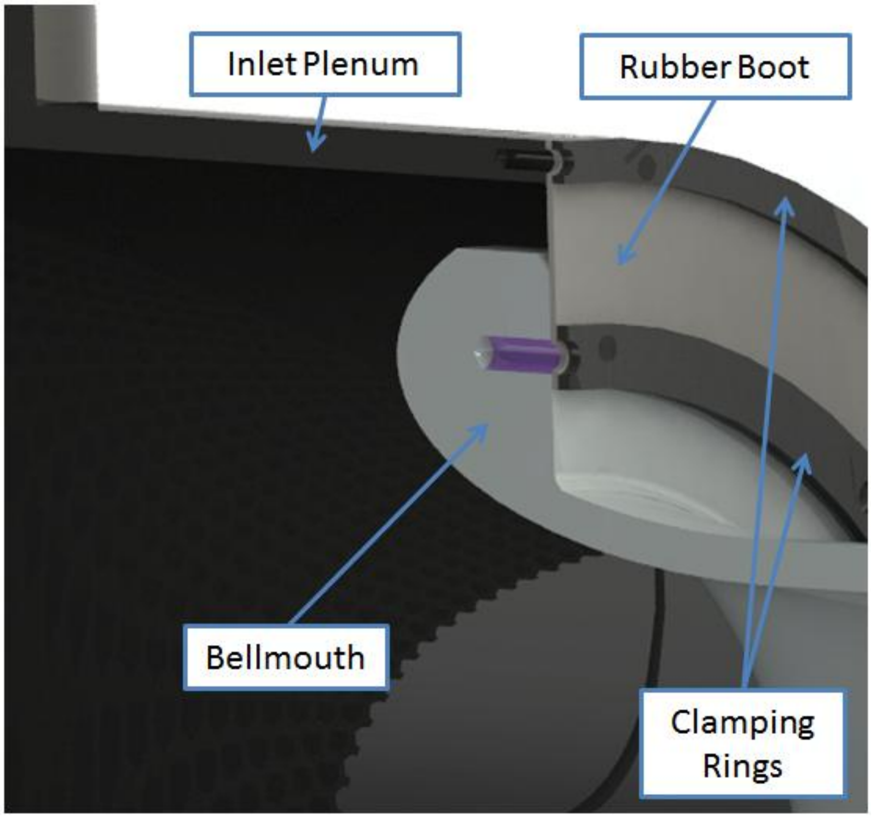

Figure 2.6: Bellmouth and inlet plenum coupling using clamping rings and rubber boot.

2.4.3 Compressor Discharge and Secondary Bleed Systems

The flow path of the compressor and the drive system are separated by a small gap that runs along the back side of the impeller, as shown in Figure 2.7. Some of the air exiting the impeller will escape and travel into this gap. An upper and lower labyrinth seal are used to control the flow of this bleed air. The air that bleeds into this gap consists of the backface and air-oil mist discharge. The air that continues to the diffuser makes up the exit plenum discharge.

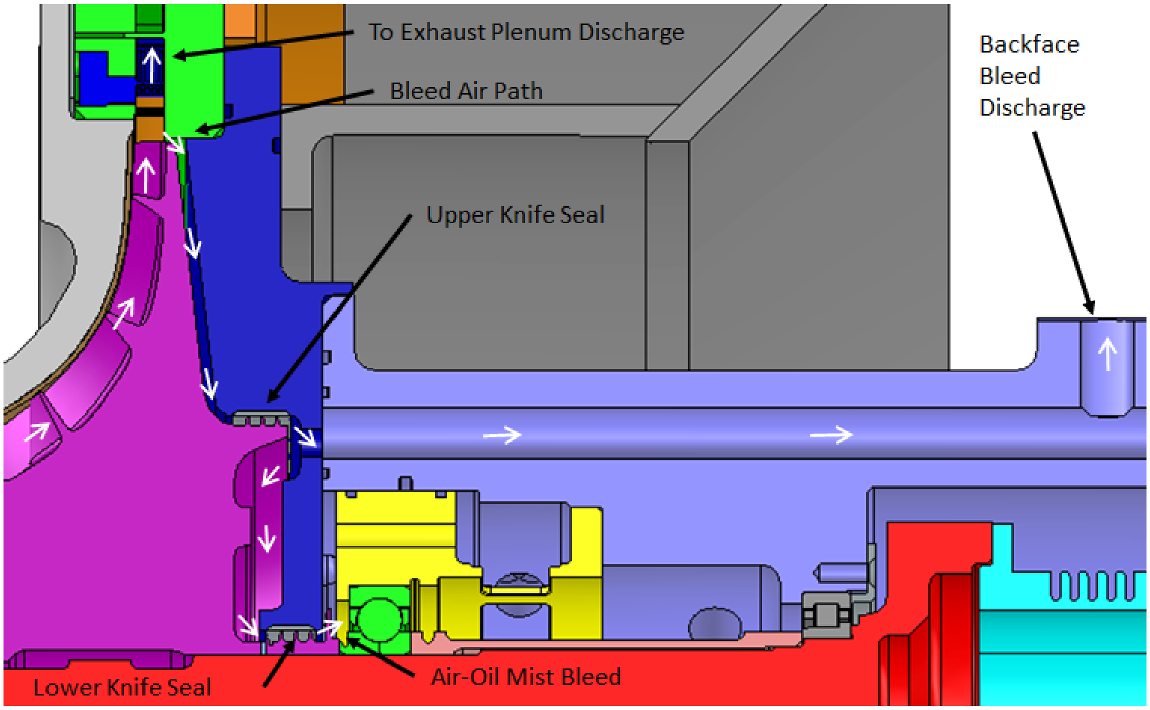

Figure 2.7: Diagram of back face bleed system.

The backface discharge, air-oil mist discharge, and exit plenum discharge all comprise the air leaving the compressor. The backface discharge is made up of air that bleeds past the upper labyrinth seal at the back of the impeller and into the backface bleed outlet. This discharge is routed outside by 1/2 NPT flare tubing where it is released to the atmosphere. The small amount of the bleed air that leaks past the lower labyrinth seal into the drive housing is the air-oil mist discharge and will be discussed in more detail in later sections. The exit plenum discharge consists of the air leaving the deswirl. This represents the majority of the facility's exhaust air. The exhaust discharges to a 6-inch vertical pipe and then through a 90 degree elbow which is reduced to 3-inch pipe to mate up with a throttle valve. Downstream of the throttle valve, the air is diffused back to 6 inch pipe where it is then routed outside. Because the temperature of the air leaving the exhaust may be as high as 400°F, it is released upward to avoid contaminating the air intake.

2.4.4 Throttle

The throttle controls the compressor's mass flow rate by providing a back pressure to the system. As the throttle is closed the flow through the compressor is reduced until the onset of stall or surge. Stall and surge can be characterized by a drop in compressor performance and stability. When stall occurs, the throttle must be opened as quickly as possible to return the compressor to stable operating conditions.

The throttle consists of three components: the valve, the actuator, and the digital valve controller. The valve, a Vee-Ball rotary control valve, is the mechanism that physically restricts the flow. It is driven by a pneumatic rotary actuator that is equipped with a quick release which allows the valve to be opened rapidly in the event of stall or surge. A pneumatic regulator is connected to the facility's 100 psi air supply and provides the rotary actuator with 65 psi of air. In the event that the actuator loses power or air pressure, the valve is spring-loaded to fail open. The actuator is paired with a FIELDVUE DVC2000 digital valve controller for precise control of the valve.

2.5 Oil System

Most of the rotating components of the facility require lubrication to function properly. In the compressor, these components consist of the spline, front bearing, rear bearing, and squeeze film damper. In the gearbox, the components include the gears, roller bearings, and journal bearings. A single system is used to feed the working fluid, Mobil Jet II MIL-23699, to every component. The primary mechanisms in the oil system include a main reservoir, a boost pump, two air-over-oil heat exchangers, a secondary reservoir, and a scavenge pump. A schematic is shown in Figure 2.8. Details such as flow rates and pressures are included in Table 2.1.

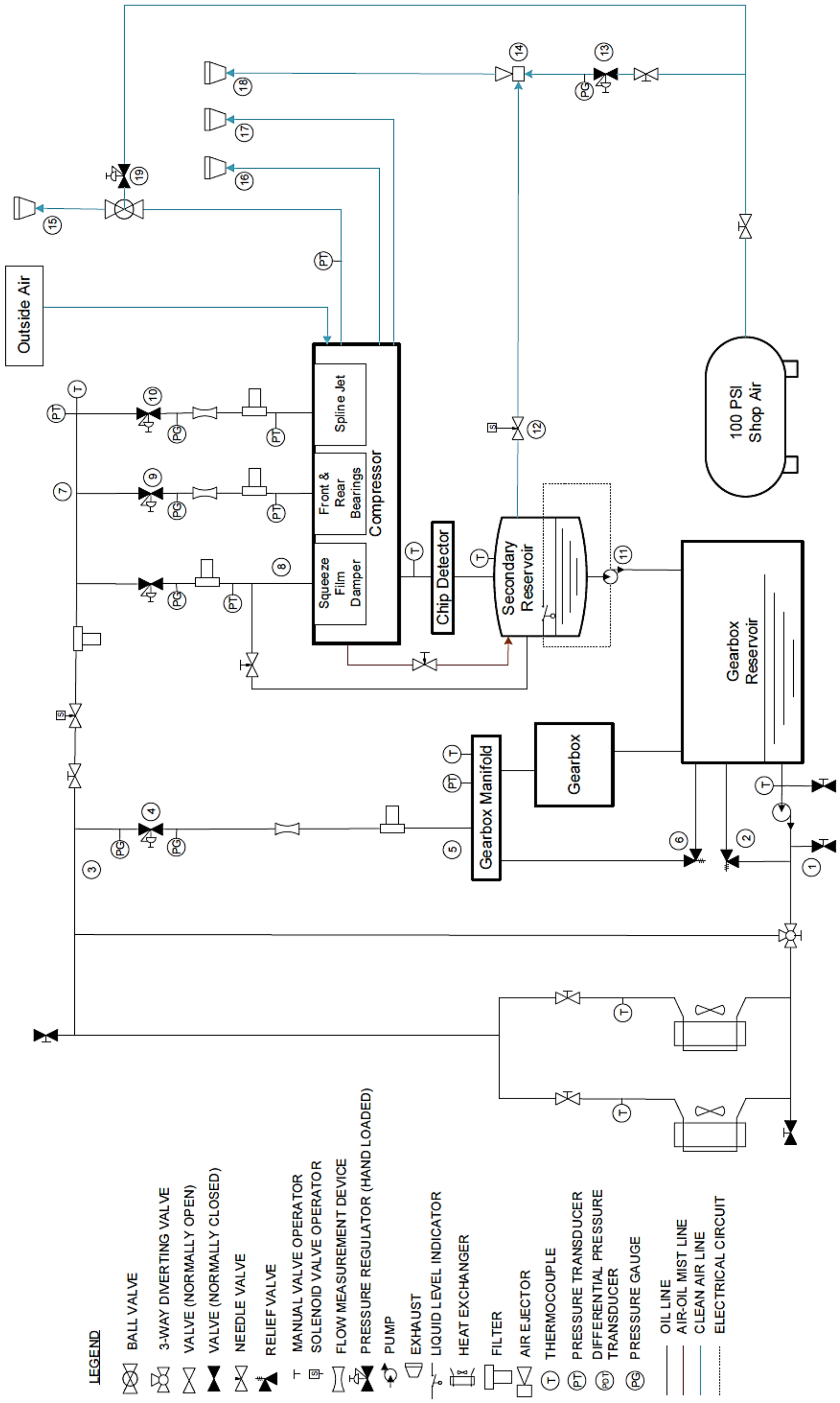

Figure 2.8: Oil plumbing and instrumentation diagram (P&ID) as of 5/30/2014.

Table 2.1: Oil P&ID specification table as of 5/30/2014.

Item Number	Description	Flow Rate (gpm)	Pressure (psig)	Temperature (F)
1	Downstream of Pump	23	160-175	110-150
2	Relief Valve	N/A	150	110-150
3	Downstream of Heat Exchangers	23	150-160	90-135
4	Pressure Regulator	~21.5	120	90-135
5	Gearbox Manifold	~21.5	35	90-135
6	Relief Valve	N/A	35	90-135
7	Compressor Manifold	~1.5	150	90-135
8	SFD Line	0.07	40	90-135
9	Bearing Regulator	0.39	40	90-135
10	Spline Regulator	0.76	75	90-135
11	Scavenge Pump	2.2	0	110-150
12	Throttle Valve	Variable	Variable	70
13	Pressure Regulator	N/A	80	70
14	Air Ejector	4.8 cfm	N/A	70
15	Main Exhaust	N/A	0	N/A
16	Bleed Exhaust 1	N/A	0	N/A
17	Bleed Exhaust 2	N/A	0	N/A
18	Air Mist Exhaust	4.8 cfm	0	N/A
19	Throttle Regulator	N/A	65	N/A

The main reservoir is located at the bottom of the gearbox and contains approximately 50 gallons of oil. The boost pump draws oil from the main reservoir and feeds it to the rest of the system. To prevent the pump from over pressurizing the system and damaging components such as filters, flow meters, and the heat exchangers, a relief valve is used that will return oil back into the main reservoir if the pressure downstream of the pump exceeds 150 psi.

Likewise, to avoid exceeding temperature limitations of the system, a thermostat that measures the temperature of the oil leaving the main reservoir is used to turn on the air-over-oil heat exchangers when the temperature reaches 105°F. To insure that each heat exchanger provides equal cooling, both outlet temperatures are monitored, and the flow of oil is adjusted using manual throttle valves downstream. The heat exchangers are located outside of the facility in a small structure with air louvers to provide protection from the elements. After passing the oil through the heat exchangers, it is then returned to the facility where it can be used for lubrication and cooling. In the event that the ambient temperature outside is cold enough to naturally cool the oil below the recommended bearing operating temperatures specified later, a three-way valve (Assured Automation G33DGXS4MV1-EP010) was installed that will allow the oil to bypass the outside heat exchangers and flow directly to the gearbox and compressors.

The flow of oil to the gearbox components is regulated using a pressure relief valve that holds the oil pressure of the gearbox manifold at 35 psi, feeding excess oil back into the main reservoir. A pressure regulator is located upstream to prevent this relief valve from dropping the pressure of the entire system. This regulator acts as a one-way valve to keep the pressure downstream from propagating upstream. A flow meter is located downstream of this regulator as a safety measure to monitor the flow rate in the line leading to the gearbox manifold. In addition, an inline filter at the manifold protects the gearbox from any foreign particles.

Each of the compressor components requires a different flow of hydraulic oil for proper lubrication and cooling. To independently control the flow to each of these components, the upstream oil enters a 3-way manifold where it is then distributed to three lines: the squeeze film damper, the front and rear bearings, and the spline. The flow rate in each line is then set using pressure regulators. Refer to Table 2.2 for the regulator specifications. The regulators are located as close to the compressor as possible to avoid excessive pressure loss due to pipe friction. They are set so that the pressure of oil entering the compressor is 40 psig for the squeeze film damper and bearing lines and 75 psig for the spline line. Flow meters are located downstream of the regulators to monitor the volumetric flow rate of the bearing and spline lines in the event that any blockage occurs. It is not standard practice to monitor the squeeze film damper line since the flow of oil is so low. In addition to flow meters, in-line filters are used to protect the compressor from upstream particles. Pressure transducers are mounted to the in-line filters to verify the pressure of oil entering the compressor. Because the oil flow rate in the squeeze film damper line is so low, a bypass line with a needle valve was installed to increase the flow of oil in the squeeze film damper line to prevent the pressure regulator from being dead headed. The bypass flow is drained into a secondary oil reservoir. A two-way valve (Assured Automation 2036BA06TA) is installed upstream of the compressor pressure regulators to control when the compressor is provided with oil.

Table 2.2: Compressor pressure regulators

Application	Model	Cv Orifice	Pressure Range (psi)
Squeeze Film Line	Swagelok/CSKPR1EJC422A30010-400	0.06	0-50
Bearing Line	Swagelok/CSKPR1EJC425A30010-400	0.20	0-50
Spline Jet Line	Swagelok/CSKPR1EJC427A30010-400	0.50	0-100

Oil entering the drive housing is accelerated through small orifices into high pressure jets used to lubricate and cool the compressor components. The sizes of these orifices were chosen to generate the proper flow rate for the given upstream pressure. The oil then collects at the bottom of the drive housing where it drains into a 19 gallon secondary reservoir through a ½-inch NPT line. To ensure proper drainage of the oil, a second line, the air-oil mist line, connects the top of the drive housing to the secondary reservoir. This line contains a needle valve to drop the pressure of the secondary reservoir relative to the drive housing. Doing this creates a vacuum that will pull the oil into the reservoir.

It is imperative that the oil in the drive housing is prevented from leaking into the compressor flow path. This is accomplished by an oil flinger and the two labyrinth seals mentioned earlier. A depiction of the oil flinger and lower labyrinth seal is shown in Figure 2.9. The oil flinger rotates with the main shaft and blocks oil by flinging the oil radially outward and away from the seals. This oil then collects at the bottom of the drive housing where it is drained by gravity. In addition to the oil flinger, the air-oil mist discharge mentioned earlier that leaks across the lower seal will aid in preventing oil from leaking up the back plate and into the flow path. To ensure that this discharge is always flowing into the drive housing, the pressure of the drive housing is actively controlled so that it is lower than the pressure of the air upstream of the lower labyrinth seal. This is accomplished by monitoring the static pressure on both sides of the seal and manually adjusting the back pressure of the air-oil mist line with an electronically actuated throttle valve to generate the appropriate pressure drop during operation. This pressure drop is maintained at approximately 2 psig. At lower speeds, the pressure upstream of the lower seal may be sub-atmospheric and incapable of driving air into the drive housing. To compensate for these pressure deficiencies, an air ejector (McMaster-Carr 9997K18) that is regulated to 80 psi from the facilities 100 psi air supply has been added to the system to generate a vacuum.

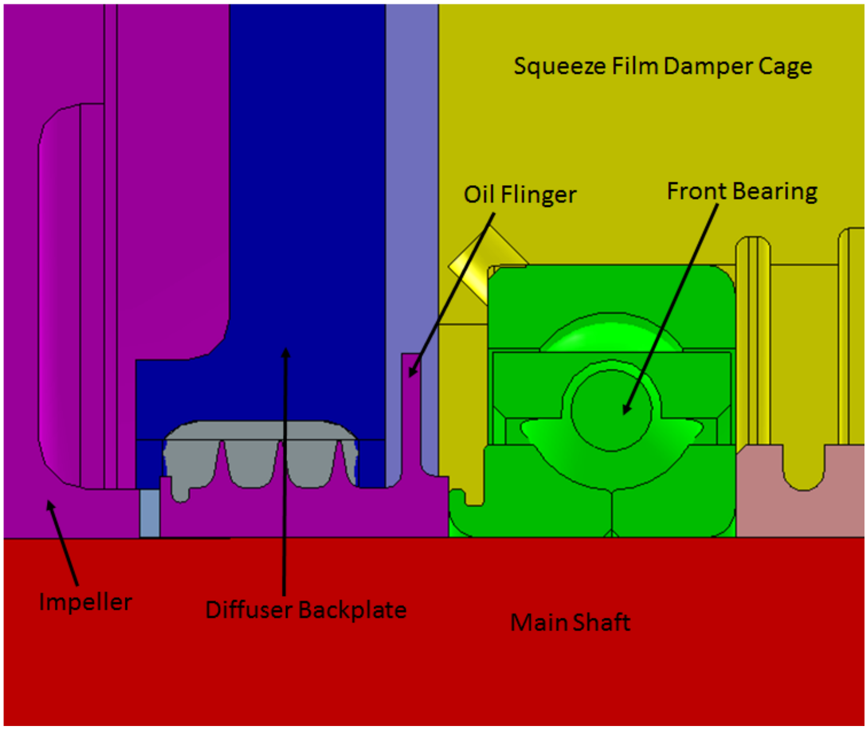

Figure 2.9: Depiction of lower labyrinth seal and oil flinger.

A scavenge gear pump (McMaster-Carr 4272K31) is used to drain oil from the secondary reservoir and feed it back into the main reservoir. Because the flow rate of the scavenge pump is greater than that of the oil entering the secondary reservoir, a relay is used to turn the pump on and off and ensure that the pump always has a sufficient supply of oil to drain to prevent cavitation. The relay is controlled using an ultra-sonic level indicator that monitors the level of oil in the tank, turning the pump on when the tank is full. The indoor oil system, oil pumps, and heat exchangers are shown in Figure 2.10, Figure 2.11, and Figure 2.12, respectively.

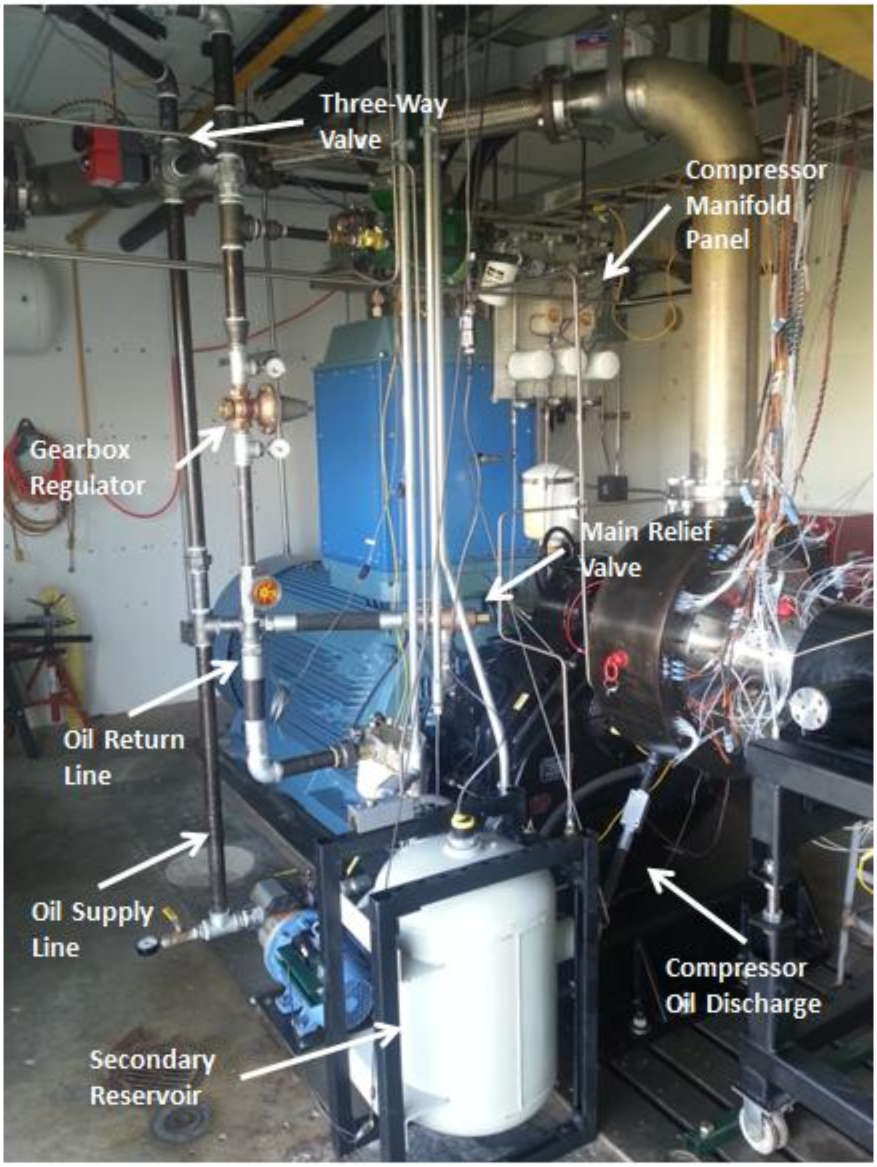

Figure 2.10: Test cell oil system layout.

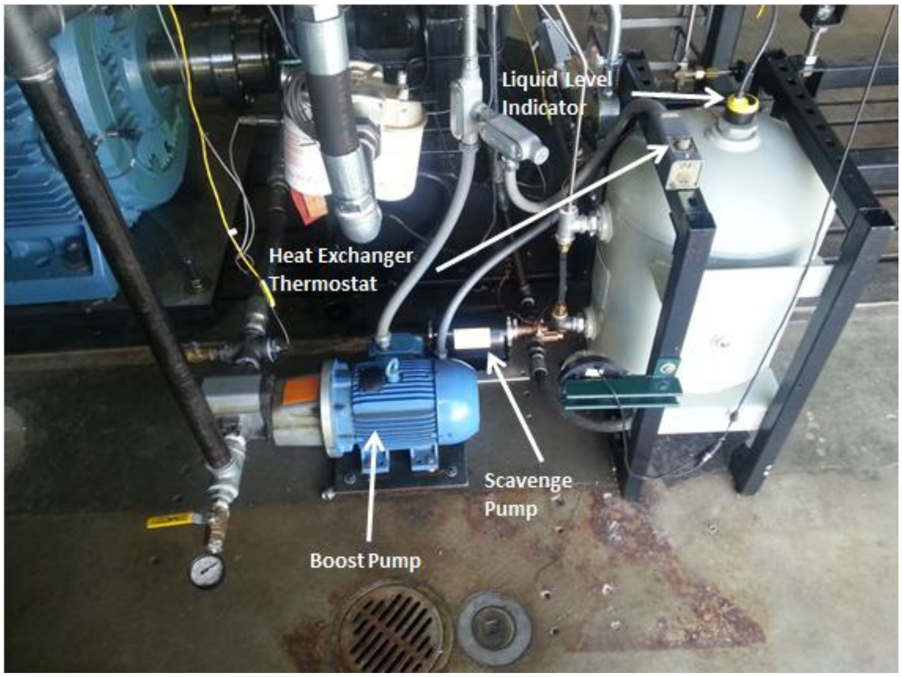

Figure 2.11: Test cell oil pumps.

Figure 2.12: Outdoor heat exchanger layout.

CHAPTER 3 : INSTRUMENTATION AND CONTROL

Instrumentation and control of the facility is crucial to ensure accuracy of the data gathered and safety for the compressor system. The instrumentation discussed in this section will either serve to monitor the health of the system or to collect measurements of the compressor's performance. In addition, tools for controlling the compressor system will be mentioned as well as the procedures for the safe operation of the facility.

3.1 Health Monitoring Instrumentation

The health monitoring system is made up of data acquisition hardware that feeds information from instrumentation to a PC where it is recorded and displayed using LabVIEW. This information includes measurements that indicate the health and functionality of critical components in the oil system and the gearbox.

3.1.1 Health Monitoring Data Acquisition

Health monitoring is performed on a single PC with LabVIEW to display real-time data and record data. Measurements are acquired and sent to the PC by a National Instrument (NI) PCI 6250 card, an NI USB 6351 device, and an Agilient 34980A mainframe. Refer to Figure 3.1 for an illustration of the health monitoring data acquisition system.

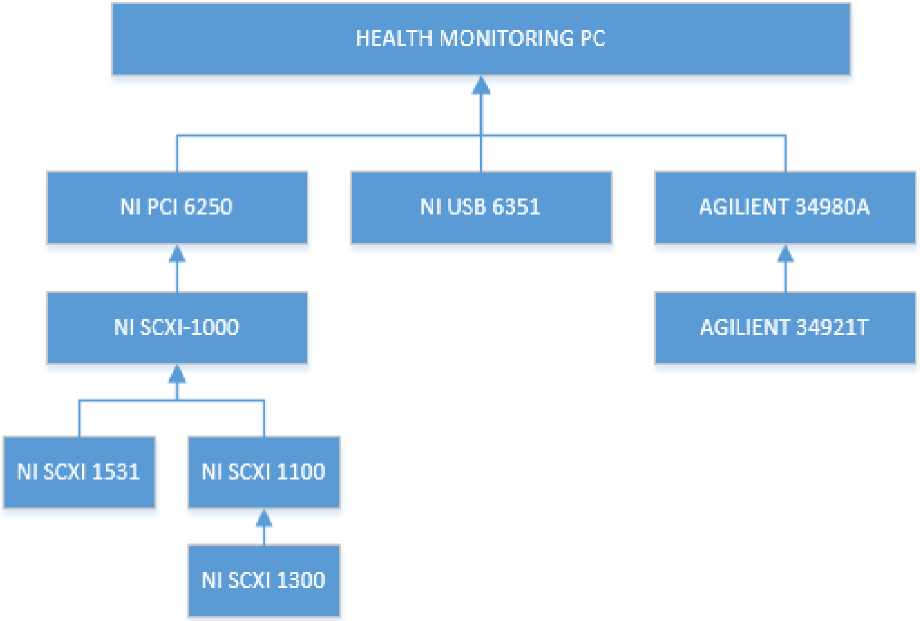

Figure 3.1: Health monitoring data acquisition system.

The NI PCI 6250 collects data from an NI SCXI-1000 chassis that can house up to four different data acquisition modules. An NI SCXI 1531 and NI SCXI 1100 module fill two of these slots currently. The NI SCXI 1531, Table 3.1, is used to read, filter, and condition up to eight integrated electronic piezoelectric compatible accelerometers. This module is used to monitor gearbox vibrations. The NI SCXI 1100 uses a NI SCXI 1300 terminal block to communicate up to 32 inputs such as voltage, current, and thermocouples to the NI PCI 6250. The NI SCXI 1300, Table 3.2, also includes a cold-junction reference for type T and type K thermal couples. The NI SCXI 1100 acquires various signals including motor speed, oil pressures, and metal chip detection.

The NI USB 6351 device, Table 3.3, communicates with the computer through its USB port. This device is capable of acquiring up to eight high-speed digital and analog voltage inputs and can provide up to two high speed +/- 10V output signals. This is used to monitor compressor vibration and oil system flow rates in addition to controlling a three way valve and oil throttle.

The Agilent 34980A is a multifunction switch/measurement system that is capable of various input and output operations through up to eight attached modules. It communicates with the PC through an Ethernet switch. An Agilent 34921T module that is attached to the Agilent 34980A is capable of reading up to 40 different inputs. This module primarily serves to acquire temperature measurements. Table 3.4 provides a list of measurements acquired by the Agilent 34921T.

Table 3.1: National instrument SCXI 1531 module.

National Instrument SCXI 1531 Module			
Channel	**Sensor Type**	**Reading**	**Measurement**
0	Accelerometer	Gearbox Vertical	Acceleration
1	Accelerometer	Gearbox Axial	Acceleration
2	Accelerometer	Gearbox Lateral	Acceleration

Table 3.2: National instrument SCXI 1300 terminal block

National Instrument SCXI 1300 Terminal Block			
Channel	**Sensor Type**	**Reading**	**Measurement**
0	Voltage/Thermo	Comp Bearing Flow	Flow rate
1	Voltage/Thermo	Spline Flow	Flow rate
2	Voltage/Thermo	Gearbox Flow	Flow rate
4	Voltage/Thermo	Comp Front Brg P1	Pressure (psia)
5	Voltage/Thermo	Comp Front Brg P2	Pressure (psia)
6	Voltage/Thermo	Comp Rear Brg P1	Pressure (psia)
7	Voltage/Thermo	Comp Rear Brg P2	Pressure (psia)
8	Voltage/Thermo	ETI Throttle Fdbk	Voltage
9	Voltage/Thermo	Level Sensor Fdbk	Voltage
12	Voltage/Thermo	GB Manifold OP	Pressure
13	Voltage/Thermo	Spline OP	Pressure
14	Voltage/Thermo	Comp Manifold OP	Pressure
15	Voltage/Thermo	Squeeze Film OP	Pressure
16	Voltage/Thermo	Comp Bearing OP	Pressure
17	Voltage/Thermo	Chip Detector	Voltage

Table 3.3: National instrument USB 6351

National Instrument USB 6351			
Channel	**Sensor Type**	**Reading**	**Measurement**
0	Voltage	Comp Fwd Vertical Accel	Acceleration
1	Voltage	Comp Fwd Lateral Accel	Acceleration
2	Voltage	Comp Rear Vertical Accel	Acceleration
3	Voltage	Comp Rear Lateral Accel	Acceleration
4	Voltage	RPM	Acceleration
8	Voltage	Comp Fwd Verical Accel	Acceleration
9	Voltage	Comp Fwd Lateral Accel	Acceleration
10	Voltage	Comp Rear Vertical Accel	Acceleration
11	Voltage	Comp Rear Lateral Accel	Acceleration
12	Voltage	RPM	Acceleration
14	Voltage		Acceleration
0	Output Voltage ±10	3 Way valve Cntrl	
1	Output Voltage ±10	ETI Throttle Ctrl	

Table 3.4: Health monitoring Agilent 34921T measurement unit.

Health Monitoring Agilent 34921T Measurement Unit			
Channel	**Sensor Type**	**Reading**	**Measurement**
1001	T-type TC	GB Bearing Forward 1	Temperature
1002	T-type TC	GB Bearing Forward 2	Temperature
1003	T-type TC	GB Bearing Rear 1	Temperature
1004	T-type TC	GB Bearing Rear 2	Temperature
1005	T-type TC	Comp Bearing Forward 1	Temperature
1006	T-type TC	Comp Bearing Forward 1	Temperature
1007	T-type TC	Comp Bearing Rear 1	Temperature
1008	T-type TC	Comp Bearing Rear 2	Temperature
1011	K-type TC	GB Reservoir	Temperature
1012	K-type TC	GB Manifold	Temperature
1013	K-type TC	Comp Manifold	Temperature
1014	K-type TC	Comp Exit Oil	Temperature
1015	K-type TC	Secondary Reservoir Top	Temperature
1016	K-type TC	HEX 1	Temperature
1017	K-type TC	HEX 2	Temperature
1040	Voltage	Thermistor CJC	Temperature

3.1.2 Oil System Instrumentation

The oil system instrumentation includes thermocouples, pressure transducers, flow meters, switches, a liquid level indicator, and a metal chip detector. Figure 2.8 and Table 2.1 provide a detailed layout of the oil system instrumentation. Critical instrumentation for the oil system is specified in Table 3.5.

Table 3.5: Oil system instrumentation specifications

Oil System Instrumentation Specifications							
Manufacturer	**Model #**	**Sensor Type**	**Range**	**Accuracy FSA**	**Resolution**	**Output**	**Max Temp.**
Omega	FPR207-PS	Turbine Meter	5-50 gpm	+/-2%	1 gpm	0-50 Hz	225°F
Omega	FPR301	Turbine Meter	0.07-5 gpm	+/-1%	0.05 gpm	1200-1380 pulses/gallon	160°F
Omega	LVCN414	Level Transmitter	1.25 m	+/-0.25%	3 mm	4-20 mA	140°F
Allen Aircraft Products, INC	3407151	Chip Detector	N/A	N/A	N/A	Voltage Signal	300°F

3.1.2.1 Temperature Measurements

The overall temperature of the system is controlled by two air-over-oil heat exchangers. A type K thermocouple is located upstream of the boost pump to validate the temperature at which the thermostat triggers the heat exchangers. The temperature of the oil leaving each heat exchanger is also monitored by type K thermocouples to ensure that the oil is being cooled equally. Throttle valves located downstream of the heat exchangers can be adjusted in the event that the oil is not being cooled equally. A three way valve was also installed to bypass the outdoor heat exchangers when the oil is too cool. The valve position is controlled using a 0 – 10 VDC output signal from the USB 6351, and it's powered by a 13.8 VDC power supply.

An additional type K thermocouple measures the oil of the temperature at the gearbox manifold. To prevent the gearbox bearings from overheating, a temperature switch located at the gearbox manifold automatically shuts down the motor if the temperature of the oil entering the gearbox exceeds 135°F. Inside the gearbox, four type T thermocouples are used to monitor the temperature of the high-speed journal bearings. The bearing outer race temperatures should not exceed 210°F.

The temperature of the oil in the compressor manifold, the front and rear bearings, and the oil leaving the compressor are all monitored using type K thermocouples. To ensure proper lubrication in the drive housing, four thermocouples are used to obtain the metal temperature of the front and rear bearings. The temperature of these bearings during operation should be maintained at approximately 250°F. The temperature limit on the bearings is 300°F.

In addition to the temperature measurements previously discussed, the metal temperature of the secondary reservoir near an ultrasonic liquid level indicator is monitored by an adhesive type K thermocouple to ensure that the reservoir temperature does not exceed the 140°F working limit of the sensor. Each thermocouple listed in this section is connected to the Agilent 34921T module.

3.1.2.2 Pressure Measurements

Oil pressure is monitored at the gearbox manifold, the compressor manifold, and the inlets to the drive housing. The pressures at these locations control the amount of lubrication to critical components.

At the gearbox manifold, the pressure is set to 35 psig using a relief valve. It is monitored by a 100 psig pressure transducer that is connected to the system's NI SCXI 1300 module. A pressure switch connected to the gearbox manifold automatically shuts down the motor in the event that the pressure drops below 18 psig.

Omega PX319-200G5V pressure transducers are used to monitor oil pressure at the compressor manifold and drive housing inlets. These 200 psig transducers have a full scale accuracy of 0.25% and a linear output of 0-5V. The compressor manifold transducer is connected to the NI SCXI 1300 module, while the drive housing inlet transducers are connected to the health monitoring Agilent 34912T module. The pressure at the compressor manifold should be approximately 150 psig after upstream pressure loss. Warnings in LabVIEW will alert the operator if the pressure of the manifold falls below 120 psig. The three lines supplying oil to the drive housing are made up of the squeeze film damper line, compressor bearing line, and spline line. The oil pressure of each of these lines is monitored in close proximity to the drive housing. Both damper and bearing lines should be 40 psig, and the spline line should be 75 psig, per the compressor designer's specifications. These pressures are set by regulators downstream from the compressor manifold.

3.1.2.3 Flow Rate Measurements

Flow meters are used to monitor the flow rates in the lines supplying oil to the gearbox, the compressor bearings, and the compressor spline jet. An Omega FPR207-PS turbine flow meter is used for the gearbox line. This meter has a measurement range of 5-50 gpm and an accuracy of +/- 1 gpm. The flow of oil in the gearbox line is approximately 23 gpm and warnings in the LabVIEW code occur when it falls below 30 gpm. The compressor bearing and spline lines are both monitored by Omega FPR301 turbine flow meters. These meters have a measurement range of 0.07-5 gpm and an accuracy of +/- 0.05 gpm. The flow of oil in the bearing and spline lines should be 0.39 gpm and 0.76 gpm, respectively. Both flow meters transmit a linear blind pulse voltage signal to the system’s NI USB 6351.

3.1.2.4 Chip detector and Liquid Level Indicator

A metal chip detector is used to monitor the oil leaving the compressor for any metal fragments. The principle behind the metal chip detector is that two magnets in the device will accumulate any small metal chips that may be present in the oil. The accumulation of these chips will complete a circuit that sends a signal to the NI SCXI 1300 alerting the operator. The detection of fragments may indicate a problem with one of the compressor bearings or splines.

An Omega LVCN414 ultrasonic level sensor measures the level of oil in the secondary reservoir. This sensor is connected to a relay (McMaster-Carr 47475K62) that triggers the scavenge pump when the height of oil in the reservoir is 5 inches. Once the pump has drained the oil in the reservoir to a level near empty the level sensor will shut off the pump. The ultrasonic level sensor continuously transmits the level of oil in the reservoir through the CB-68 LP to LabVIEW where it is displayed on the front panel. Figure 3.2 illustrates the circuit used to control the scavenge pump with the LVCN414. In the event that the level indicator fails to trigger the scavenge pump, a bypass switch is installed that will override the pump relay and manually operates the pump.

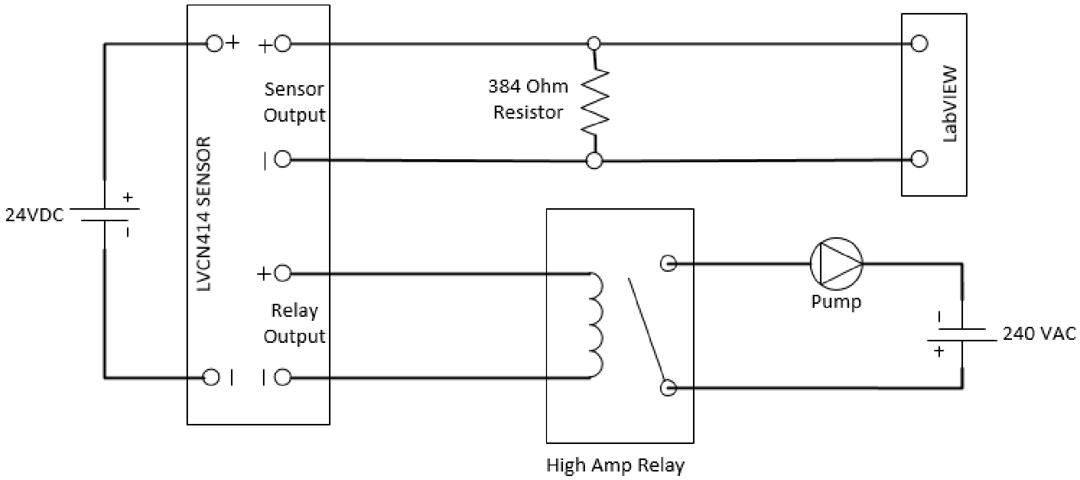

Figure 3.2: Level sensor circuit diagram.

3.1.3 Vibration Monitoring

Critical components such as the gearbox and compressor require vibration monitoring to ensure that they are operating within the proper working parameters. These vibration readings are acquired with accelerometers, each capable of measuring vibrations along a single axis. Three accelerometers are used to monitor the gearbox, and four are used to monitor the compressor.

The gearbox uses integrated electronic piezoelectric accelerometers. Two monitor vibrations in the vertical and lateral directions from the high speed journal bearings inside. An additional one is used to monitor axial vibrations along the gearbox's intermediate shaft. Each of these accelerometers interface with the NI SCXI 1531 module for signal filtering and amplification. Warnings in LabVIEW will alert the operator if any of the gearbox vibration measurements exceed 0.3 inches per second (IPS).

The accelerometers on the compressor are of charge-output piezoelectric type. Two of these are used to monitor the vertical and lateral vibrations of the front ball bearing. Two additional measure the vertical and lateral vibrations of the rear roller bearing. These accelerometers require different signal conditioning from the integrated electronic piezoelectric type used for the gearbox. The compressor accelerometers interface with Endevco 6634B signal conditioners that provide 0-10V outputs for the acceleration, velocity, and displacement of each measurement. The signal conditioners transmit this information to LabVIEW through the USB 6351 where it is recorded and monitored. The maximum allowable velocity of the vibrations measurements is 0.22 ips. Table 3.6 includes a list of the accelerometers, signal conditioners, and limiting conditions. Table 3.7 specifies the safety features implemented by the facility.

Table 3.6: Vibration instrumentation.

Vibration Instrumentation			
Accelerometer	**Model #**	**Signal Conditioner**	**Max IPS**
Compressor Front Lateral	CEC 4-130-0005	NI USB 6351	0.22
Compressor Front Vertical	CEC 4-130-0005	NI USB 6351	0.22
Compressor Rear Lateral	Endevco 6222S-100A	Endevco 6634B	0.22
Compressor Rear Vertical	CEC 4-130-0005	NI USB 6351	0.22
Gearbox Vertical	ICP 603 C01	NI SCXI-1531	0.3
Gearbox Lateral	ICP 603 C01	NI SCXI-1531	0.3
Gearbox Axial	ICP 603 C01	NI SCXI-1531	0.3

Table 3.7: Facility safety features.

Facility Safety Features			
Feature	**Location**	**Limiting Parameter**	**Action**
Pressure Switch	Gearbox Manifold	18 psig falling	E-Stop Automatically Triggered
Temperature Switch	Gearbox Manifold	135 F rising	E-Stop Automatically Triggered
Chip Detector	Oil Path Downstream of Compressor	Metal Chips Detected	Warning in Health Monitoring Code-Manual Shut Down
Accelerometers	Gearbox & Drive Housing	0.3 or 0.22 ips, as detailed in Table 3.6	Warning in Health Monitoring Code-Manual Shut Down
Compressor Bearing Temperature	Rear Bearing Outer Racing	300˚F	Warning in Health Monitoring Code-Manual Shut Down
Compressor Bearing Temperature	Front Bearing Outer Racing	300˚F	Warning in Health Monitoring Code-Manual Shut Down
Pressure Sensor	Compressor Manifold	120 psig	Warning in Health Monitoring Code-Manual Shut Down
Pressure Sensor to Monitor Surge	Compressor Exhaust	Large Amplitude Oscillations	Open Throttle manually by hitting Throttle Emergency-Open button
Flow Meter	Oil Path Upstream of Gearbox	15 gpm falling	Warning in Health Monitoring Code-Manual Shut Down
Flow Meter	Oil Path Upstream of Compressor Spline	0.4 gpm falling	Warning in Health Monitoring Code-Manual Shut Down
Flow Meter	Oil Path Upstream of Compressor Bearings	0.2 gpm falling	Warning in Health Monitoring Code-Manual Shut Down
Level Sensor	Secondary Reservoir	10 in. rising	Warning in Health Monitoring Code-Manual Shut Down
Oil Temperature	Compressor Manifold	160˚F	Warning in Health Monitoring Code-Manual Shut Down

3.2 Compressor Performance Instrumentation

Compressor performance instrumentation allows the facility to control and experimentally determine the performance of the CSTAR compressor and is crucial to the research performed in this facility. The system used to acquire compressor performance includes a data acquisition system, compressor instrumentation, and a PC. The data acquisition system is used to communicate information between the performance instrumentation and LabVIEW on the PC. This section will discuss the different performance instrumentation used to acquire measurements in this facility, as well as the data acquisition hardware used to feed these measurements to a PC where the information can be recorded, processed, and displayed by LabVIEW.

3.2.1 Performance Data Acquisition

The performance data acquisition system consists of a PCI 6035E card, an Agilent 34980A mainframe, and several Scanivalve digital sensor array (DSA) modules. These measurements are collected by a single Performance PC where they can be processed and displayed on a LabVIEW front panel. Figure 3.3 illustrates this data acquisition system.

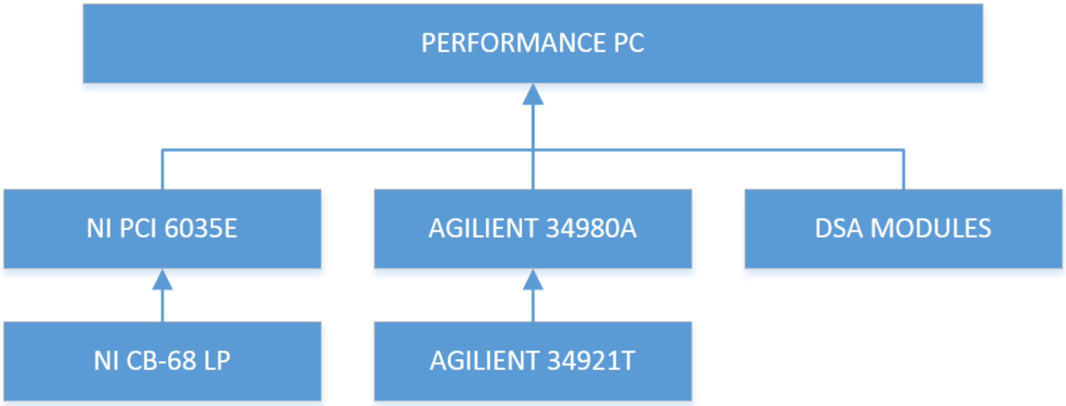

Figure 3.3: Performance data acquisition system.

The PCI 6035E card transmits signals from a NI CB-68LP device to the PC. The NI CB-68LP, Table 3.8, is a unshielded 68-pin input-output board that is capable of reading 15 analog and 15 digital voltage inputs as well as providing two +/- 10V outputs. This device is used to read various pressure and voltage measurement from the system in addition to controlling both the air-oil mist and compressor throttles.

The Agilent 34980A mainframe is identical to the unit used for health monitoring. It also has an identical Agilent 34921T module that is capable of up to 40 inputs. This main frame is used to acquire readings from the various thermocouples in the test cell. An Ethernet switch communicates these readings to the performance computer.

Table 3.8: National Instrument CB-68 LP Terminal Block.

National Instrument CB-68 LP Terminal Block			
Channel	**Sensor Type**	**Reading**	**Measurement**
0	Voltage	P ATM Mensor	Pressure
1	Voltage	Inlet Pitot Ps (Rosemount)	Pressure
2	Voltage	Inlet Pitot Po (Rosemount)	Pressure
3	Voltage	Venturi Mensor	Voltage
4	Voltage	Venturi Rosemount	Voltage
5	Voltage	Humidity sensor	Voltage
6	Voltage	Exhaust Surge	Voltage
7	Voltage	E-Open Button	Voltage
8	Voltage	Throttle Feedback	Voltage
9	Voltage	RPM	Voltage
0	Output Voltage ±10	Throttle Ouput V	

3.2.2 Mass Flow Rate Measurements

The facility utilizes four components to accurately determine the mass flow rate of the compressor. These components include a settling chamber, a humidity sensor, a pitot total-static probe, and a long-form ASME venturi.

Figure 3.4: Settling chamber for atmospheric pressure measurements.

Figure 3.5: Omega HX94AV hydrometer.

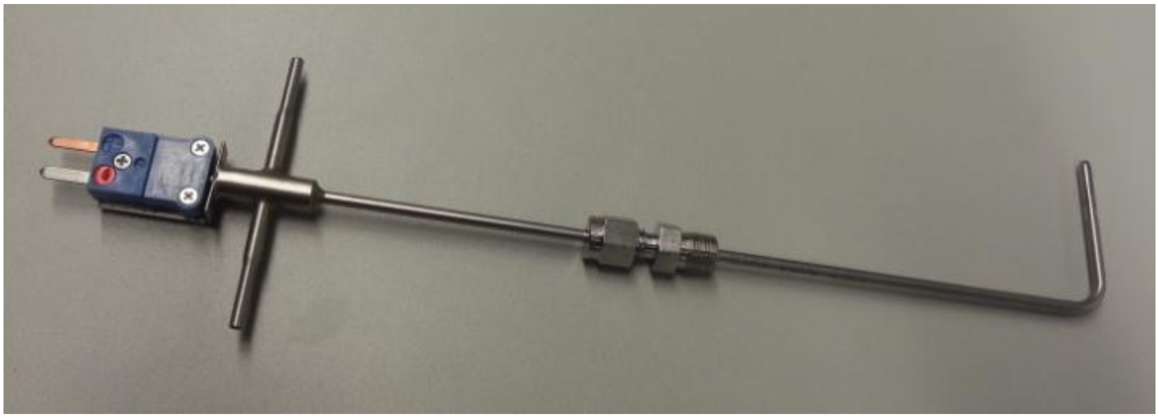

Figure 3.6: United Sensor PAC-T-8-K-KL-Mini plug pitot probe.

The settling chamber is a PVC capsule with a flow conditioner that is used to dampen air from outside affects, Figure 3.4. This enables the facility to obtain extremely accurate measurements of the ambient air pressure. This is important because the ambient air pressure is used in almost every calculation in the performance code. A Mensor CPT6110 barometric pressure transducer has a range of 13-15 psi and a full-scale accuracy of 0.01% and acquires the ambient pressure measurement. The plenum is located at the control center. An Omega HX94AV, Figure 3.5, is used to collect the humidity of the flow five diameters upstream of the inlet of the venturi. It is accurate to within +/-2.5% relative humidity. The sensor outputs a 0-1V signal to the CB-68 LP. The relative humidity is used to determine the molar composition of the air. At the same location, a United Sensor PAC-T-8-K-KL-Mini plug pitot-static probe gathers the total temperature, total pressure, and static pressure of the fluid in the center of the pipe, Figure 3.6. This information is used to calculate the density of the fluid. The total pressure and static measurements are acquired by two 0-5 inchH_2O Rosemount 3051S Series pressure transducers. The Rosemount 3051S Series pressure transducers provide a 0-5V output and have a +/- 0.04% full-scale accuracy. The temperature measurement, a type T thermocouple, is taken by the performance Agilent 34921T module. The ASME Long Form Venturi downstream of the pitot probe is a device that measures the flow rate of a fluid. It functions by gradually increasing the velocity of the flow resulting in a measureable static pressure drop. A Mensor CPT6110 differential pressure transducer measures the lower range of this pressure drop while a Rosemount 3051S series pressure transducer measures the upper range. The Mensor transducer has a 0.03% full-scale accuracy of its 0-0.36 psig range, and the Rosemount transducer has +/- 0.06% full-scale accuracy of its 0-50 inH_2O range. Both interface with the CB-68 LP. Obtaining the pressure drop with transducers at different ranges results in a more accurate overall measurement.

3.2.3 Compressor Inlet Flow Measurements

Compressor inlet instrumentation includes all instrumentation from the inlet plenum to the inducer. Quantities measured include static pressure, total pressure, and total temperature.

The first set of rakes is located one throat diameter upstream of the bellmouth inlet in the inlet plenum chamber. Originally used in an earlier plenum, these rakes have been retrofitted to mate with the current plenum. The two rakes are shown in Figure 3.7 and Figure 3.8. One rake includes three elements and the other rake contains four elements, each element capable of reading total pressure and total temperature. Because the current plenum is smaller in diameter than the earlier design, only five of the seven elements are used. Two different sets of measurement locations are possible depending on the mounts chosen for each rake. These two configurations are depicted in Figure 3.9 and Figure 3.10. A total of four mounts are available on the plenum allowing the facility to clock the rakes at 90 degrees intervals. The pressure measurements are acquired by DSA3016 pressure scanners and the temperature measurements are acquired by the Agilent 34980A. Table 3.9 shows the specifications for each of the pressure measurement devices used in this facility.

Figure 3.7: Three element inlet plenum total temperature and total pressure rake.

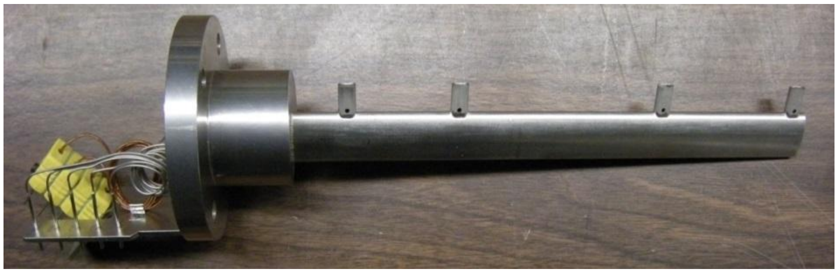

Figure 3.8: Four element inlet plenum total temperature and total pressure rake, from [27].

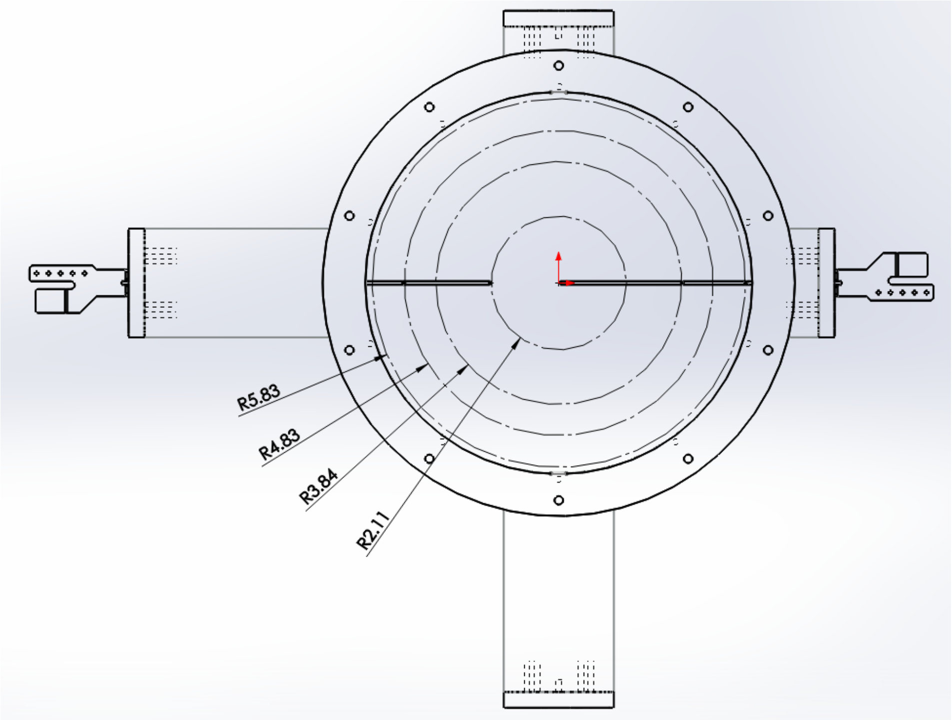

Figure 3.9: Inlet plenum rake clocking configuration 1.

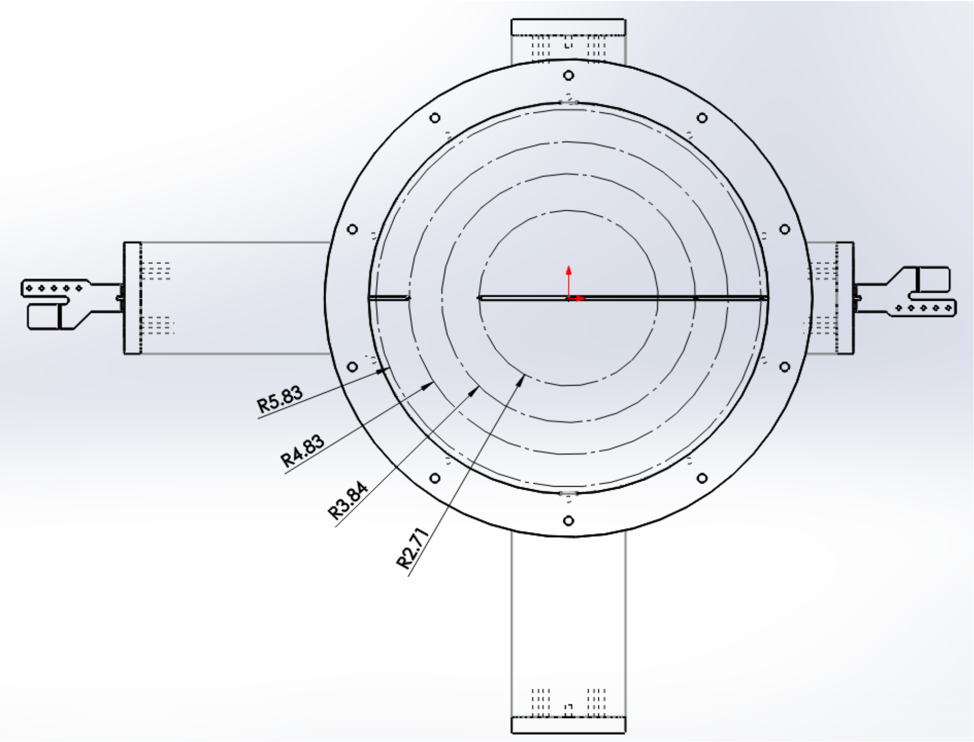

Figure 3.10: Inlet plenum rake clocking configuration 2.

Table 3.9: Pressure measurement device specifications.

Pressure Measurement Device Specifications						
Manufacturer	**Model #**	**Type**	**Range**	**Accuracy FS**	**Uncertainty**	**Output**
Scanivalve	DSA3217	Differential	0-5 psi	+/-0.05%	0.0025 psi	Ethernet
Scanivalve	DSA3217	Differential	0-30 psi	+/-0.05%	0.015 psi	Ethernet
Scanivalve	DSA3016	Differential	0-15 psi	+/-0.05%	0.0075 psi	Ethernet
Scanivalve	DSA3016	Differential	0-30 psi	+/-0.05%	0.015 psi	Ethernet
Mensor	CPT6110	Differential	0-0.36 psi	+/-0.03%	0.000108 psi	0-5V
Mensor	CPT6110	Barometric	13-15 psi	+/-0.01%	0.0002 psi	0-5V
Omega	PX319-200G5V	Differential	0-200 psi	+/-0.25%	0.5 psi	0-5V
Rosemount	3051S	Differential	0-5 inWc	+/-0.04%	0.002 inWc	0-5V
Rosemount	3051S	Differential	0-50 inWc	+/-0.06%	0.03 inWc	0-5V

The last set of inlet measurements are located 1.4 inches upstream of the impeller inlet. They include two total temperature rakes, two total pressure rakes, and two static pressure taps. The total temperature rakes consist of five elements and are located at 150 and 330 degrees forward looking aft (FLA). Figure 3.11 illustrates one of the four inlet compressor rakes. The total pressure rakes each contain five total pressure elements. The static pressure taps are located in the shroud at the same plane as the inlet rakes. Both the pressure rakes and taps are mounted at 30 and 210 degrees. These pressure measurements are obtained using DSA3016 pressure scanners and the temperature measurements are acquired using the Agilent 34980A.

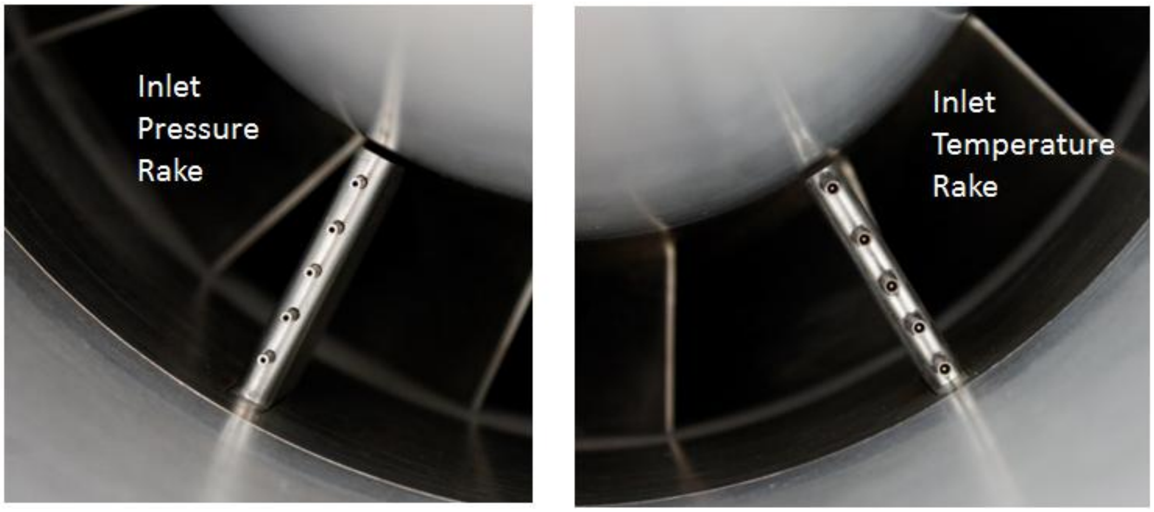

Figure 3.11: Two of four inlet compressor rakes.

In addition to the rakes, a mount at 60 degrees FLA is available for a probe traverse mechanism. This device can be equipped with various instrumentation and used to perform radial traverses. Examples of this instrumentation would include boundary layer probes, total temperature probes, and hot wire probes.

3.2.4 Impeller and Diffuser Measurements

All of the measurements acquired from the impeller inlet to the diffuser exit comprise of static pressure taps, total pressure rakes, total temperature rakes, and tip clearance measurement probes.

A total of 23 static pressure taps line the shroud. Of these 23 static taps, 19 are located at top dead center (TDC) and four are placed at 120 and 240 degree positions near the impeller inlet. Seven of the 19 TDC static pressure taps are located at the impeller exit. These measurements are made with using the DSA3016 pressure scanners. Figure 3.12 illustrates a portion of these impeller static taps.

Figure 3.12: Impeller static pressure taps.

A FM high-temperature clearance measurement system is used to acquire the blade tip clearance during operation of the compressor. These measurements are obtained at six different locations along the shroud. Figure 3.13 shows two of the six capacitance probes installed in the compressor. Three are equally distributed around the knee of the impeller and three are equally distributed at the impeller exit. The system is capable of withstanding temperatures up to 1400°C and is accurate to within 0.0004 inches. These high precisions are important because the anticipated clearance when running at design speed is 0.007" at the inducer and 0.003" at the exducer. The tip clearance measurement system is standalone and does not interface with either the performance or health monitoring PCs. This system consists of probes, oscillators, a demodulator, and central processing module (CPM). The tip clearance system works on the principle that measuring the capacitance between a passing blade and the probe electrode can be used to determine the distance between them. The probes are connected to oscillators that form a fixed frequency. As a blade passes by, the change in capacitance is seen as a modulation of that frequency. This frequency modulation is then demodulated and changed to an output voltage by the demodulator. The CPMs process this output voltage and convert it into a tip clearance based on stored calibration data.

Figure 3.13: Knee and exducer capacitance probes used to measure blade tip clearance.

The calibration data includes calibrations for specific channel, probe, oscillator, and cap configurations and can be found in Table 3.10. The capacitance probes feature caps that match the contour of the flow path. Each probe is calibrated using the cap that was formed for that probe's particular location. Calibrating each probe, channel, oscillator, and cap as one unit decreases the uncertainty in the probe measurements. Measured RMS values of the cold geometry tip clearance by the capacitance probes is shown in Table 3.11.

Table 3.10: Calibration configurations for CSTAR.

Channel Number	**Probe Serial**	**Oscillator Serial**	**Cap Number**	**Cal Disc Number**	**Purdue Reference&Filename**
1	B223/G13/0061	713/794	1	ADT0269	CC-pos1
2	B223/G13/0062	713/795	2	ADT0269	CC-pos2
3	B223/G13/0063	713/796	3	ADT0269	CC-pos3
4	B223/G13/0064	713/797	4	ADT0270	CC-pos4
5	B223/G13/0065	713/798	5	ADT0270	CC-pos5
6	B223/G13/0066	713/799	6	ADT0270	CC-pos6

Table 3.11: Cold geometry tip clearances as measured by the capacitance probes.

Capacitance Probe	Location	Cold Clearance (mils)
1	Exducer	11
2	Exducer	20
3	Exducer	18
4	Knee	14
5	Knee	7
6	Knee	11

In the diffuser, static pressure taps, instrumented vanes, and total pressure rakes have been installed to collect measurements. A total of 12 static pressure taps are also installed along the shroud side of two vane passages. These passages are located at 90 and 270 degrees forward looking aft (FLA). The taps are equally distributed among the two passages to measure the static pressure at both the inlet and exit of the diffuser. Figure 3.14 shows the static pressure taps within one of these diffuser passages. Two removable diffuser passages are installed at 135 and 315 degrees FLA and are equipped with total pressure and temperature probes, Figure 3.15. Each of these passages consists of two vanes with leading edge instrumentation. One vane in each removable passage is embedded with four total pressure elements and the other with three total temperature elements. Finally, at the diffuser exit, eight total pressure rakes have been installed, Figure 3.16. Each of these rakes contains four total pressure elements. The pressure measurements are acquired by DSA3016 pressure scanners and the temperature measurements are acquired by the Agilent 4980A.

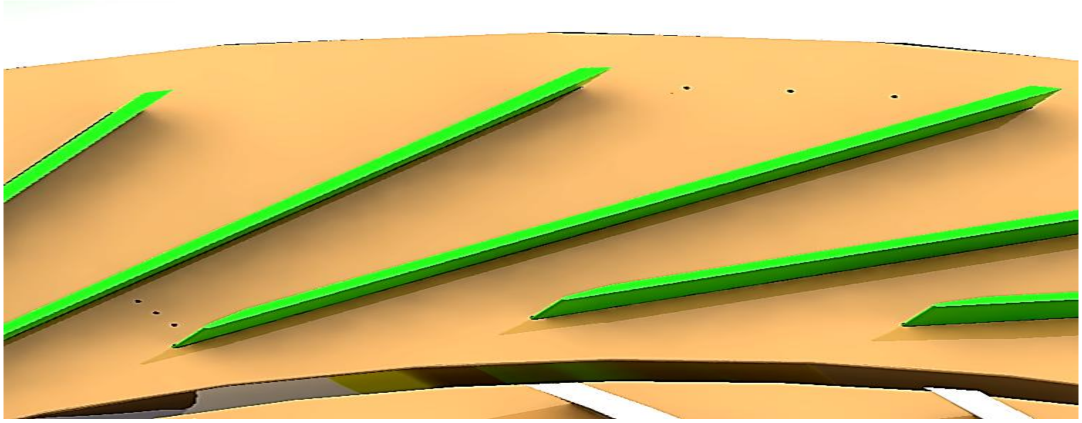

Figure 3.14: Diffuser passage static pressure taps.

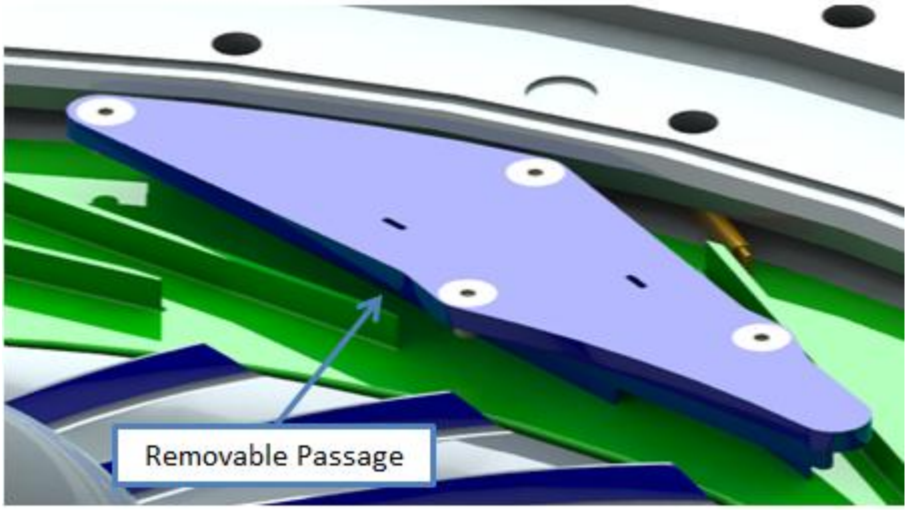

Figure 3.15: Removable instrumented diffuser passage.

Figure 3.16: Two of the eight diffuser exit total pressure rakes.

3.2.5 Discharge Measurements

Discharge measurements include all instrumentation downstream of the diffuser. This instrumentation includes deswirl static pressure taps, deswirl inlet total pressure rakes, deswirl exit total temperature rakes, and a pressure transducer to detect the onset of surge.

At the inlet of the deswirl, a total of five rakes measure the total pressure. Each of these rakes consists of four elements, Figure 3.17. Within the deswirl passage, six static pressure taps line the inner and outer walls. Three of the taps are installed along the outer wall and the remaining three are installed along inner wall, Figure 3.18. These taps are located at the 340 degree position looking aft. Four total temperature rakes are installed at the deswirl exit. Each of these rakes comprises of three elements, Figure 3.19. Finally, in the piping outside of the exit plenum, an Omega PX319-200G5V is used to monitor the flow for pressure fluctuations that would indicate the onset of surge. This measurement interfaces with the CB-68 LP. The specifications for all the compressor rakes is shown in Table 3.12.

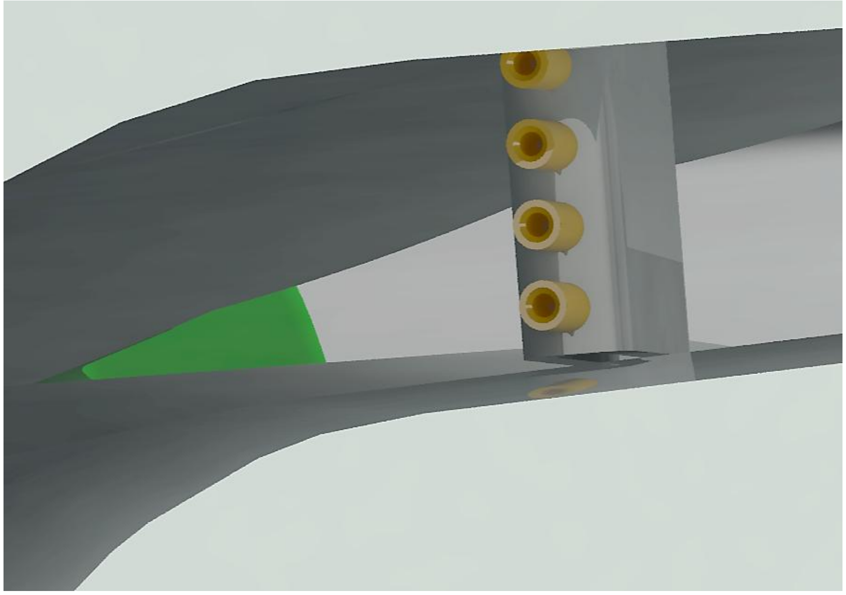

Figure 3.17: One of five deswirl inlet total pressure rakes.

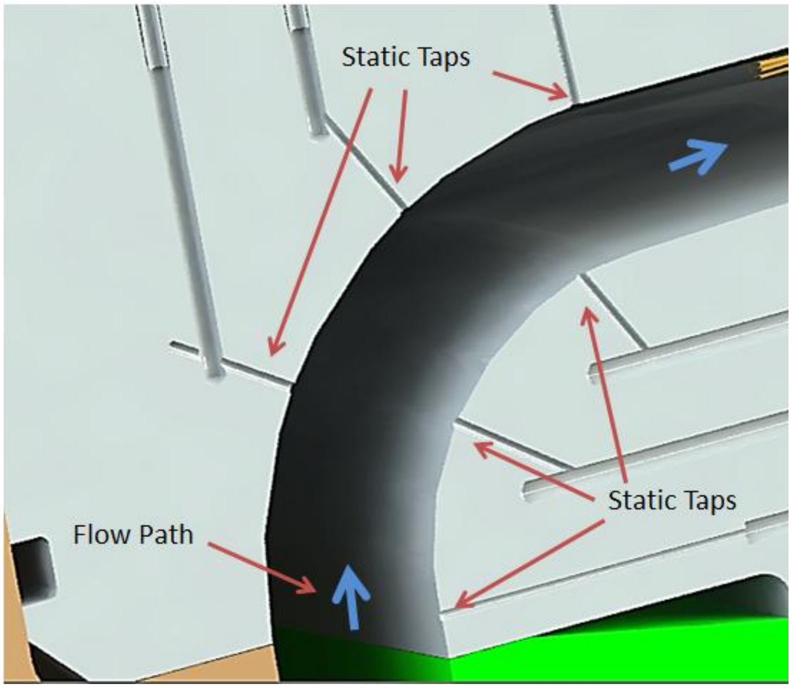

Figure 3.18: Six deswirl static pressure taps.

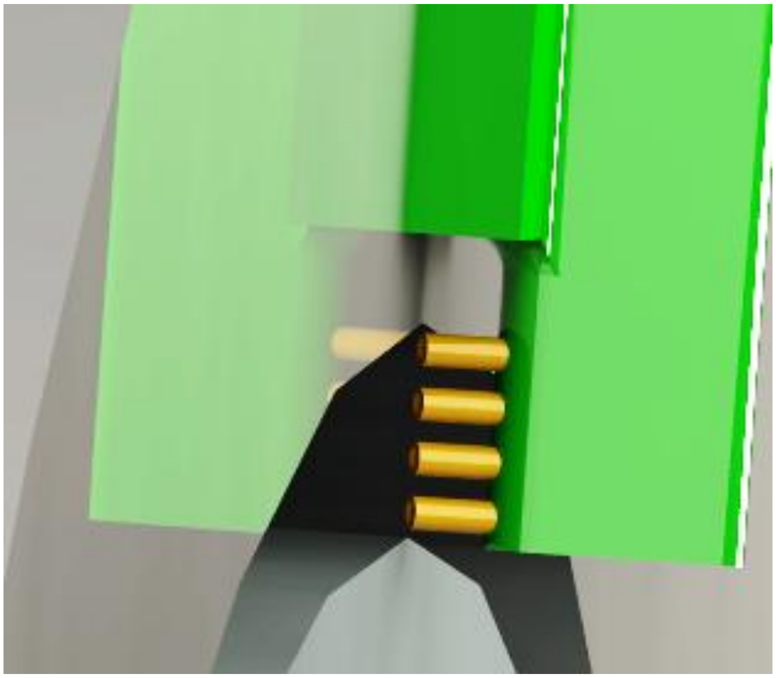

Figure 3.19: One of four total temperature rakes located at the deswirl exit.

Table 3.12: Compressor rake geometry specifications.

Rake	Measurement	Element	Span	Kiel Diameter (in)	Kiel Angle
Inlet Rake #1	Po	1	0.839	0.042 x 0.013 Wall	45˚
		2	0.672		
		3	0.504		
		4	0.336		
		5	0.168		
Inlet Rake #2	To	1	0.927	0.042 x 0.010 Wall	45˚
		2	0.746		
		3	0.554		
		4	0.353		
		5	0.121		
Diffuser Inlet #1	Po	1	0.879	0.032 x 0.005 Wall	45˚
		2	0.631		
		3	0.380		
		4	0.133		
Diffuser Inlet #2	To	1	0.752	0.032 x 0.005 Wall	45˚
		2	0.452		
		3	0.153		
Diffuser Exit	Po	1	0.876	0.032 x 0.005 Wall	45˚
		2	0.628		
		3	0.378		
		4	0.130		
Deswirl Inlet	Po	1	0.967	0.032 x 0.005 Wall	45˚
		2	0.711		
		3	0.456		
		4	0.196		
Deswirl Exit	To	1	0.832	0.032 x 0.005 Wall	45˚
		2	0.500		
		3	0.168		

3.2.6 Future Measurements

In the future, additional instrumentation will be added to expand the capability of the current compressor. Windows will be installed in the shroud to acquire LDV measurements. Also, a once-per-rev probe will be mounted at the inducer to facilitate fast response signal processing in addition to tracking individual blades from the tip clearance probes. A Hood Technology Opt-7F200-Spot-3m-350C fiber optical sensor will be used, Figure 3.20. The sensor will be mounted using a MPG-062-A-V CONAX vacuum sealing gland at the inlet of the compressor. The system will need to incorporate anti-reflective paint at the inducer to acquire the once-per-rev signal.

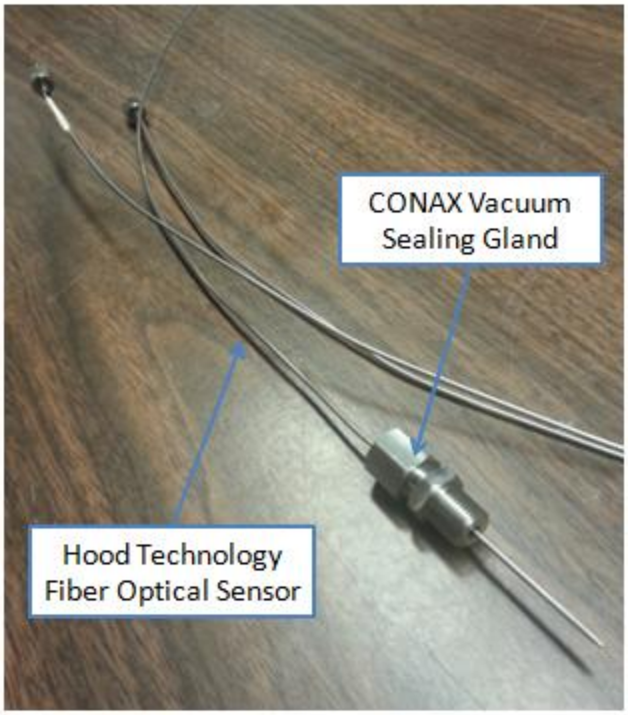

Figure 3.20: Fiber optical sensor to be used for once-per-rev measurement.

3.3 Control Systems

There are five major systems in the facility that require control. These systems include the heat exchangers, the scavenge pump, the compressor throttle, the oil system throttle, and the AC motor. The heat exchangers and scavenge pump can be considered passive control items and were discussed in detail in the health monitoring instrumentation section. The compressor throttle, oil system throttle, and AC motor are active control items because the operator will control them during operation, and they are discussed below.

3.3.1 Compressor Throttle

The compressor throttle controls the mass flow rate through the CSTAR compressor by providing a back pressure to the system. During operation of the compressor, closing the throttle will reduce the flow rate, placing the compressor closer to stall. In the case of stall or surge, the throttle must be rapidly opened to its fully opened position.

This process is controlled using a Fieldvue DVC2000 Digital Valve Controller. The controller interfaces with the LabVIEW Performance Front Panel through the NI CB-68 LP device. The NI CB-68 LP provides a 0-10V output signal to an APD 4380 DC-to-DC transmitter that converts it to a 4-20mA signal that sets the position of the throttle. The controller is capable of holding the throttle position to within 0.5% of its full range of motion. The position is validated using a feedback signal from the digital valve controller. This is a 4-20mA signal and the NI CB-68 LP is only capable of reading a voltage. A simple circuit with a 465 ohm resistor allows the NI CB-68 LP to read the current signal from the controller as a voltage. When the throttle is in the 100% open position, the feedback will send a 4 mA through the circuit and generate a voltage potential across the resistor that can be read by the computer. When the computer reads that the throttle is at the 100% open position a 12 VDC signal is sent to a green LED indicator at the control station. Also located at the control station is a red emergency-open button. In the case of stall or surge, pressing this button will send a 6 VDC signal to LabVIEW, which then sets the throttle to the 100% open position in a matter of seconds.

3.3.2 Oil System Throttle

As discussed previously in the oil section of Chapter 2, a throttle system is used to control the flow of air down the back of the impeller. This system consists of a Swagelok SS-1RS6 needle valve and an ETI VK21-259-V electronic actuator. The electronic actuator requires a 0-10V signal for position control and provides a 0-10V signal for position feedback. The valve is fully-closed at 10V and fully-open at 0V. The throttle system is controlled in the LabVIEW Performance Front Panel through the NI CB-68 LP.

3.3.3 AC Motor

The AC motor is controlled from a pedestal outside of the test cell. The pedestal can be used to change the speed of the motor as well as monitor feedback from the motor. This feedback includes motor speed, power, torque, current, voltage, and frequency. Currently, the only parameters monitored are motor speed, power, and torque. The pedestal also contains a digital display that indicates the current run time of the motor for maintenance purposes. The oil should be changed every 2500 hours of operation or every six months, whichever occurs first. In the event that a pressure or temperature switch triggers the motor to shut down or the Emergency Stop located on the pedestal is pressed, the drive has been programmed to decelerate from full speed to 0 rpm in 10 seconds, reducing the damage to critical components.

3.3.4 Additional Control Mechanisms

Additional components of the control system include the three-way and two-way valves that have been mentioned previously. The three-way valve allows the oil to bypass the outside heat exchangers. Because the three-way valve is a variable valve it will be possible in the future to create a program in LabVIEW that will control the temperature of the oil precisely by varying how much oil is sent to the heat exchangers for cooling, diverting the rest directly to the gearbox and compressor. This will take the place of the thermostat currently being used to control the heat exchanges and allow more precise control of the oil temperature.

The two-way valve is a simple open/close mechanism that controls the oil supply to the compressor. It permits the facility to lubricate the gearbox while withholding oil from the compressor. It is operated by a 120 VAC switch at the control center. In the event that it loses power, it will automatically close and cut off oil to the compressor.

CHAPTER 4 : BASELINE SHROUD VALIDATION

4.1 Motivation

Future plans to incorporate LDV optical access in the CSTAR compressor will require modifications to the shroud and diffuser. To ensure that the performance and integrity of the compressor is not compromised by these modifications, a comprehensive stress and deflection analysis is required. Before an analysis can be performed to determine the stress and deflection that results from the introduction of optical access, a baseline for comparison must first be established and validated. Such a baseline will demonstrate confidence in the procedure utilized to perform a finite element analysis and provide a control group to observe changes in tip clearance deflections that result from the shroud and diffuser modifications.

Resources available to validate a baseline comparison include a 2D finite element analysis (FEA) that was performed on the compressor assembly by a third party during its design phase, ANSYS Mechanical to perform new FEA simulations, and SolidWorks to construct baseline assemblies. The 2D compressor assembly analysis that was originally performed provides the predicted deflection and stress of the assembly for a max hot day (MHD) environment when ambient temperatures are 105°F at 105% speed. At this condition, the compressor temperature and pressure rise will be at the upper limit of what will realistically occur. The high temperature and pressure associated with running the compressor at 105% speed on a max hot day will result in the largest thermal growth and tip clearance change making it the ideal operating condition to validate the baseline and LDV window design. Unfortunately, a 2D analysis cannot be used to validate the LDV window design due to the asymmetric nature of a compressor assembly that incorporates optical access. The 2D analysis, however, can validate a 3D baseline analysis, which in turn can be utilized to validate the LDV window design.

4.2 Sub-assembly Decoupling

Due to the intense computational time and power that would be required to run a 3D analysis on the full compressor assembly, an analysis on a sub-assembly of the compressor was performed. The geometry used in the original third party 2D analysis is shown in Figure 4.1. The pertinent components selected to be part of the sub-assembly analysis are depicted in Figure 4.2 and include the shroud, abraidable, shim, and forward diffuser. The abraidable is a coating applied to shroud that will reduce blade damage if contact occurs between the shroud and the impeller. To represent the influence that the remainder of the assembly has on the sub-assembly components, seven points of deflection on the rear face of the forward diffuser were measured from the third party 2D analysis and applied to the sub-assembly in the form of displacement constraints. Figure 4.3 depicts the location of the seven displacement constraints, and Table 4.1 shows the radial and axial deflection of each constraint as measured in Figure 4.3.

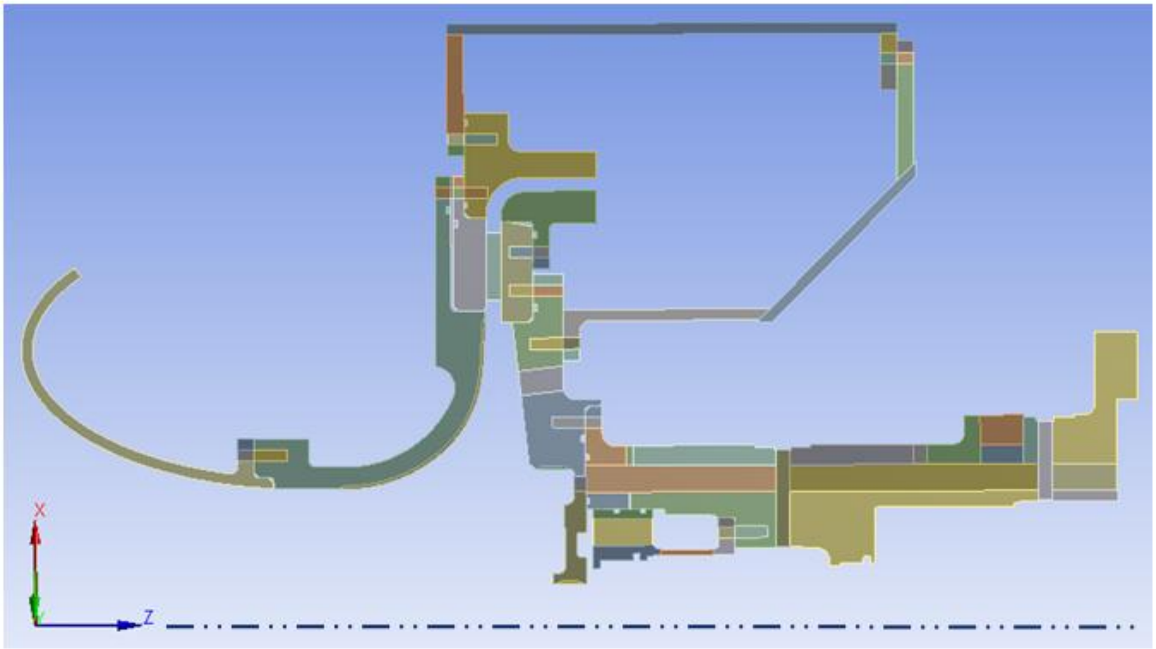

Figure 4.1: Full assembly 2D geometry used in third party analysis.

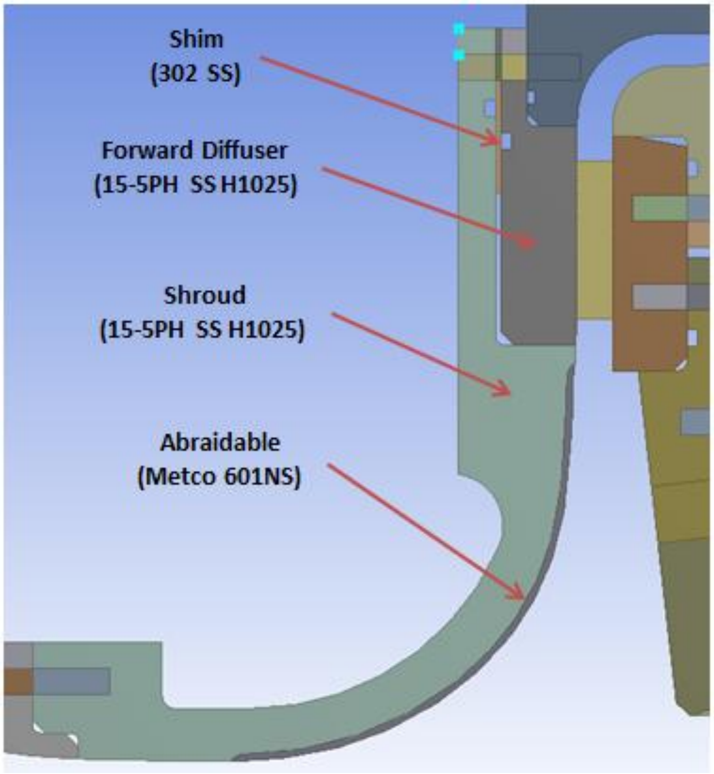

Figure 4.2: Pertinent geometry selected to be used as part of a sub-assembly analysis.

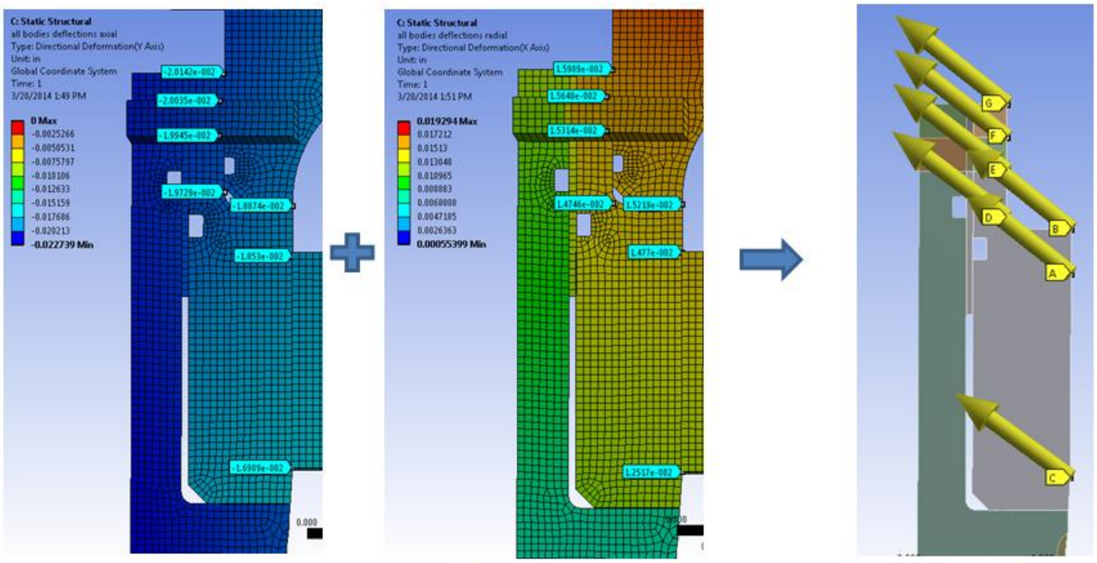

Total forward diffuser axial deflection

Total forward diffuser radial deflection

Seven displacement constraints applied to rear face of forward diffuser

Figure 4.3: Methodology used to predefine the deflection of the rear face of the forward diffuser.

Table 4.1: Axial and radial deflection along the rear face of the forward diffuser.

Location	Axial Deflection (in)	Radial Deflection (in)
A	-1.8530E-02	1.4770E-02
B	-1.8874E-02	1.5219E-02
C	-1.6989E-02	1.2517E-02
D	-1.9729E-02	1.4746E-02
E	-1.9943E-02	1.5314E-02
F	-2.0041E-02	1.5648E-02
G	-2.0138E-02	1.5989E-02

To validate this process, an ANSYS 2D sub-assembly simulation including only the pertinent components was created using the temperature and pressure loading conditions from the third party 2D full assembly analysis. The only difference between the two simulations, besides the geometry, was the use of the displacement constraints. Eight points at various positions on the shroud were selected to monitor and compare deflections between the two analyses. The tightest tooling tolerance on the shroud is +/- 0.001". As long as the difference in deflection between the two assemblies is less than +/- 0.001", it will be assumed that the deflection between the two models is equivalent. Figure 4.4 shows the eight points on the 2D sub-assembly that were monitored for changes in deflection, and Table 4.2 shows the resulting difference in axial and radial deflection between the two assemblies. Because the differences are less than 0.001", the use of displacement constraints to model the deflections that result from contact between the sub-assembly and the full assembly components is valid.

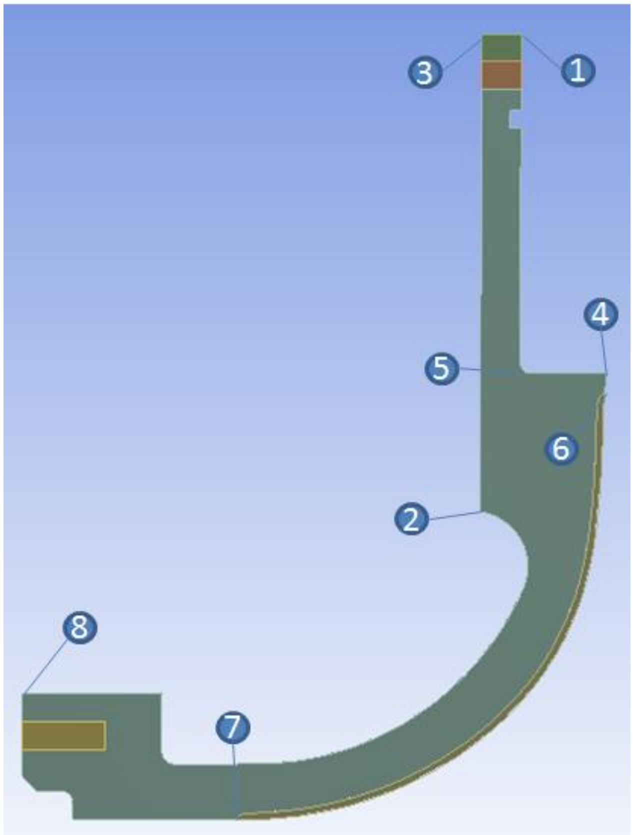

Figure 4.4: Eight locations on the shroud 2D sub-assembly were monitored for changes in deflection.

Table 4.2: The difference in deflections between the third party full assembly and sub-assembly.

Location	Axis	Third Party Full ASM (in)	Third Party Sub-ASM (in)	Delta (in)
1	Axial	-2.0545E-02	-2.0555E-02	1.00E-05
	Radial	1.2255E-02	1.2248E-02	7.00E-06
2	Axial	-2.1613E-02	-2.1558E-02	-5.50E-05
	Radial	6.2346E-03	6.2205E-03	1.41E-05
3	Axial	-2.1041E-02	-2.1049E-02	8.00E-06
	Radial	1.2136E-02	1.2126E-02	1.00E-05
4	Axial	-1.9827E-02	-1.9789E-02	-3.80E-05
	Radial	7.8133E-03	7.8160E-03	-2.70E-06
5	Axial	-2.0982E-02	-2.0940E-02	-4.20E-05
	Radial	7.8554E-03	7.8430E-03	1.24E-05
6	Axial	-1.9859E-02	-1.9812E-02	-4.70E-05
	Radial	7.5421E-03	7.5404E-03	1.70E-06
7	Axial	-1.9794E-02	-1.9739E-02	-5.50E-05
	Radial	7.8185E-04	8.0763E-04	-2.58E-05
8	Axial	-2.0234E-02	-2.0329E-02	9.50E-05
	Radial	1.0270E-03	8.3473E-04	1.92E-04

4.3 2D Baseline Validation

The 2D geometry used by the third party to perform a full assembly FEA is not identical to the as-built geometry of the compressor assembly. Some critical differences featured in the as-built geometry include a flange extension from 1.25 inches to 1.96 inches at the front of the shroud to mount the LCSmith and a shim with a larger inner diameter of 17.77 inches. Moving forward, it was assumed that these geometric differences would not have a significant impact on sub-assembly decoupling permitting the continued use of the seven displacement constraints discussed previously.

Due to the differences between the third party geometry and the as-built geometry, it is necessary to demonstrate that a 2D sub-assembly baseline consisting of the as-built geometry can be properly set up and validated before constructing the 3D baseline. Developing this 2D baseline will provide confidence that the methods and constraints used to set up the ANSYS simulation are valid for predicting deflections in the compressor that are consistent with the third party FEA. Once this is demonstrated, identical procedures can be implemented to generate the 3D baseline FEA.

4.3.1 2D Baseline Geometry and ANSYS Contact Set Up

The initial 2D sub-assembly geometry to be used as a 2D baseline was constructed in SolidWorks from the as-built solid models. To reduce the time to perform the FEA, small features such as fillets, static taps, and forward flange bolt holes were removed. Two shims were also generated for the 2D baseline, one identical to the third party geometry and the other identical to the as-built geometry. The third party shim featuring the smaller 17" inner diameter was used in the sub-assembly to validate temperature and pressure profiles between the third party analysis and the 2D baseline analysis. The final baseline, however, incorporated the as-built shim with an inner diameter of 17.77" to be representative of the delivered compressor.

The contact settings used in ANSYS are identical to the settings used in the third party analysis. These contacts are depicted in Figure 4.5 and include: frictionless contact between the non-fastener sections of the shroud, shim, and diffuser; no separation contact at the fastener interfaces; and a bonded contact between the shroud and abraidable. Plane stress behavior was applied to the fastener features and axisymmetric behavior was applied to the remaining features. The plane stress width (t_{plane}) is determined by calculating an equivalent length of the material between all fastener holes and can be shown to be,

$$t_{plane} = \pi\left(2r_{mean} - \frac{nd}{4}\right), \tag{4.1}$$

where r_{mean} is the radius of the bolt circle, d is the diameter of the bolt, and n is the number of bolts. Additionally, the as-built geometry incorporates an interference fit between the shroud and diffuser at the radial pilot. To model this interference fit in ANSYS, the inner diameter of the forward diffuser was trimmed to match the shroud pilot and an interface treatment offset of 0.004" was applied in the frictionless contact setting between the two interfaces.

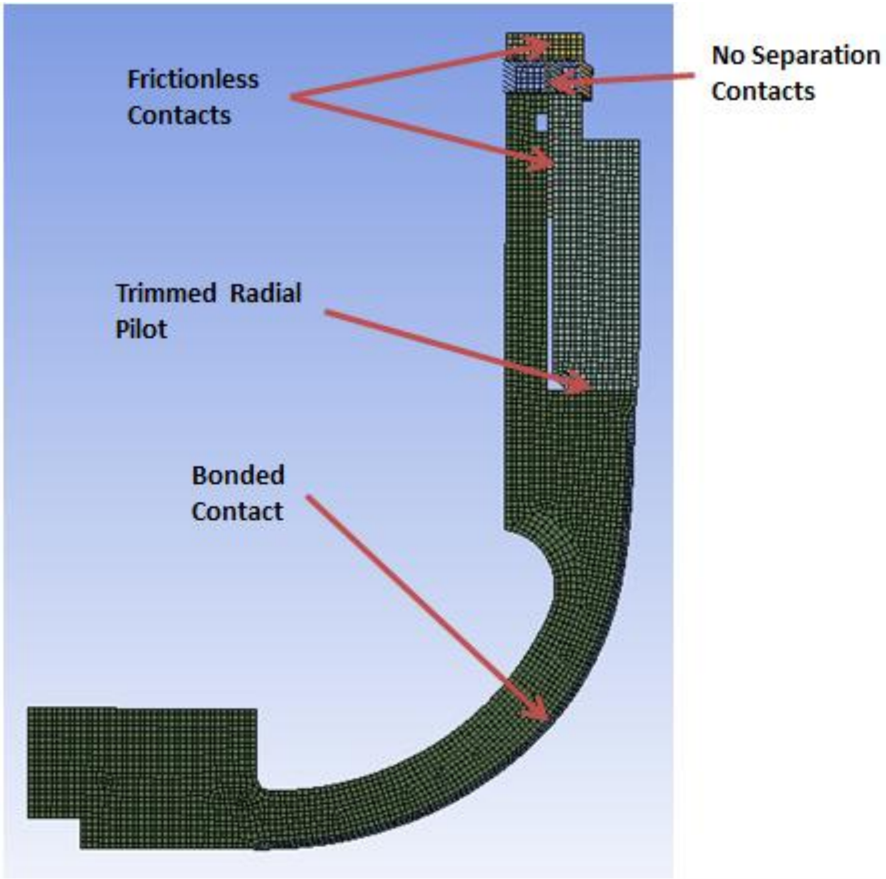

Figure 4.5: ANSYS contact set up for the 2D sub-assembly analysis.

4.3.2 Pressure Profile Validation

The original flow path pressure profile utilized by the third party in their 2D analysis was derived from the sponsor's CFD simulation. Unfortunately, it would be challenging to apply this quasi-continuous 2D pressure profile to a 3D assembly in which the optical elements of the shroud side of the flow path are constantly changing during iterations in the design process. This makes it necessary to develop an alternative form of the pressure profile that can be implemented easily at both the 2D and 3D level.

To accomplish this, the quasi-continuous 2D pressure profile was broken up into 12 constant pressure segments, with the pressure at each segment defined as the average of the corresponding portion of the quasi-continuous pressure profile. This process is illustrated in Figure 4.6. The pressure profile along the rear face of the forward diffuser was neglected for two reasons. First, the forward diffuser is brazed to the rear diffuser. Assuming that the pressure on the rear face of the forward diffuser is equivalent to the pressure at the forward face of the rear diffuser, the resulting net force would be nearly zero. The equivalence of these two pressure distributions is observed in Figure 4.7. The second reason the pressure distribution was neglected is that the deflection at the rear face of the forward diffuser is predefined by the seven displacement constraints depicted in Figure 4.3. Applying a pressure loading to the rear face would not change the deflection of the assembly.

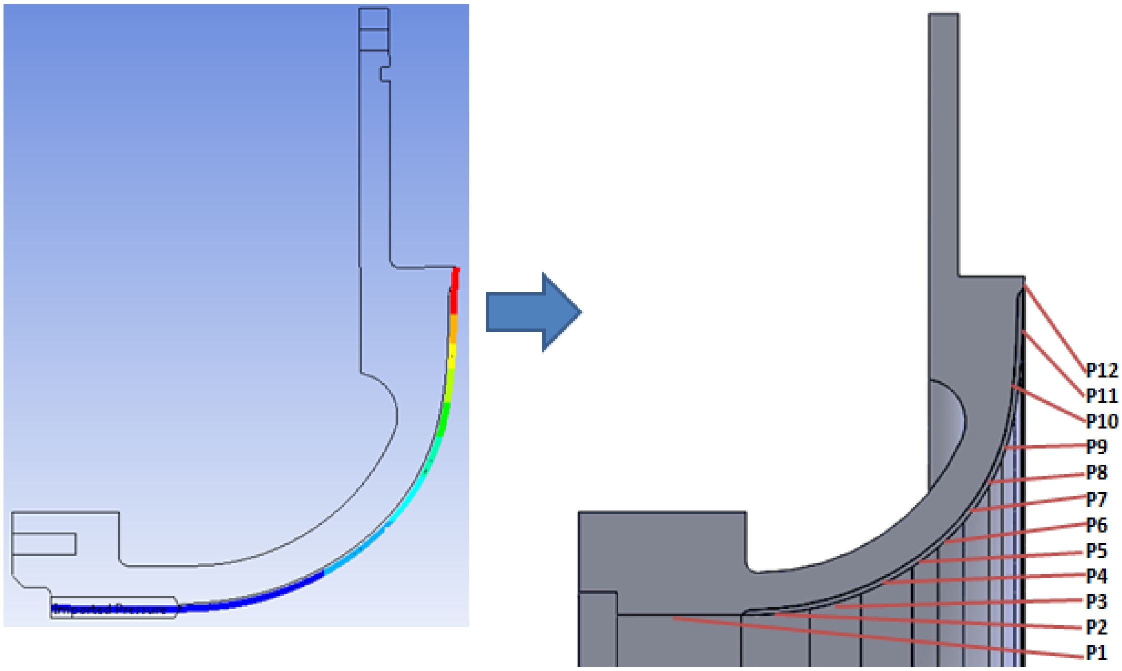

2D CFD Predicted Pressure Profile

Resultant Baseline Pressure Profile (12 line segments)

Figure 4.6: 2D baseline pressure profile development from CFD quasi-continuous pressure profile.

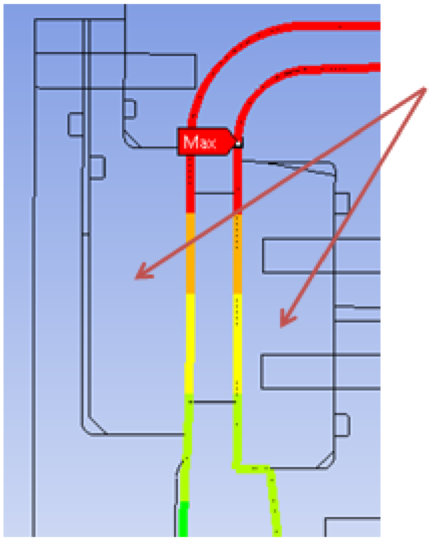

Forward and Aft diffuser sections are brazed together

Figure 4.7: Pressure profile along the diffuser faces as predicted by the third party full assembly analysis.

To validate the proposed 2D baseline pressure profile, two ANSYS simulations were set up featuring sub-assemblies of both the third party geometry and the proposed 2D baseline geometry. Only pressure loading was applied to the sub-assembly models; the quasi-continuous profile to the third party geometry and the 12 pressure segments to the 2D baseline geometry. The difference in deflection between the two simulations is shown in Table 4.3. Because the difference in deflection is less than the 0.001" tooling tolerance, the use of the 12 pressure segments is assumed to be representative of the quasi-continuous pressure profile predicted by CFD.

Table 4.3: The difference in deflection between the third party sub-assembly and the 2D baseline sub-assembly when only pressure loading is applied.

Location	Axis	Third Party 2D Sub-ASM (in)	2D Baseline Sub-ASM (in)	Delta (in)
1	Axial	1.4697E-04	1.5197E-04	-5.00E-06
	Radial	-3.2380E-04	-3.5711E-04	3.33E-05
2	Axial	-6.5765E-03	-6.5320E-03	-4.45E-05
	Radial	2.6680E-05	-9.9934E-06	3.67E-05
3	Axial	1.4860E-04	1.5364E-04	-5.04E-06
	Radial	-1.7335E-04	-1.9847E-04	2.51E-05
4	Axial	-3.9826E-03	-4.0456E-03	6.30E-05
	Radial	-2.2363E-03	-2.2444E-03	8.10E-06
5	Axial	-4.0099E-03	-4.0799E-03	7.00E-05
	Radial	-7.0019E-04	-7.1119E-04	1.10E-05
6	Axial	-4.3042E-03	-4.3087E-03	4.50E-06
	Radial	-2.2385E-03	-2.2347E-03	-3.80E-06
7	Axial	-9.7748E-03	-9.7419E-03	-3.29E-05
	Radial	6.3056E-05	5.3400E-05	9.66E-06
8	Axial	-9.8264E-03	-9.7974E-03	-2.90E-05
	Radial	-2.8551E-05	-3.1203E-05	2.65E-06

4.3.3 Temperature Profile Validation

Like the pressure profile, the temperature profile used in the third party analysis cannot be easily applied to 3D geometry. In place of the quasi-continuous temperature profile, a modified temperature profile was developed that consists of 19 constant temperature segments. The temperature of each segment was determined by averaging the temperature of the corresponding quasi-continuous segment. Unlike the pressure profile, the modified temperature profile includes the rear face of the forward diffuser. In addition, to the flow path temperature profile, a free convection boundary condition was applied to all surfaces exposed to ambient conditions. The coefficient of convection, h, of:

$$h = 1.93E - 5\frac{BTU}{s\ in^2 {}^\circ F}, \tag{4.2}$$

taken from the third party analysis, was used for this convective boundary condition at 105°F. The temperature profile along the flow path is illustrated in Figure 4.8.

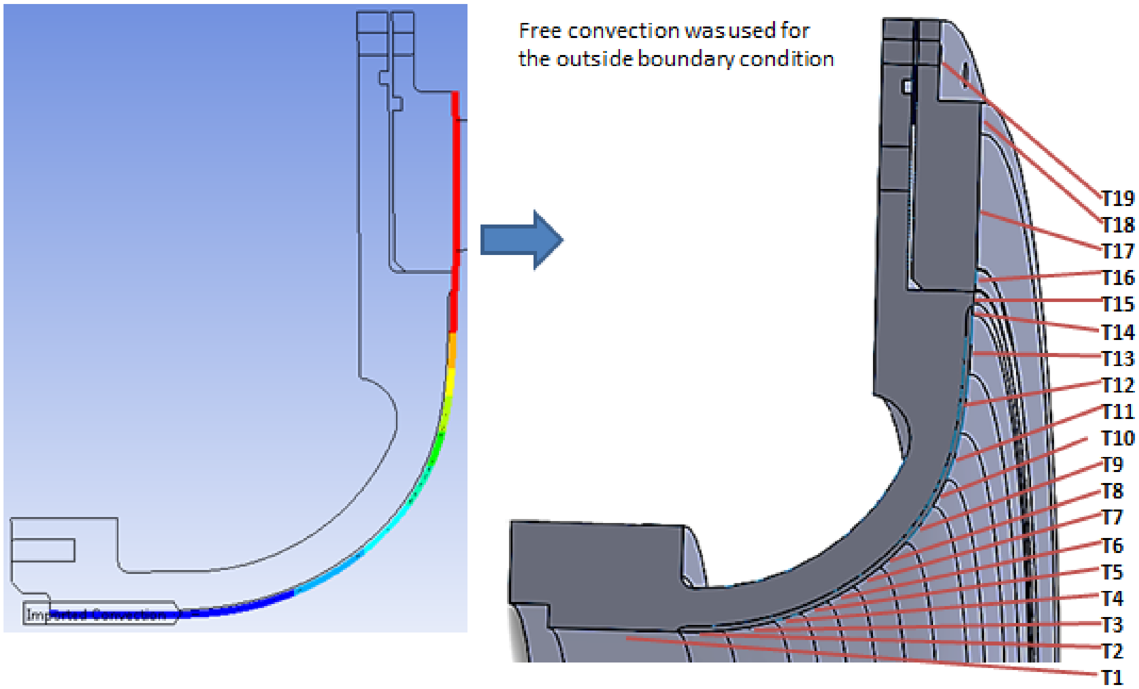

2D CFD Predicted Temperature Profile

Resultant Baseline Temperature Profile (19 line segments)

Figure 4.8: Development of 2D baseline temperature profile from CFD predicted quasi-continuous temperature profile.

To validate the proposed 2D baseline temperature profile, two ANSYS simulations were set up and run between the third party sub-assembly and the 2D baseline sub-assembly. Only temperature loading was applied in each simulation; quasi-continuous profile for the third party sub-assembly and the proposed 2D baseline profile for the 2D baseline sub-assembly. The difference in deflection from the two simulations is noted in Table 4.4. Because the difference in deflection is less than the tooling tolerance of 0.001", the proposed 2D baseline temperature profile is considered representative of the quasi-continuous temperature profile predicted by CFD.

Table 4.4: The difference in deflection between the third party sub-assembly analysis and the 2D baseline sub-assembly analysis when only temperature loading is applied.

Location	Axis	Third Party 2D Sub-ASM (in)	2D Baseline Sub-ASM (in)	Delta (in)
1	Axial	-2.0582E-02	-2.0608E-02	2.60E-05
	Radial	1.2185E-02	1.2213E-02	-2.80E-05
2	Axial	-2.0357E-02	-2.0345E-02	-1.20E-05
	Radial	6.1137E-03	6.1333E-03	-1.96E-05
3	Axial	-2.1077E-02	-2.1101E-02	2.40E-05
	Radial	1.2027E-02	1.2049E-02	-2.20E-05
4	Axial	-1.8911E-02	-1.8787E-02	-1.24E-04
	Radial	7.9093E-03	7.8804E-03	2.89E-05
5	Axial	-1.9974E-02	-1.9959E-02	-1.50E-05
	Radial	7.8148E-03	7.7814E-03	3.34E-05
6	Axial	-1.8811E-02	-1.8797E-02	-1.40E-05
	Radial	7.6414E-03	7.6558E-03	-1.44E-05
7	Axial	-1.8366E-02	-1.8511E-02	1.45E-04
	Radial	8.0865E-04	8.2432E-04	-1.57E-05
8	Axial	-1.8958E-02	-1.9129E-02	1.71E-04
	Radial	8.3202E-04	8.8070E-04	-4.87E-05

To ensure that no discrepancies exist from using the third party sub-assembly in place of the full third party assembly to validate both the proposed temperature and pressure profiles, a 2D baseline sub-assembly was set up in which both pressure and temperature loading was applied. The resulting deflection from this 2D baseline sub-assembly was then compared to the deflection predicted by the third party full assembly analysis, Table 4.5. The differences in deflection are less than the tooling tolerance of 0.001", indicating a high level of confidence that the proposed 2D baseline loading conditions are representative of the loading conditions predicted by CFD.

Table 4.5: The difference in deflection between the third party sub-assembly analysis and the 2D baseline sub-assembly analysis with both pressure and temperature loading.

Location	Axis	Third Party 2D Sub-ASM (in)	2D Baseline Sub-ASM (in)	Delta (in)
1	Axial	-2.0545E-02	-2.0560E-02	1.50E-05
	Radial	1.2255E-02	1.2263E-02	-8.00E-06
2	Axial	-2.1613E-02	-2.1718E-02	1.05E-04
	Radial	6.2346E-03	6.2500E-03	-1.54E-05
3	Axial	-2.1041E-02	-2.1055E-02	1.40E-05
	Radial	1.2136E-02	1.2150E-02	-1.40E-05
4	Axial	-1.9827E-02	-1.9910E-02	8.30E-05
	Radial	7.8133E-03	7.7749E-03	3.84E-05
5	Axial	-2.0982E-02	-2.1080E-02	9.80E-05
	Radial	7.8554E-03	7.8166E-03	3.88E-05
6	Axial	-1.9859E-02	-1.9942E-02	8.30E-05
	Radial	7.5421E-03	7.6102E-03	-6.81E-05
7	Axial	-1.9794E-02	-2.0068E-02	2.74E-04
	Radial	7.8185E-04	8.2551E-04	-4.37E-05
8	Axial	-2.0234E-02	-2.0688E-02	4.54E-04
	Radial	1.0270E-03	8.7877E-04	1.48E-04

4.3.4 Final 2D Baseline Validation

As mentioned previously, the original third party analysis geometry was not identical to the as-built geometry. To validate the temperature and pressure profile, a shim matching the third party geometry was used in the baseline geometry. Because the shim acts as a pivot point between the shroud and diffuser, the reduced inner diameter of the as-built shim may lead to excessive deflection of the shroud toward the impeller. To verify the differences in deflection that the two shim designs may have is not a concern, an ANSYS simulation using the 2D baseline sub-assembly was performed for each shim. Table 4.6 shows the differences in deflection between the two shim designs. Though the difference in deflection was less than the tooling tolerance of 0.001", the final 2D baseline geometry moving forward will utilize the as-built shim to remain consistent with the actual compressor. The deflections from the simulation that utilized the as-built shim were also compared to the overall third party assembly analysis in Table 4.7. Results show that the difference in deflection is negligible.

Table 4.6: The difference in deflection between the third party shim and the as-built shim.

Location	Axis	17" Shim (in)	17.77" Shim (in)	Delta (in)
1	Axial	-2.0560E-02	-2.0559E-02	-1.00E-06
	Radial	1.2263E-02	1.1988E-02	2.75E-04
2	Axial	-2.1718E-02	-2.1298E-02	-4.20E-04
	Radial	6.2500E-03	6.1310E-03	1.19E-04
3	Axial	-2.1055E-02	-2.1059E-02	4.00E-06
	Radial	1.2150E-02	1.1870E-02	2.80E-04
4	Axial	-1.9910E-02	-1.9686E-02	-2.24E-04
	Radial	7.7749E-03	7.8267E-03	-5.18E-05
5	Axial	-2.1080E-02	-2.0851E-02	-2.29E-04
	Radial	7.8166E-03	7.7395E-03	7.71E-05
6	Axial	-1.9942E-02	-1.9699E-02	-2.43E-04
	Radial	7.6102E-03	7.6014E-03	8.80E-06
7	Axial	-2.0068E-02	-1.9536E-02	-5.32E-04
	Radial	8.2551E-04	8.2436E-04	1.15E-06
8	Axial	-2.0688E-02	-2.0155E-02	-5.33E-04
	Radial	8.7877E-04	8.7975E-04	-9.80E-07

Table 4.7: The difference in deflection between the third party full assembly analysis and the final 2D baseline sub-assembly analysis.

Location	Axis	Third Party Full ASM (in)	2D Baseline Sub-ASM (in)	Delta (in)
1	Axial	-2.0545E-02	-2.0559E-02	1.40E-05
	Radial	1.2255E-02	1.1988E-02	2.67E-04
2	Axial	-2.1613E-02	-2.1298E-02	-3.15E-04
	Radial	6.2346E-03	6.1310E-03	1.04E-04
3	Axial	-2.1041E-02	-2.1059E-02	1.80E-05
	Radial	1.2136E-02	1.1870E-02	2.66E-04
4	Axial	-1.9827E-02	-1.9686E-02	-1.41E-04
	Radial	7.8133E-03	7.8267E-03	-1.34E-05
5	Axial	-2.0982E-02	-2.0851E-02	-1.31E-04
	Radial	7.8554E-03	7.7395E-03	1.16E-04
6	Axial	-1.9859E-02	-1.9699E-02	-1.60E-04
	Radial	7.5421E-03	7.6014E-03	-5.93E-05
7	Axial	-1.9794E-02	-1.9536E-02	-2.58E-04
	Radial	7.8185E-04	8.2436E-04	-4.25E-05
8	Axial	-2.0234E-02	-2.0155E-02	-7.90E-05
	Radial	1.0270E-03	8.7975E-04	1.47E-04

The grid utilized in the FEA to validate the 2D baseline (12,098 nodes) was based off the same refinement level as the third party analysis (11,305 nodes). The grid used for the 2D baseline is illustrated in Figure 4.9. To ensure that both studies were grid independent, a grid refinement study was performed on the 2D baseline sub-assembly. The grid was refined to 46,202 nodes to ensure the deflections remained unchanged. Table 4.8 compares the difference in deflection between the two refinement levels. The magnitude of the differences in deflection are not significant and show that the solution was indeed grid independent at the original level.

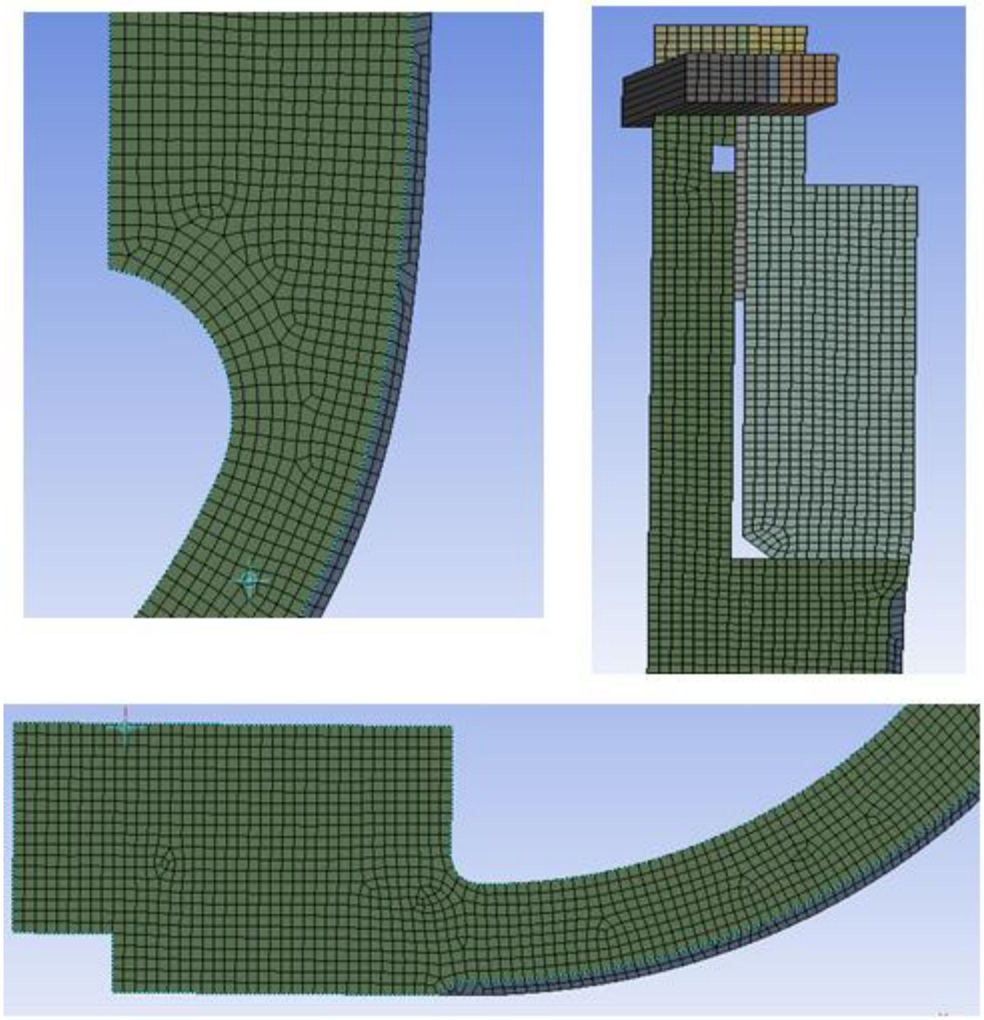

Figure 4.9: Grid used for 2D baseline sub-assembly FEA.

Table 4.8: The difference in deflection at two different grid refinement levels for the 2D baseline sub-assembly FEA.

Location	Axis	12051 Nodes (in)	46202 Nodes (in)	Delta (in)
1	Axial	-2.0559E-02	-2.0559E-02	0.00E+00
	Radial	1.1988E-02	1.2001E-02	-1.30E-05
2	Axial	-2.1298E-02	-2.1324E-02	2.60E-05
	Radial	6.1310E-03	6.1440E-03	-1.30E-05
3	Axial	-2.1059E-02	-2.1061E-02	2.00E-06
	Radial	1.1870E-02	1.1878E-02	-8.00E-06
4	Axial	-1.9686E-02	-1.9690E-02	4.00E-06
	Radial	7.8267E-03	7.8214E-03	5.30E-06
5	Axial	-2.0851E-02	-2.0855E-02	4.00E-06
	Radial	7.7395E-03	7.7471E-03	-7.60E-06
6	Axial	-1.9699E-02	-1.9703E-02	4.00E-06
	Radial	7.6014E-03	7.6329E-03	-3.15E-05
7	Axial	-1.9536E-02	-1.9571E-02	3.50E-05
	Radial	8.2436E-04	8.2459E-04	-2.30E-07
8	Axial	-2.0155E-02	-2.0189E-02	3.40E-05
	Radial	8.7975E-04	8.7984E-04	-9.00E-08

The validated 2D baseline model provides confidence in a methodology that can be applied to develop and validate a 3D baseline. The validated 2D baseline sub-assembly geometry consists of the shroud, the forward diffuser, the shim, and the abraidable. Key features of this methodology include seven displacement constraints to predefine the deflection of the forward diffuser, a pressure profile comprising of 12 constant pressure panels, a temperature profile comprising of 19 constant temperature panels with free convection applied on surfaces exposed to the ambient environment, and the as-built shim. The ANSYS setup features a trimmed forward diffuser inner diameter with a 0.004" interface treatment offset, and all contacts are frictionless except at fastener interfaces which have a no-separation condition and the bonded interface between the shroud and abraidable. The results presented in this section demonstrate a high level of confidence in the use of this FEA set up to procure a representative 3D baseline.

4.4 3D Baseline Model Validation

A 3D baseline shroud model is required to verify that the deflections resulting from the addition of LDV optical access will not lead to flow path changes. Excessive deflections would result in non-uniform tip clearances that could change the characteristics of the flow. The methodology developed to validate the 2D baseline in the previous section can be directly applied to generate the 3D baseline.

The geometry used for the 3D baseline is identical to the 2D baseline; consisting of the as-built shroud, forward diffuser, shim, and abraidable. Small features such as static pressure taps, fastener holes, and the cap probe holes were also removed to reduce ANSYS computational time. The contacts and settings used in ANSYS also were identical to the 2D baseline analysis, with the addition of a fixed tangential displacement constraint applied to the outer diameters of the shroud, shim, and diffuser to prevent the assembly from rotating freely. To apply the 2D baseline temperature and pressure profile to the 3D baseline, split lines were created in the solid models that break up the flow path surface permitting it to be a selectable feature in ANSYS. Figure 4.10 illustrates the application of split lines to the abraidable surface of the assembly. Breaking up the surface in this way also generates a reference at eleven radii from the inducer to the exducer in which tip clearance deflections of the shroud can be monitored.

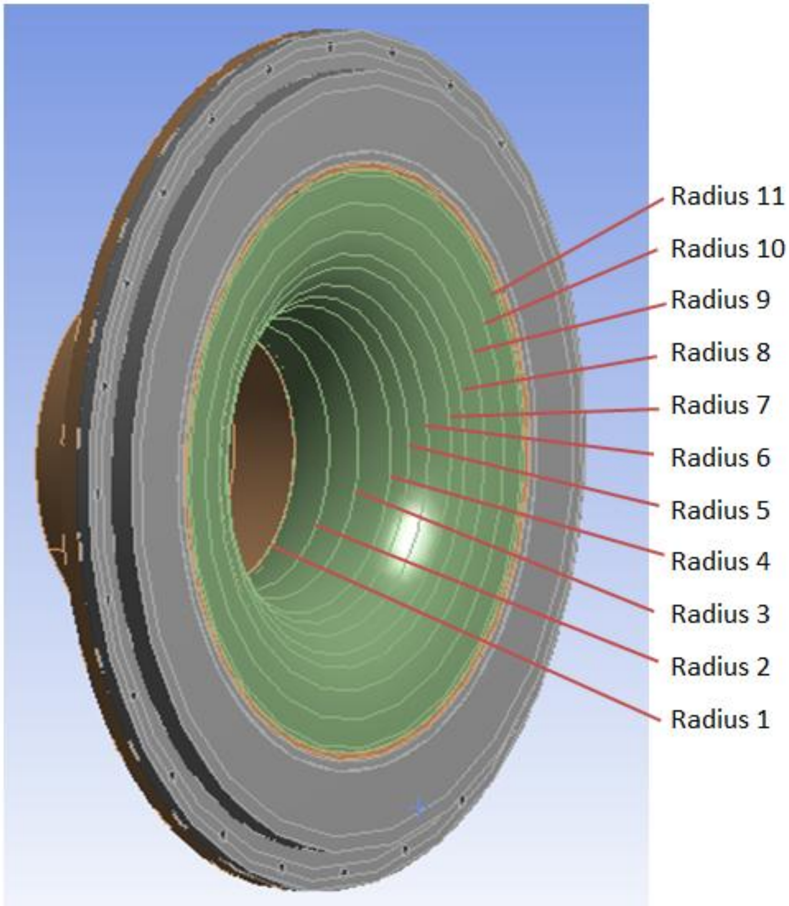

Figure 4.10: The 11 radii depicted from the inducer to the exducer will be used to monitor tip clearance deflection of the shroud.

4.4.1 3D Baseline Grid Refinement Study

A grid refinement study was performed on the 3D baseline assembly to ensure that the deflections predicted by ANSYS were independent of the grid used. Two radii were chosen to show convergence of the solution. These convergence regions include the radial deflection at the inducer (radius 1) and the axial deflection at the exducer (radius 11). Simulations were performed at four different grid refinement levels ranging from 200,000 to 700,000 nodes. A solution that varied less than 2.5E-5 inches would be considered converged. This value is 2.5% of the deflection limit requirements.

Figure 4.11 illustrates the radial deflection at radius 1 and the axial deflection at radius 11 for the four different refinement levels. The study indicates that convergence requirements at radius 1 are met within the first refinement level of 233,157 nodes. The maximum difference in deflection between the four refinement levels is 1.63E-6 inches at radius 1. At radius 11, convergence is met by the 2nd refinement level of 352,463 nodes. The maximum difference in axial deflection after the 2nd refinement level is 1.6e-5 inches.

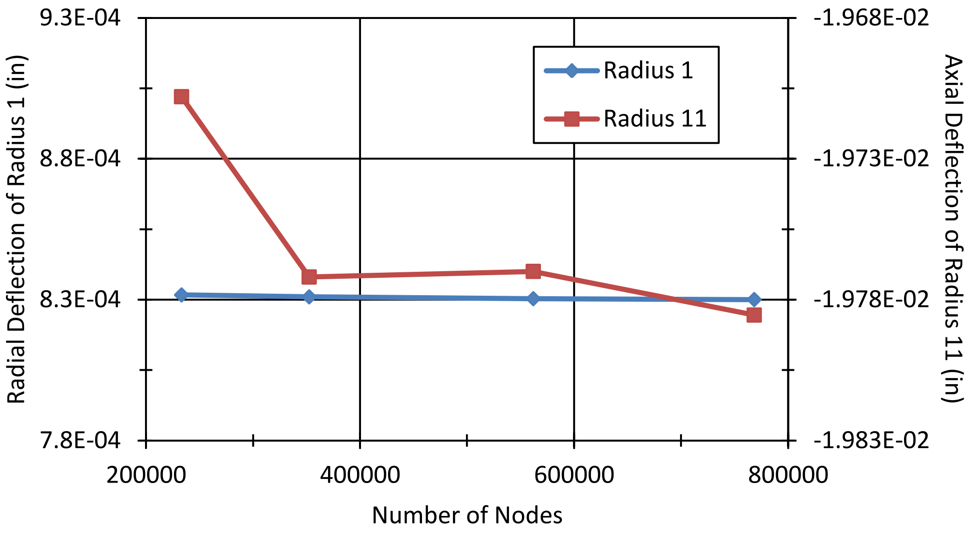

Figure 4.11: 3D grid refinement study performed at the inducer and exducer of the 3D baseline sub-assembly.

Based on grid refinement studies performed at radius 1 and radius 11, convergence of the 3D baseline occurs when the refinement level is greater than 350,000 nodes. Future simulations in ANSYS using the 3D baseline geometry will be assumed to be grid independent when the refinement level is greater than 350,000 nodes. Additionally, the deflection of the 3D baseline geometry at the 4th refinement level was compared to the deflection predicted by the third party full assembly analysis, Table 4.9. Figure 4.12 shows the grid of the 3D baseline sub-assembly at the fourth refinement level. Differences in deflection between the two models are all less than the tooling tolerance of 0.001 inches. This indicates that the methodology and set up for the 3D baseline is representative of the predicted third party FEA. It also means that the proposed 3D baseline can be compared with modified versions of the geometry to determine the deflection of proposed future designs with a high level of confidence.

Table 4.9: The difference in deflection between the third party full assembly analysis and the final 3D baseline sub-assembly analysis.

Location	Axis	Third Party Full ASM (in)	3D Baseline Sub-ASM (in)	Delta (in)
1	Axial	-2.0545E-02	-2.0552E-02	7.00E-06
	Radial	1.2255E-02	1.2175E-02	8.00E-05
2	Axial	-2.1613E-02	-2.1672E-02	5.90E-05
	Radial	6.2346E-03	6.3262E-03	-9.16E-05
3	Axial	-2.1041E-02	-2.1050E-02	9.00E-06
	Radial	1.2136E-02	1.2054E-02	8.20E-05
4	Axial	-1.9827E-02	-1.9819E-02	-8.00E-06
	Radial	7.8133E-03	7.7859E-03	2.74E-05
5	Axial	-2.0982E-02	-2.0983E-02	1.00E-06
	Radial	7.8554E-03	7.8638E-03	-8.40E-06
6	Axial	-1.9859E-02	-1.9819E-02	-4.00E-05
	Radial	7.5421E-03	7.5738E-03	-3.17E-05
7	Axial	-1.9794E-02	-2.0060E-02	2.66E-04
	Radial	7.8185E-04	8.4139E-04	-5.95E-05
8	Axial	-2.0234E-02	-2.0687E-02	4.53E-04
	Radial	1.0270E-03	8.9037E-04	1.37E-04

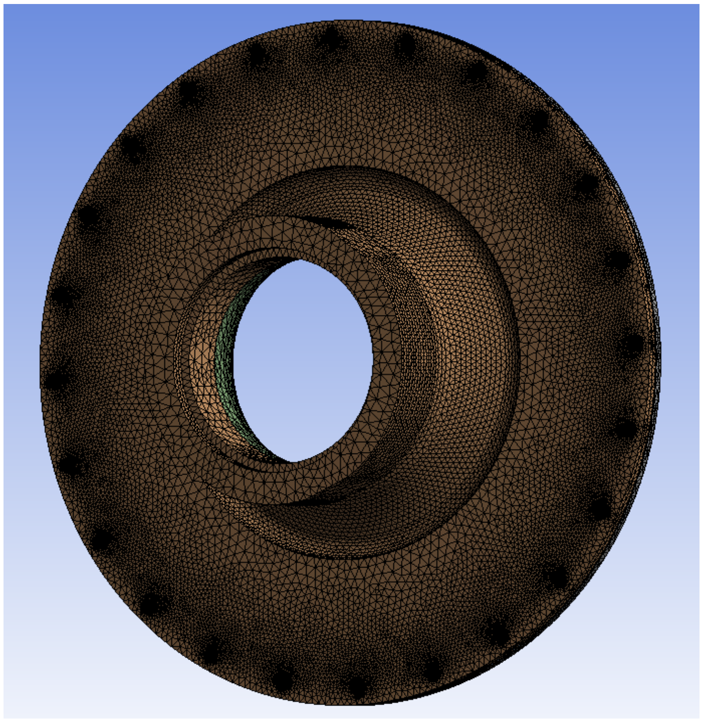

Figure 4.12: 3D baseline sub-assembly grid at the 4th refinement level of 768,358 nodes.

4.4.2 Capacitance Probe Hole Deflection

Because the capacitance probe holes remove a significant amount of material from the shroud, it was necessary to determine the impact that the holes might have on the overall assembly deflection. To determine the extent that the capacitance probe holes affect the shroud, a comparison was made between two 3D baseline models: one with the capacitance probe features and one without the capacitance probe features. Figure 4.13 shows the difference in deflection at each radius from the inducer (radius 1) to the exducer (radius 11). Significant deflection occurs at radius 6 and radius 10. Further investigation reveals that the area in which the excessive deflection occurs is at the knee capacitance probe hole (radius 6) and at the exducer capacitance probe (radius 10).

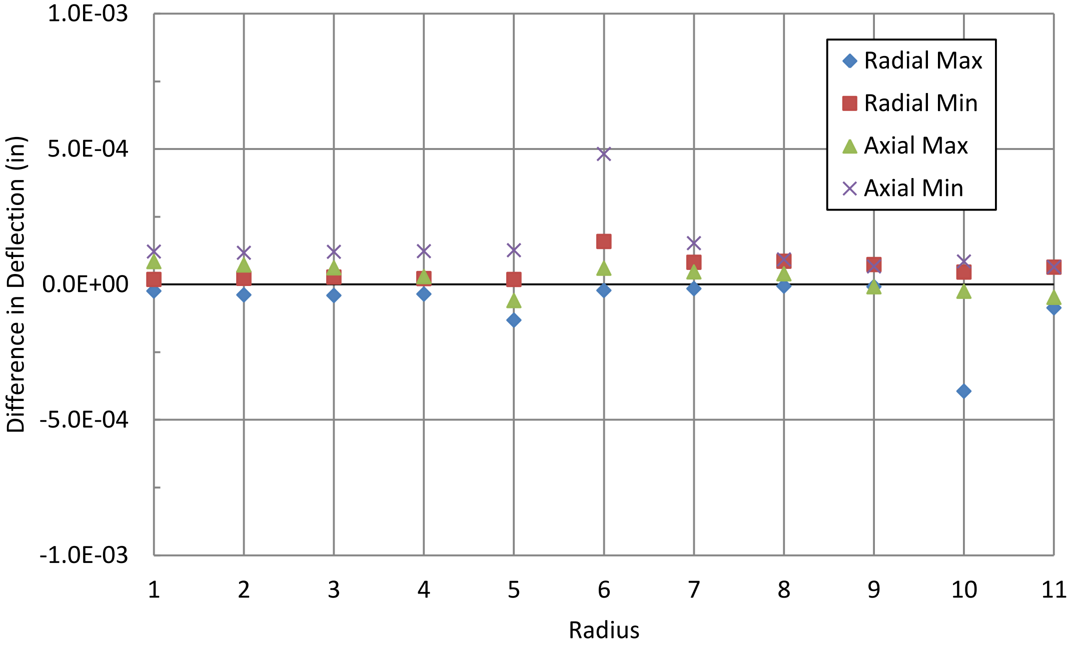

Figure 4.13: The difference in deflection between a 3D baseline featuring capacitance probe holes and a 3D baseline featuring no capacitance probe holes at 11 radii from the inducer to the exducer.

Figure 4.14 and Figure 4.15 show the source of each deflection. The excessive deflection is localized to each capacitance probe hole. A short distance from each hole the deflection converges to the values predicted by the 3D baseline model that does not feature the capacitance probe holes. The difference in deflection a short distance from the knee capacitance probe hole is 8.3e-5 inches and the difference a short distance from the exducer capacitance probe hole is 2.42e-5 inches. Due to the small nature of these deflections and the reduced computational time resulting from the exclusion of capacitance probe holes in the geometry, capacitance probe holes were only modeled in final FEA iterations.

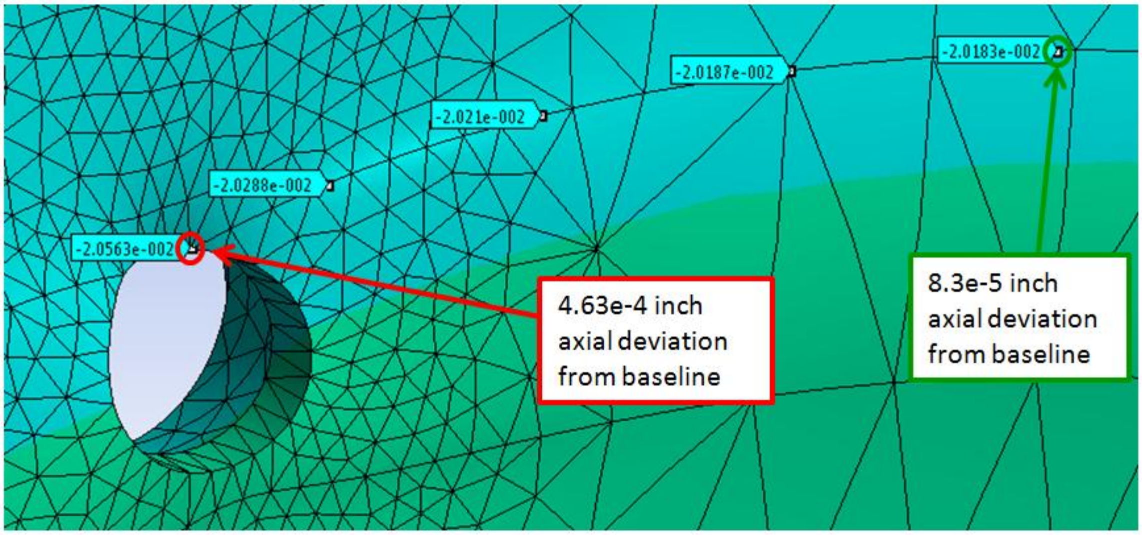

Figure 4.14: Axial deflection at the knee (radius 6).

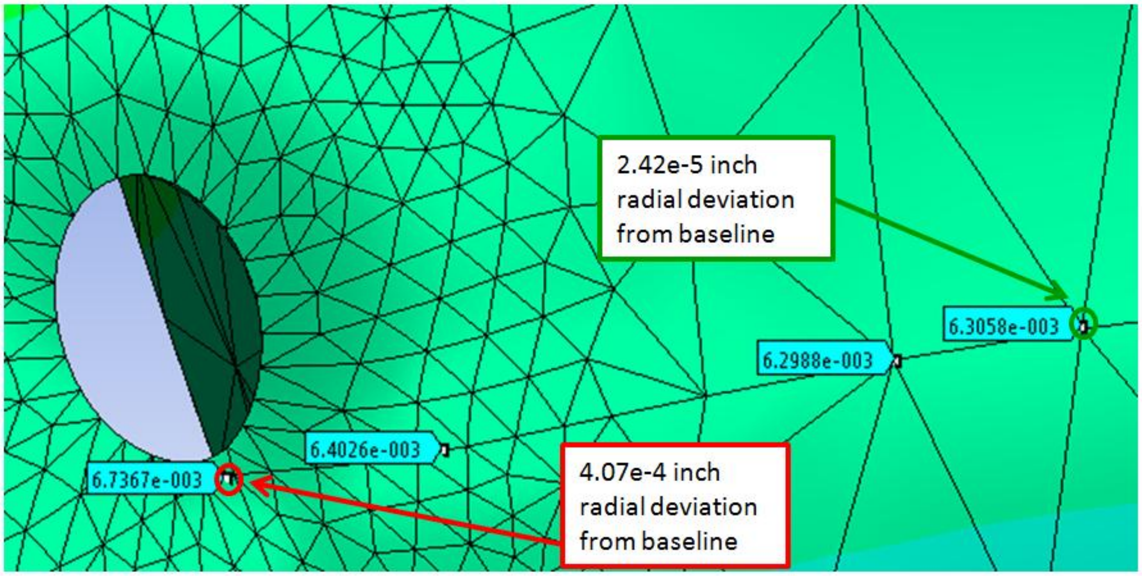

Figure 4.15: Radial deflection at the exducer (radius 10).

CHAPTER 5 : LDV WINDOW DESIGN

5.1 Design Requirements

In future experiments, optical access for the LDV System will be required. The shroud and diffuser will need to be modified and windows will need to be fabricated. There are several key requirements driving the design. First, adequate window width should be considered for the two LDV probes to maximize the viewable area of the compressor while minimizing the relative error from transforming the coordinate system. This is difficult because the relative error is smallest when the two LDV probes are orthogonal to one another, permitting the direct measurement of all three components of the entrained particle velocity; however, it is impossible to design windows that will accommodate such a large angle. Therefore, a compromise must be made between window width and the allowable deflection of the shroud. Second, the tip clearance between the impeller and shroud is very small, 0.007” at the inducer and 0.003” at the exducer. Any window assembly incorporated into the compressor will need to maintain these tight clearances during operation where high temperature and high pressure loads are present. Requirements set by the sponsor are that the deviation in deflection between original assembly and modified assembly from the inducer to the exducer must be within +\- 0.001". Additionally, the stress in the window assemblies and modified components must be less than 80% of the yield stress of the component materials. Table 5.1 specifies the mechanical design requirements for the LDV window design. With these requirements in mind, two designs have been developed to allow LDV access to most of the impeller and two diffuser vane passages.

Table 5.1: Window Mechanical Design Requirements.

<table>
<tr><td colspan="4">Window Requirements</td></tr>
<tr><td colspan="4">Stress Limits</td></tr>
<tr><td>Material</td><td>Type</td><td>Fty (ksi)</td><td>0.8*Fty (ksi)</td></tr>
<tr><td>15-5PH SS</td><td>Compressive/ Tensile</td><td>132</td><td>105.6</td></tr>
<tr><td>Fused Silica SiO2</td><td>Compressive</td><td>160</td><td>128</td></tr>
<tr><td>Fused Silica SiO2</td><td>Tensile</td><td>7</td><td>5.6</td></tr>
<tr><td colspan="4">Deflection and Tolerance Limits</td></tr>
<tr><td colspan="2">Type</td><td>Upper Limit (in)</td><td>Lower Limit (in)</td></tr>
<tr><td colspan="2">Change in Deflection</td><td>0.001</td><td>-0.001</td></tr>
<tr><td colspan="2">Window Machine Tolerance</td><td>0</td><td>-0.002</td></tr>
</table>

5.2 LDV System Specifications

The LDV system intended to be implemented with the CSTAR compressor consists of two backscattering one-dimensional and two-dimensional probes. A 5 Watt argon-ion laser is utilized to generate three different beams with wavelengths (λ) 514.5 nm, 488.0 nm, and 476.5 nm. The probes feature a beam spacing of 38.0 mm, a focal length (F) of 159.8 mm, a beam diameter (D_L) of 2.2 mm, and a beam angle (θ) of 13.56°. The probe volume dimensions (δ_z, δ_y, δ_x), fringe spacing (δ_f), and number of fringes (N_f) are calculated from:

$$\delta_z = \frac{4F\lambda}{\pi \mathrm{D_L} \sin\left(\frac{\theta}{2}\right)}, \tag{5.1}$$

$$\delta_y = \frac{4F\lambda}{\pi \mathrm{D_L}}, \tag{5.2}$$

$$\delta_x = \frac{4F\lambda}{\pi \mathrm{D_L} \cos\left(\frac{\theta}{2}\right)}, \tag{5.3}$$

$$\delta_f = \frac{\lambda}{2\sin\left(\frac{\theta}{2}\right)}, \tag{5.4}$$

and

$$N_f = \frac{8Ftan\left(\frac{\theta}{2}\right)}{\pi \mathrm{D_L}}. \tag{5.5}$$

These LDV specifications for each beam wavelength are denoted in Table 5.2.

Table 5.2: LDV probe volume specifications.

	λ (nm)		
	514.5	488	476.5
δz (mm)	0.4030	0.3823	0.3732
δy (mm)	0.0476	0.0451	0.0441
δx (mm)	0.0479	0.0454	0.0444
δf (um)	2.179	2.067	2.018
Nf	22.0	22.0	22.0

5.3 LDV Window Design Features

The optical access designed for the CSTAR compressor will cover various areas of the flow path from the inducer to the diffuser exit. Multiple configurations have been explored to maximize the amount of access given by each window within the design space. To incorporate the various window assembly designs in the CSTAR compressor, modifications to the shroud and diffuser will be required. These modifications include holes in the shroud and cutouts of the diffuser section.

Two different designs have been explored to obtain optical access in the centrifugal compressor. The first design features three windows; an inducer window, a knee window, and a diffuser window. The second design reduces the amount of windows in the assembly down to two by combining the inducer and knee window into one window. The two window and three window designs are illustrated in Figure 5.1. The advantage of the three window design is that it can be implemented in the current shroud and each individual window should be more easily machined due to the reduction in window aspect ratio. The advantage of the two window design, however, is that by reducing the number of windows the total manufacturing cost may be less, and the design is much cleaner.

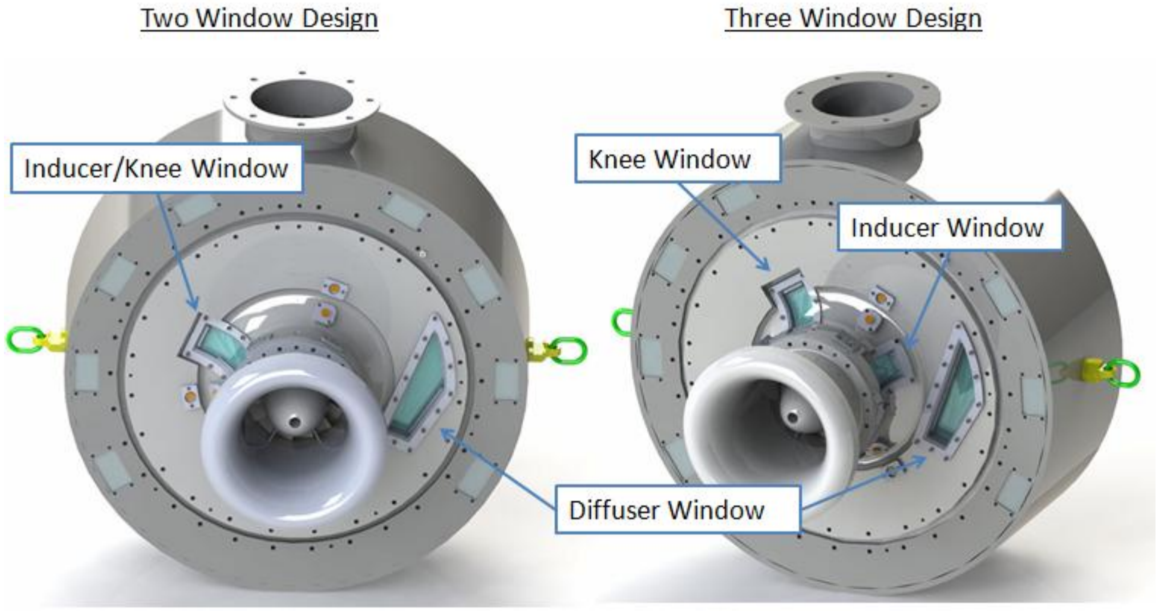

Figure 5.1: The two window and three window design for optical access is shown above.

Each window assembly, though different geometrically, is constructed using the same type of components. These components consist of the window holder, the window, and the window clamps, Figure 5.2. The holder and clamps will be made out of 15-5 stainless steel to remain consistent with the shroud and diffuser materials. The window holder is held flush against the shroud surface by a flange with #8-36 machine screws. This flange also houses a 1/16" O-ring to prevent air from leaking out of the compressor. There is a lip located inside of the holder that acts as a mechanical stop to prevent the window from falling into the compressor. The clamps are used to hold the window against this lip. These clamps are fastened to the inner walls of the window holder frame using #6-40 countersunk machine screws. The window will be made out fused silica because of the material's high strength, low coefficient of thermal expansion, and optimal optical properties. Each window incorporates a lip that complements the lip in the holder. An adhesive will hold the window against the holder to ensure proper sealing of the assembly. Sealant will also be required to seal the screws used to fasten the window clamps. Each window assembly is designed to replicate the contour of the shroud. To ensure that the performance of the compressor is not impacted by varying tip clearances, the tolerance along the flow path surface of this assembly must be +0.000"/-0.002". Each design feature described above is illustrated in Figure 5.3 for the four window designs.

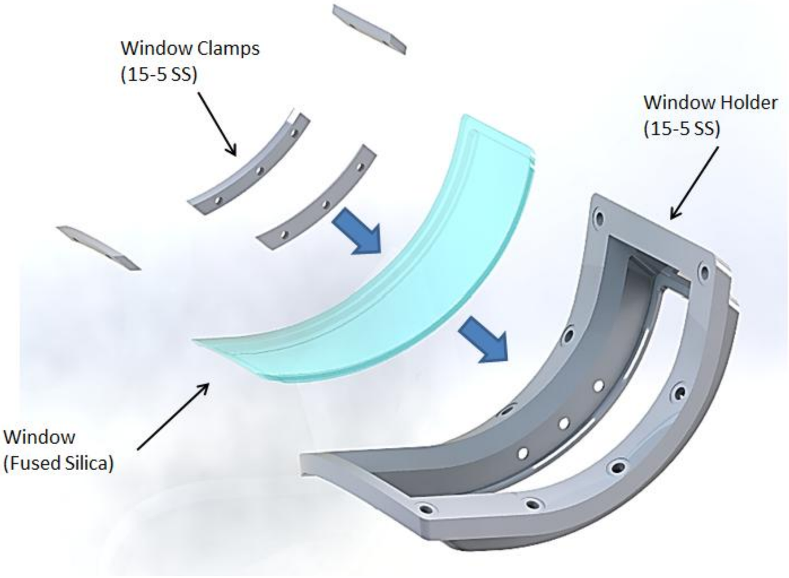

Figure 5.2: Each window consists of the three components; the window, clamps, and window holder.

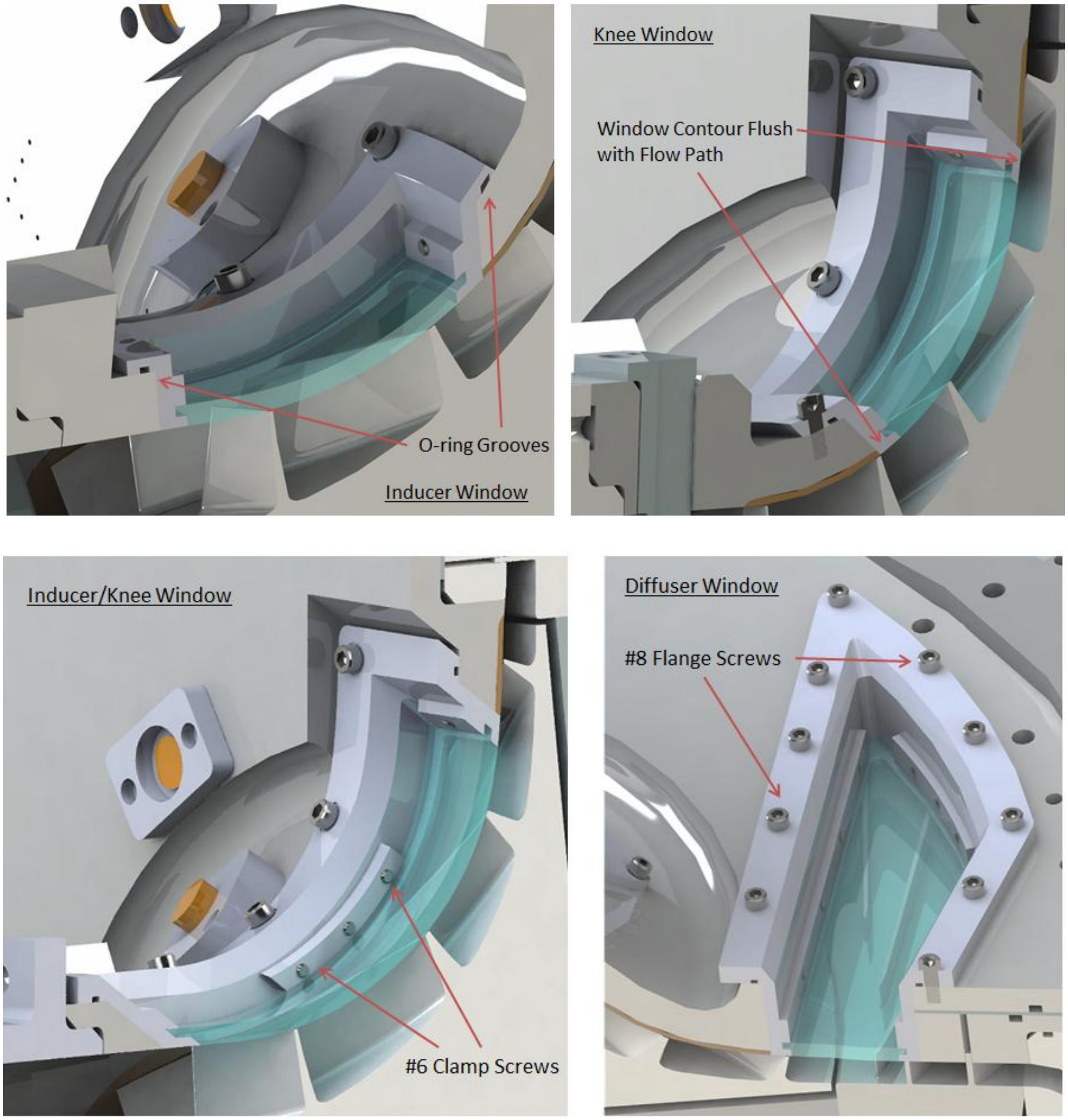

Figure 5.3: The design features are depicted on the section views for the four window designs.

5.4 Finite Element Analysis

To optimize the design of the windows within the design space several aspects of the window assembly design required iterations in ANSYS. The main features of the design that were explored were window clocking, window width, and window thickness. Both the stress and deflection of the assembly was monitored to determine limits within the LDV window design space.

5.4.1 Methodology

The methodology chosen to analyze the deflection in the shroud should maintain a high level of confidence that the deflection is accurately captured. Due to the complexity associated with analyzing every point along the surface of the shroud, an approach was developed to process each FEA at 11 predefined radii along the flow path of the shroud. The deflections at each of these radii are used to infer whether or not deflection requirements have been exceeded.

The following methodology was implemented to analyze the FEA results for the different window configurations. For each radius, window holder trailing edge, and window holder leading edge, the angle normal to the flow path surface was found and used to calculate the actual difference in tip clearance deflection ($\Delta r'$) from the axial and radial deflections as follows:

$$\Delta r' = \Delta r \cdot \cos(\phi) - \Delta z \cdot \sin(\phi) \tag{5.6}$$

where Δr is the difference in radial deflection, Δz is the difference in axial deflection, and ϕ is the angle of the vector normal to the flow path, Figure 5.4.

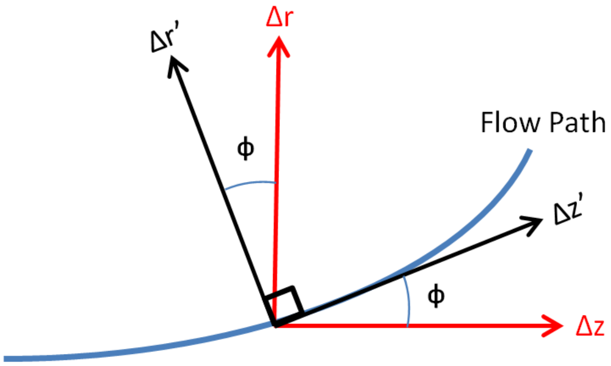

Figure 5.4: The axial and radial deflections were transformed to calculate the difference in tip clearance deflection, Δr'.

The maximum and minimum radial/axial deflections were collected for all 11 radii, Figure 4.10. Though the maximum and minimum radial/axial deflections at each radius may not coincide at the same point, critical possible tip clearance deflections can be predicted by combining these maximum and minimum deflections and used as a tool to determine which radius may have areas that exceed deflection requirements. The minimum radial deflection and maximum axial deflection were combined to predict the minimum tip clearance deflection possible and the maximum radial and minimum axial deflection were combined to predict the maximum tip clearance deflection possible. If either of these values exceeds the deflection requirements, the radius is investigated further to determine the true values of deflection at critical locations to rule out false positives. Points found to exceed deflection requirements using this methodology are discussed in the following sections.

5.4.2 Window Clocking

There are several possible clocking configurations that the windows can be set at. An ideal configuration will clock the windows in positions that reduce the overall deflection of the shroud. Two different clocking configurations were studied for both the three window and two window designs to determine the impact clocking has on the deflection of the shroud, Figure 5.5.

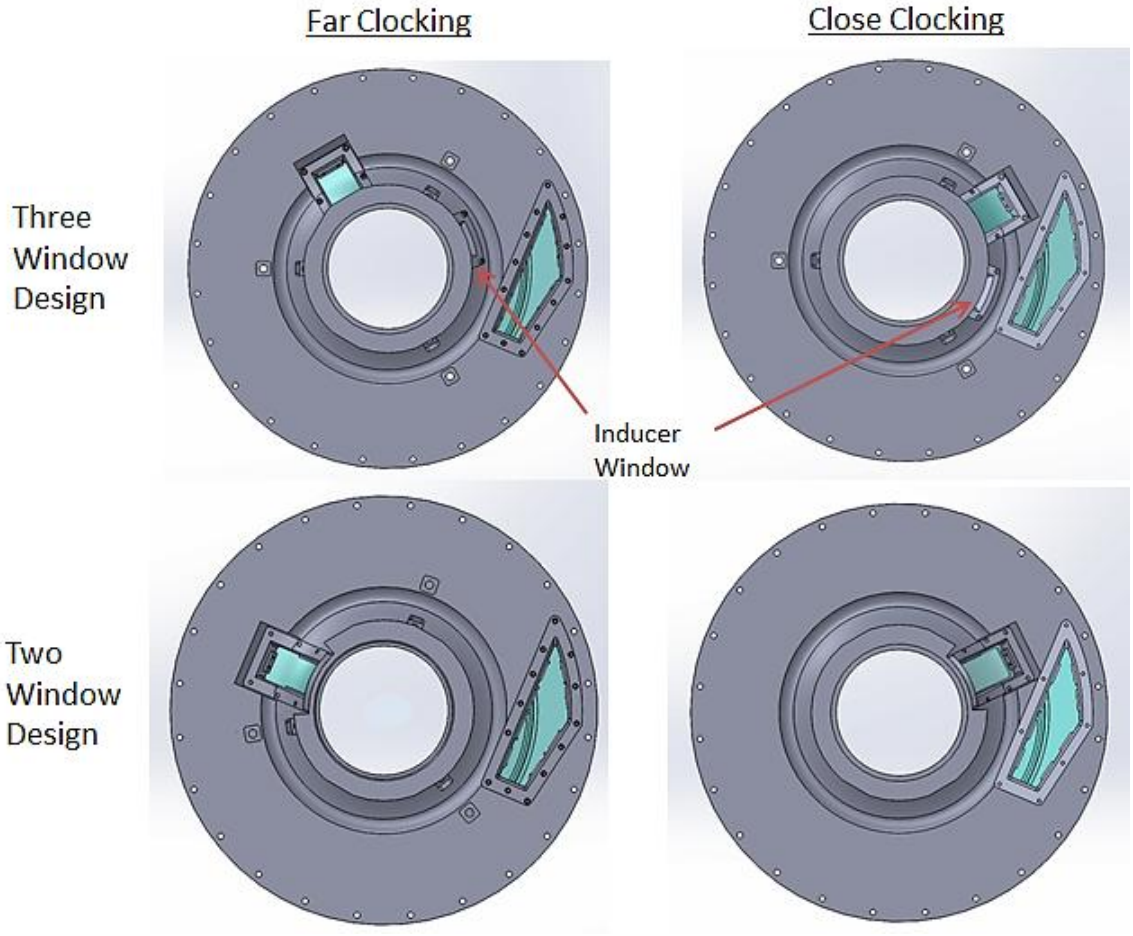

Figure 5.5: Far and close clocking configurations are depicted for both the three window and two window design.

The three window design consists of a close clocking mode with the inducer window clocked at 114 degrees from TDC and the knee window clocked at 60 degrees from TDC and a far clocking mode with the inducer window clocked at 70 degrees from TDC and the knee window clocked at 330 degrees from TDC. The diffuser window was clocked in the first quadrant of the shroud looking aft placing it in close proximity to both the inducer and knee windows in the close clocking mode. The methodology described previously was applied to the close clocking configuration and four locations were identified that exceed the +/- 0.001" deflection requirement. The locations of excess deflection at each of these radii are shown in Figure 5.6. Three of the locations occur in the inducer window and one occurs in the diffuser window. The deflection corresponding to these four locations was similarly measured in the far clocking configuration and compared. The difference in deflection between the modified geometry and the baseline geometry for each configuration were plotted in Figure 5.7. The plot indicates that the difference in deflection between the baseline geometry and the modified geometry is less at all four locations when the windows are clocked further apart. Only location 3 in the inducer window remains above the 0.001" limit; however, the extent to which it exceeds this requirement is only 7e-5 inches and will be considered negligible.

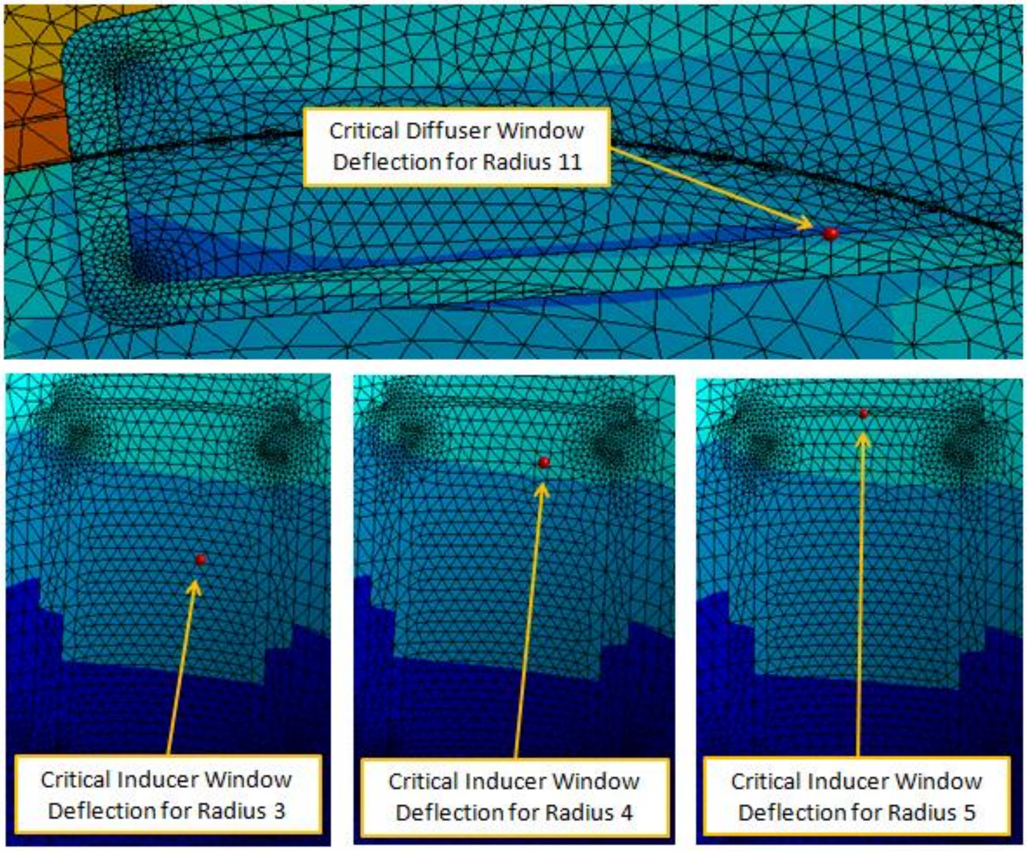

Figure 5.6: Locations of critical deflection for three window close clocking configuration.

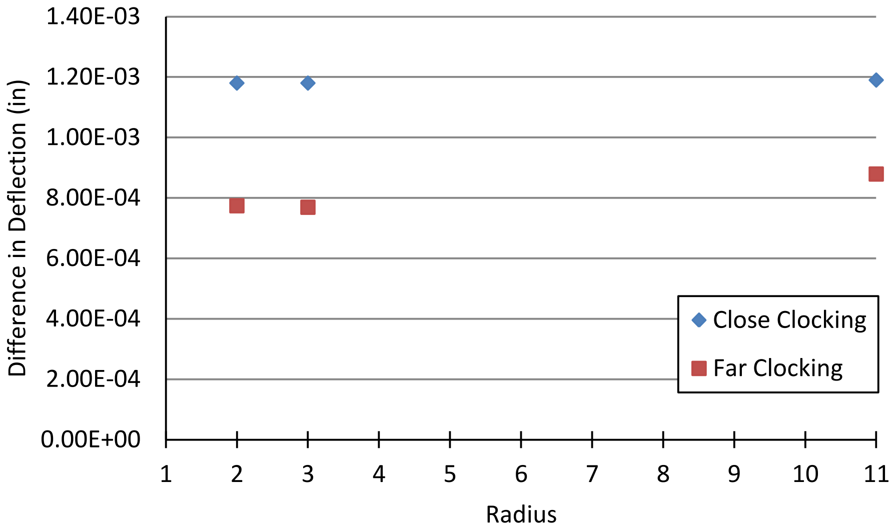

Figure 5.7: Difference in deflection between baseline and modified geometry at two clocking configurations for three window design.

Like the three window design, the clocking study for the two window design was performed for both a close and far clocking configuration. The close clocking configuration clocks the inducer/knee window at 64 degrees from TDC which is in close proximity to the diffuser window. The far clocking configuration clocks the inducer/knee window at 293 degrees from TDC which is much further from the diffuser window. Using the methodology described previously, three locations were identified in the close clocking configurations that exceed the +/- 0.001" deflection requirements. Two of these locations occurred in the inducer/knee window and one of these locations occurred in the diffuser window, refer to Figure 5.8 for an illustration of these points of deflection. These three critical points were then measured in far clocking configuration and both sets of deflections were plotted in Figure 5.9. The plot indicates a substantial drop in the difference in deflection between the baseline geometry and the modified geometry when the inducer/knee window is clocked further from the diffuser window. By clocking the inducer/knee window further from the diffuser window, the differences in deflection between the baseline geometry and the modified geometry all fall within the deflection requirements.

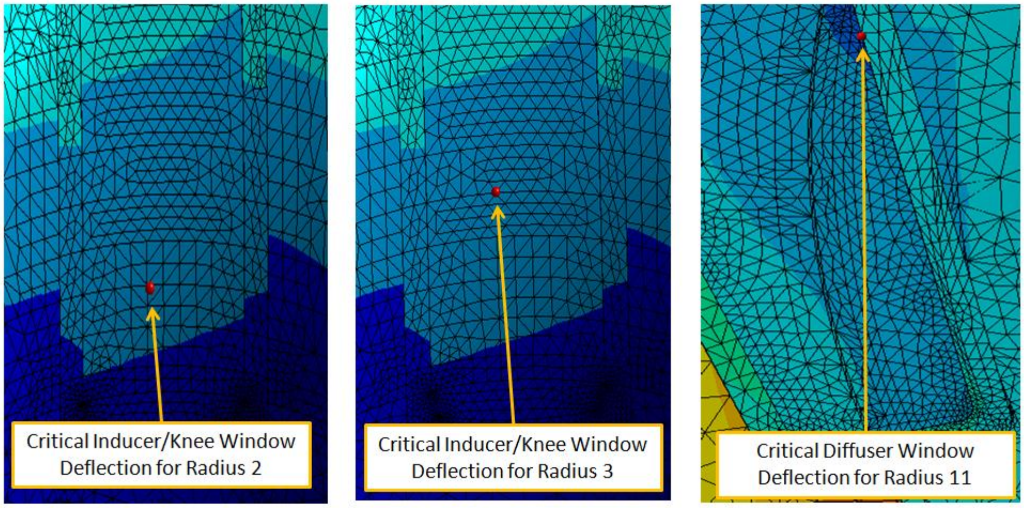

Figure 5.8: Critical deflection locations for two window close clocking configuration.

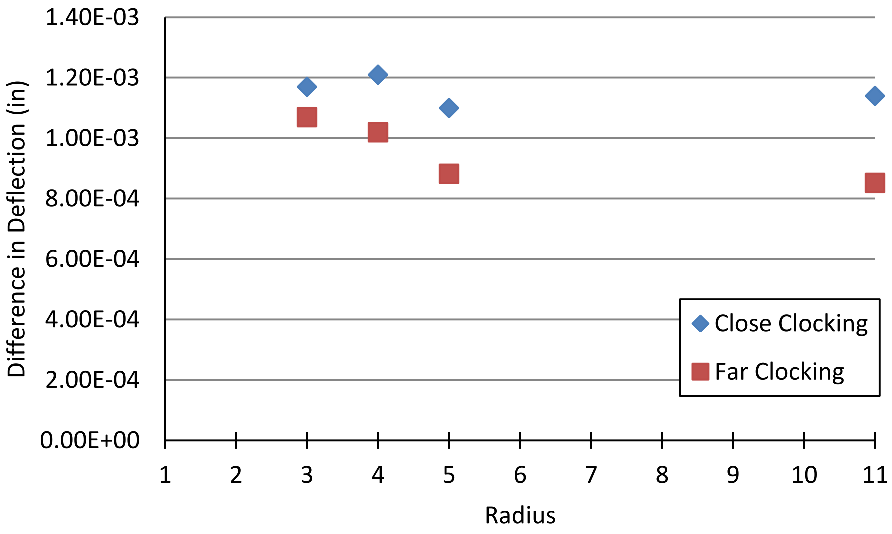

Figure 5.9: Difference in deflection between baseline and modified geometry at two clocking configurations for two window design.

The two different clocking studies indicate that clocking the windows further from each other is optimal and will aid in dampening the deflection that results from the addition of optical access to the shroud. An added benefit to clocking the windows further from each other is the increase in design space that it offers. This permits more room for the development of window holder flanges, allowing fastener heads to be fully seated on the flange, more properly securing the window holder to the shroud.

5.4.3 Window Width

The width of the window determines the angle the two LDV probes are able to collect measurements at. Measurements obtain at wider angles will result in a reduced relative error when transforming the velocity measurements to a three component coordinate system. Unfortunately, to incorporate larger windows more material must be removed from the shroud which might weaken it. To determine the optimal width that would reduce the relative error of the LDV measurements without weakening the shroud, several window widths were simulated.

Window width iterations were performed on the three window far clocking configuration to determine whether a larger factor of safety in deflection might be obtained if slightly narrower windows were employed, mainly at location 3. Three window holder widths were tested; 1.5", 1.75", and 2". Locations 4, 5, and 11 were also monitored to compare the change in deflection from window width alterations at different locations. The difference in deflection at the three window holder widths are plotted in Figure 5.10.

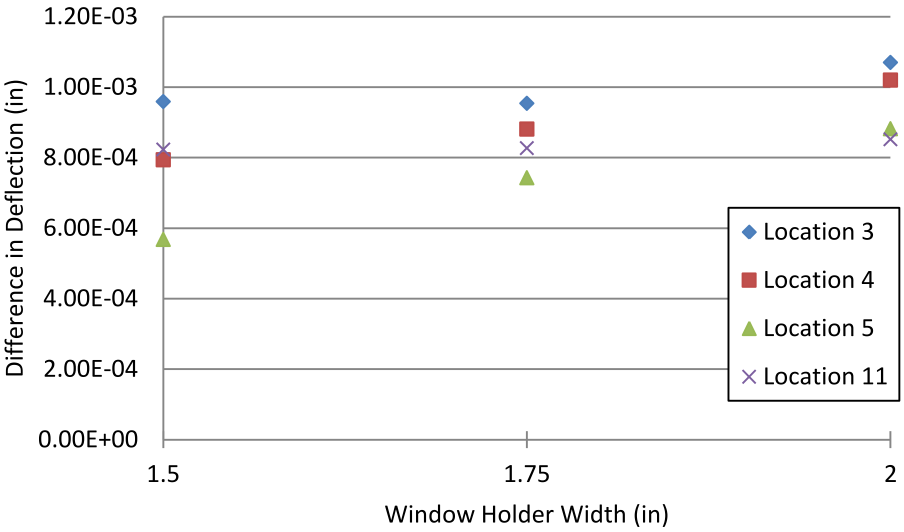

Figure 5.10: Window width iterations.

Simulating the windows at three different widths reveals that changes in deflection at location 3 and 11 are subtle while locations 4 and 5 seem to be more affected by window width. Because the diffuser width was not iterated on, the subtle change in deflection at location 11 and independence from the inducer and knee window width iterations is expected. Locations 3, 4, and 5 range from the middle of the inducer window to the trailing edge of the inducer window. The window width study would suggest that locations near the trailing and leading edges of the windows such as locations 4 and 5 are more affected by varying window width than areas near the middle of the windows such as location 3. Because this window study indicates that the deflection at location 3 will not be significantly improved by varying window width, it is recommended that 2 inch wide window assemblies be used due to the advantages offered by the increased LDV probe access that is contributed to wider windows.

5.4.4 Window Thickness

The thickness of the windows will determine how much the probe beams will refract. If the windows are thicker, the beams may refract too much and aligning the lasers will be more challenging. Thinner windows are optimal for reducing refraction of the lasers; however, thinner windows are less robust and may incur excessive deflection and stress. To determine the optimal window thickness several thicknesses were explored for each window ranging from 0.13”-0.2”.

For both the 3 and 2 window designs, the radii pertaining to the greatest deflection of each window were tracked for varying window thickness. These locations are shown in Figure 5.11. The difference in deflection at each of these points was collected from various simulations and plotted against the respective window thickness. The difference in deflection for each window at varying window thickness is plotted in Figure 5.12

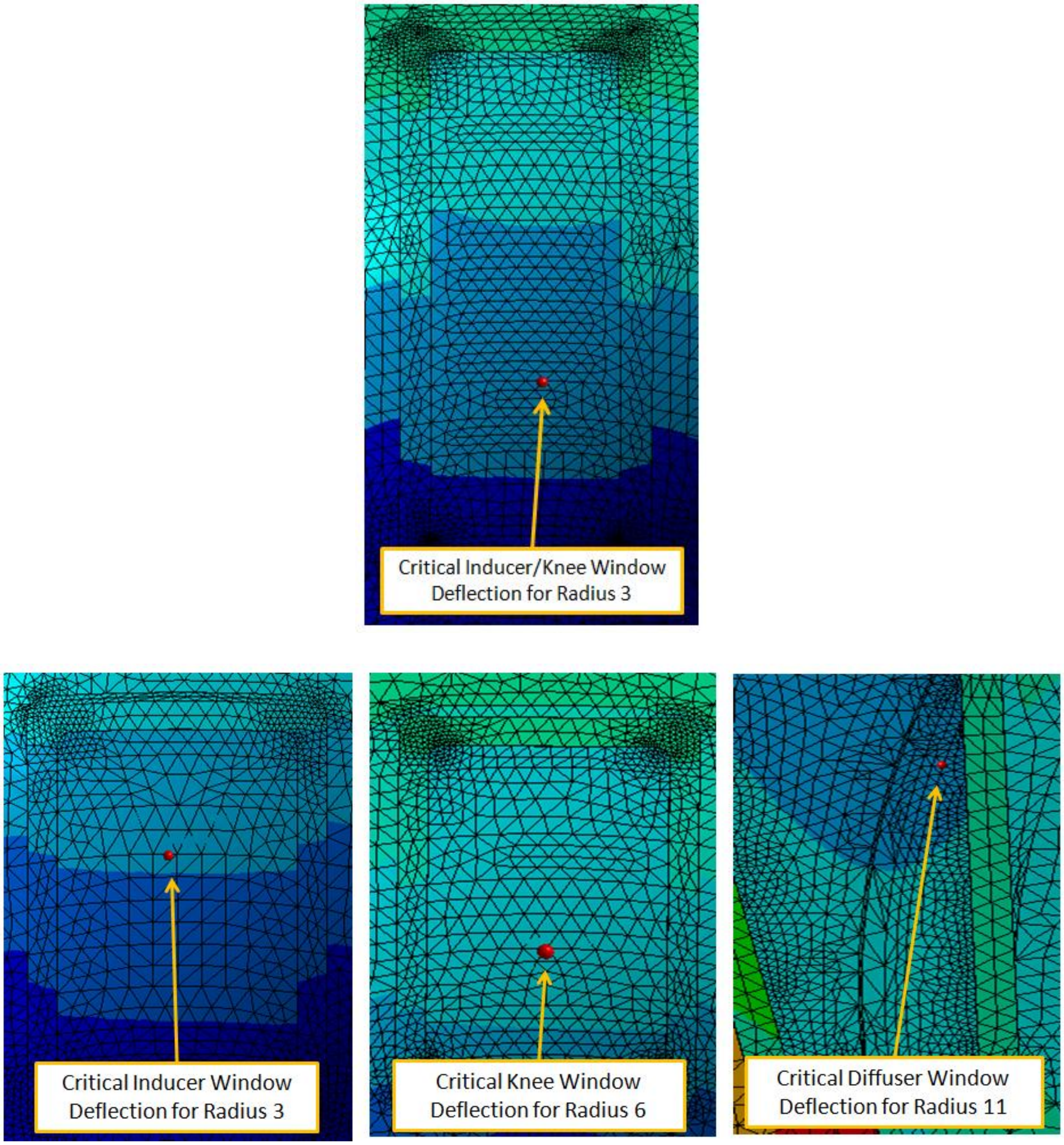

Figure 5.11: Critical locations of deflection for the inducer/knee, inducer, knee, and diffuser window.

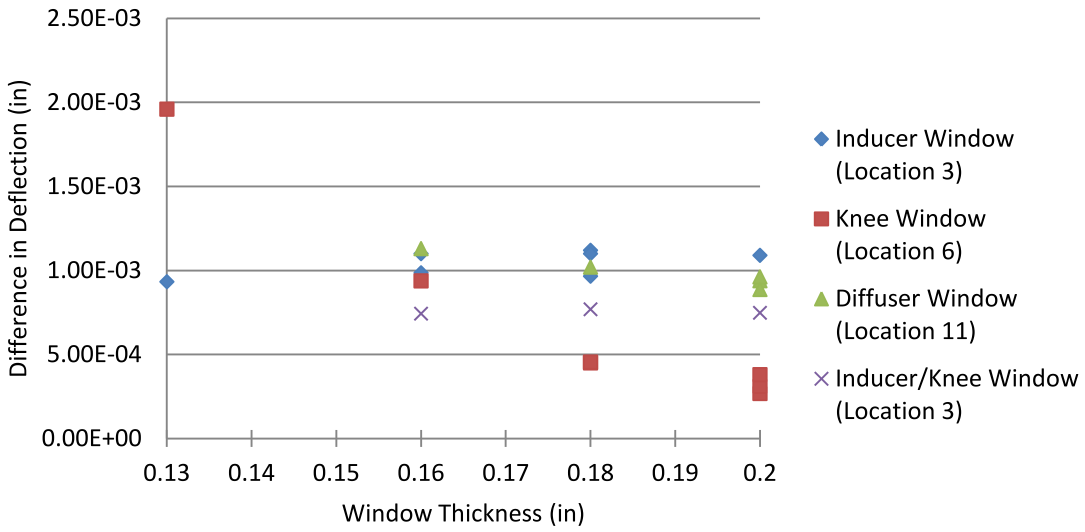

Figure 5.12: Window thickness iterations for all four window designs.

The difference in deflection for each window design at varying window thickness is plotted in Figure 5.12. The difference in deflection in the inducer area remains fairly constant for varying window thickness, with an average value of 1.04e-3 inches for the inducer window and 7.53e-4 inches in the inducer/knee window. The inducer and inducer/knee windows' independence from window thickness likely stems from the low temperature and low pressure conditions that occur at the inlet of the compressor and has low loading. The reason that the inducer window still maintains a 1.04e-3 inch deflection despite the low loading conditions is most likely due to general deformation from the other two windows that manifest itself in that area of the shroud.

The knee and diffuser windows, however, do not show an independence from window thickness. As the thickness of each window is decreased the windows deflect more at the critical deflection points. The increase in outward deflection of the knee and diffuser window is the result of deformation of the window material due to the higher pressures that occur deeper in the compressor. In the knee window the deflection limit occurs when the window is 0.16 inches thick and in the diffuser window that limit occurs for a window thickness of 0.18 inches.

Based off of the results from the window thickness study, the following conclusions can be made. The final inducer, knee, and inducer/knee window design will meet deflection requirements as long as the window thickness is 0.16" or greater. The diffuser window design will meet deflection requirements if the window is 0.18" or thicker. Factoring in a degree of safety, it is recommended that the final window design feature a 0.18" window thickness for the inducer, knee, and inducer/knee windows and a 0.20" window thickness for the diffuser window.

5.4.5 Window Stress

The stress on the windows was monitored in addition to the deflections and must have a safety factor of at least 1.25 with respect to the material yield stress. As stated in Table 5.1, the stress of the windows in the final design must have a tensile stress less than 5,600 psi and a compressive stress less than 128,000 psi. Additionally, the equivalent stress in the shroud and window holders must be less than 105,600 psi. The equivalent stress of the shroud and window holders for the three window and two window designs is depicted in Figure 5.13. The equivalent and maximum principal stresses are illustrated in Figure 5.14, Figure 5.15, Figure 5.16, and Figure 5.17 for each of the four different windows. Because the window thickness study suggests that windows with a thickness less than 0.16 inches would not be ideally suited for use in this centrifugal application, 0.16 inches windows were chosen to validate the stress in the overall LDV window design.

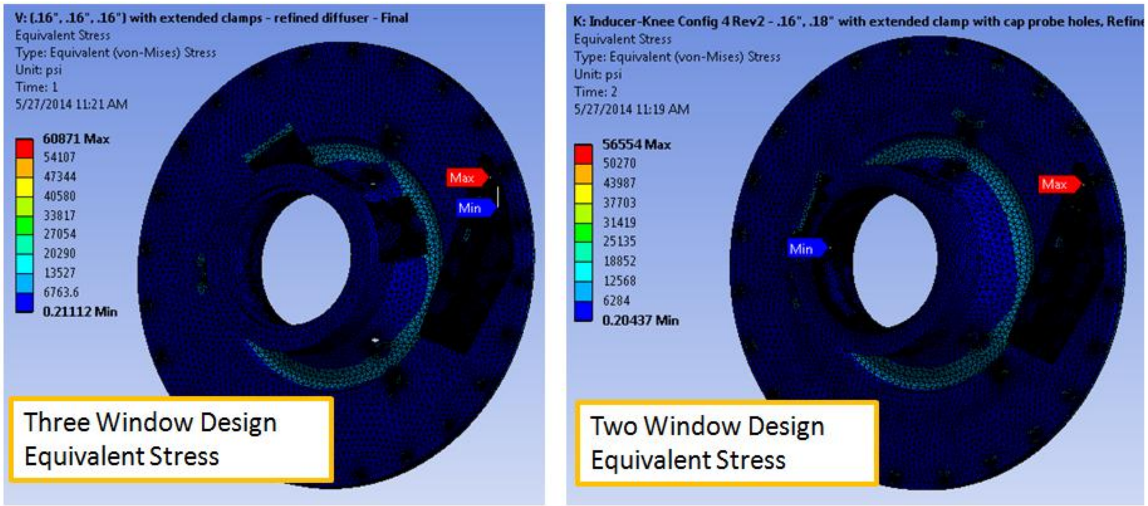

Figure 5.13: The equivalent stress for the shroud and window holders for both the three and two window designs.

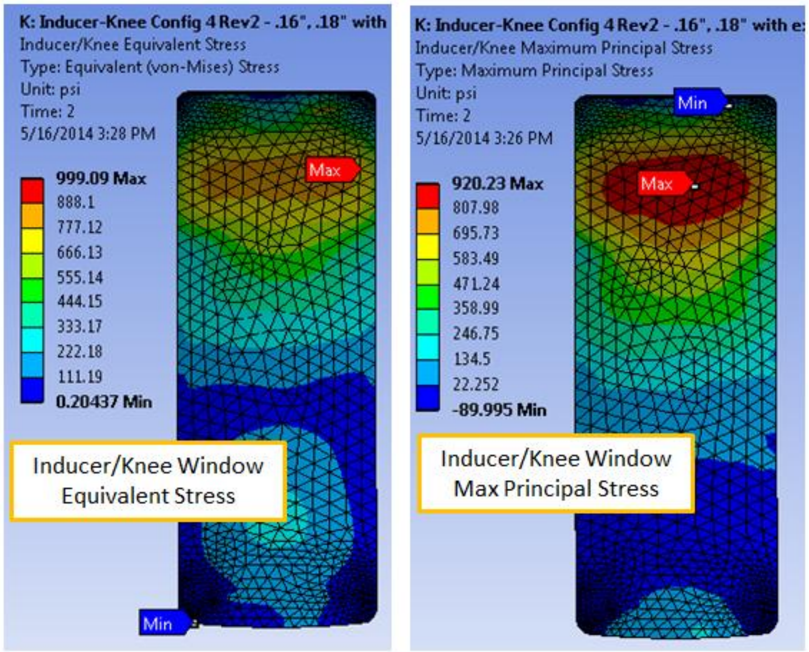

Figure 5.14: Equivalent and max principal stress in the inducer/knee window at a thickness of 0.16”.

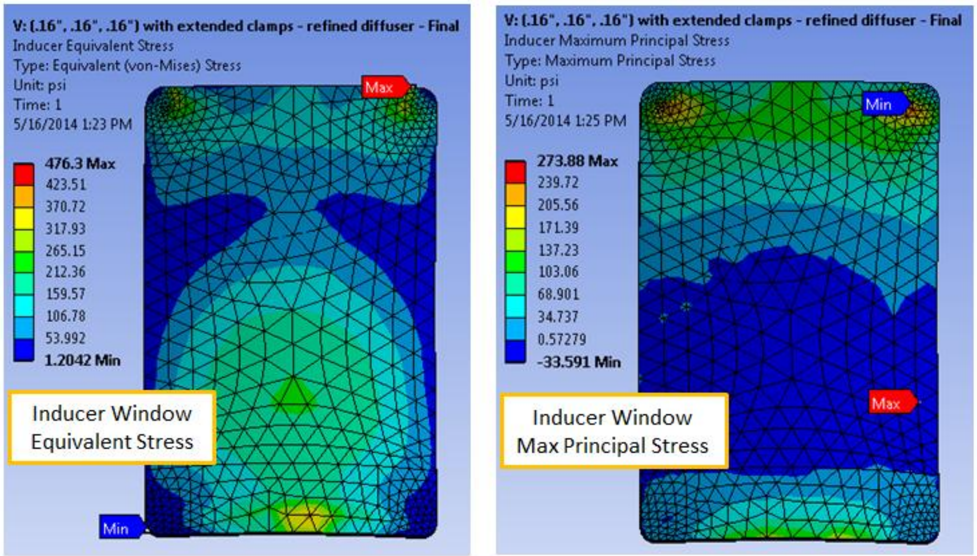

Figure 5.15: Equivalent and max principal stress in the inducer window at a thickness of 0.16”.

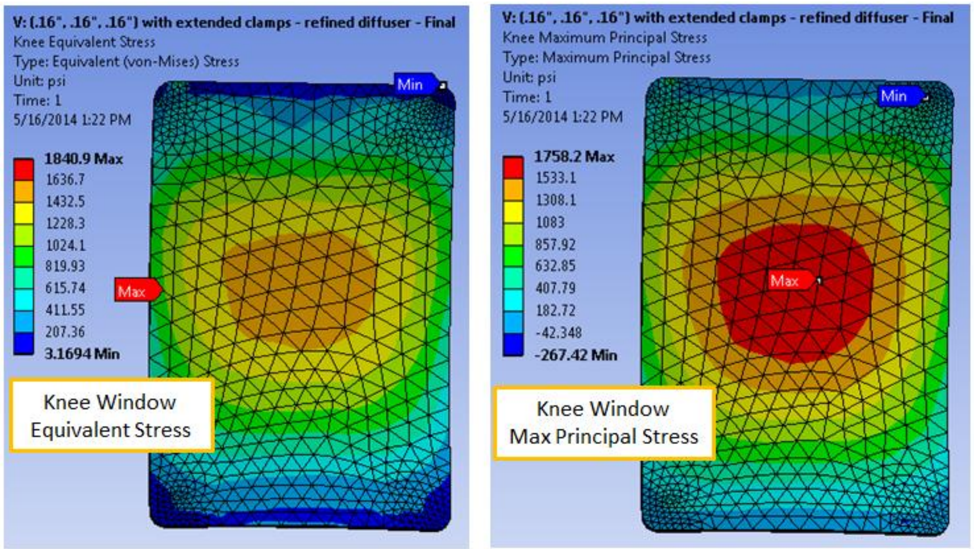

Figure 5.16: Equivalent and max principal stress in the knee window at a thickness of 0.16”.

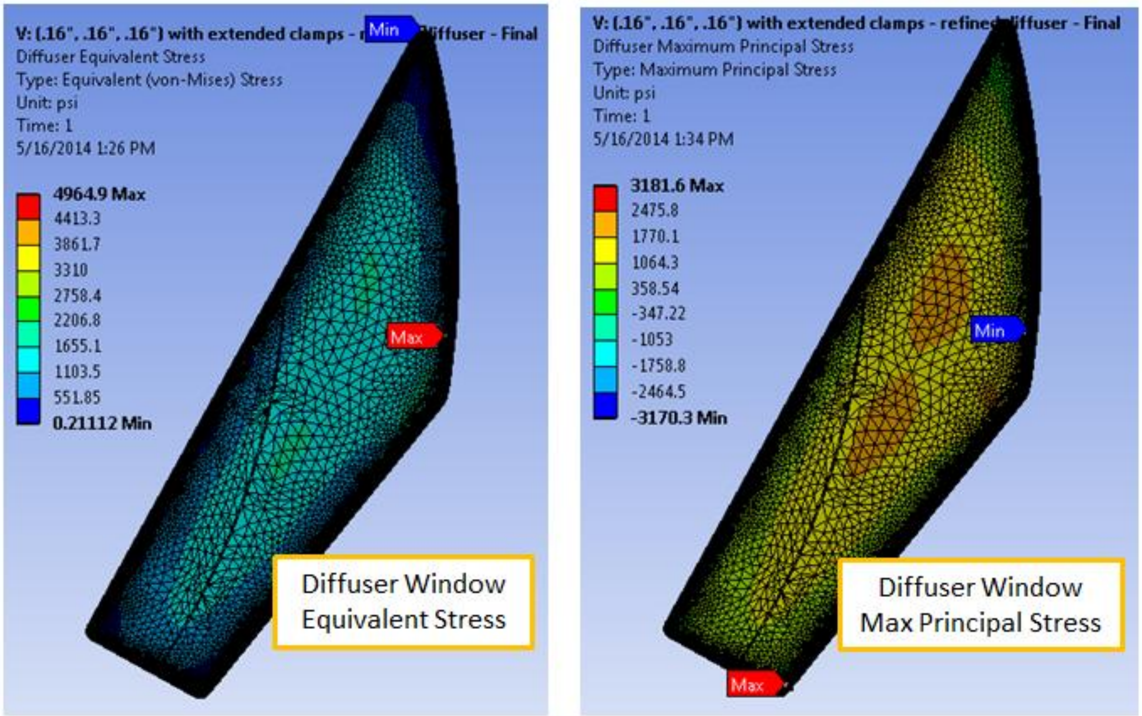

Figure 5.17: Equivalent and max principal stress in the diffuser window at a thickness of 0.16”.

The safety factors for the LDV window designs are tabulated in Table 5.3. The stress in the shroud and window holders for both the two and three window designs is below the required 105,600 psi limit. For each window, as depicted in the stress maps, the equivalent stress is well under 128,000 psi indicating that the windows are limited primarily by the maximum principal stress requirement. As shown in Table 5.3, the maximum principal stress is below the required 5,600 psi limit for each window at a thickness of 0.16". Because the stress in each window at 0.16 inches is within the design stress requirements, it is assumed that any windows featuring thicknesses larger than 0.16 inches will also maintain a stress that is within the design requirements.

Table 5.3: Safety factors for the shroud, window holder, and window designs.

Combined Shroud and Window Holder Stress		
Design	Max Equivalent Stress (psi)	Safety Factor
Three Window	60871	2.2
Two Window	56554	2.3
Window Stress		
Component	Maximum Principal Stress (psi)	Safety Factor
Inducer/Knee	920	7.6
Inducer	273	25.6
Knee	1758	4.0
Diffuser	3181	2.2

CHAPTER 6 : CONCLUSIONS

6.1 Overview

In the future, more efficient gas turbine engines will be required to meet consumer demands for higher performance at lower specific fuel consumption. To meet these requirements, a need exist for compressors that feature higher overall pressure rises with larger power-to-weight ratios.

One method of meeting these demands is to improve the performance of the axial compressors used in modern gas turbine engines. Axial compressors perform best at high specific flow with low head rise; however, in the rear stages of an axial compressor an increase in relative tip clearance and a lower specific flow impede this performance. Because centrifugal compressors are less susceptible to endwall loss and more suitable for low specific flows, the performance of an axial compressor can be improved by adding a centrifugal compressor as the last stage.

The performance of the centrifugal compressor depends heavily on the fluid interactions occurring within the impeller and diffuser. These interactions are often complex and not well understood due to the high radial accelerations and tip leakage flows present in centrifugal compressors. Because of this, further research on the flow physics occurring inside the impeller and diffuser is critical to achieve better overall performance for these machines. In particular, the application of non-intrusive measurement techniques such as LDV is needed to provide a deeper insight into the fluid interactions that occur in centrifugal compressors. The primary focus of this research has been to develop optical access in the Purdue CSTAR compressor for the application of LDV.

6.2 LDV Window Design Overview

The final LDV window design presented includes two possible configurations. These configurations include a two window and three window design making up a total of four windows, Figure 6.1. Each of these designs meets the stress and deflection requirements set forth by the CSTAR sponsor.

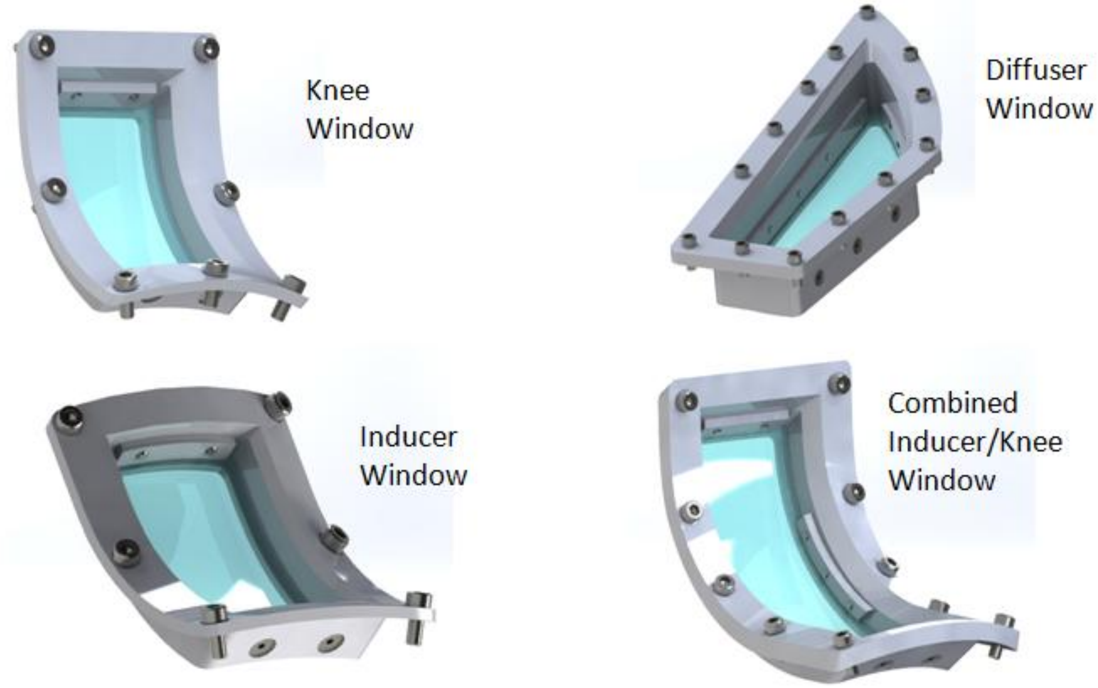

Figure 6.1: The final design for LDV optical access to the compressor includes the four window assemblies shown above.

Both the two window and three window designs permit access to various areas of the compressor from the inducer to the diffuser exit. In particular, the inducer, knee, and inducer/knee windows cover the impeller from the inlet to compressor knee. The diffuser window permits access of the diffuser vaned passages and the impeller exit. The windows were designed to allow maximum coverage of the compressor. Both of the proposed designs will provide coverage of approximately 85% of the impeller flow path. The optical access of both the inducer and knee windows is shown by the green volume in Figure 6.2. The optical access supplied by both these windows overlap each other to provide continuous coverage of the impeller. Alternatively, continuous coverage of the impeller flow path is supplied by the longer inducer/knee window design as shown in Figure 6.3. For both the two window and three window design the optical access granted by the diffuser window is shown in Figure 6.4.

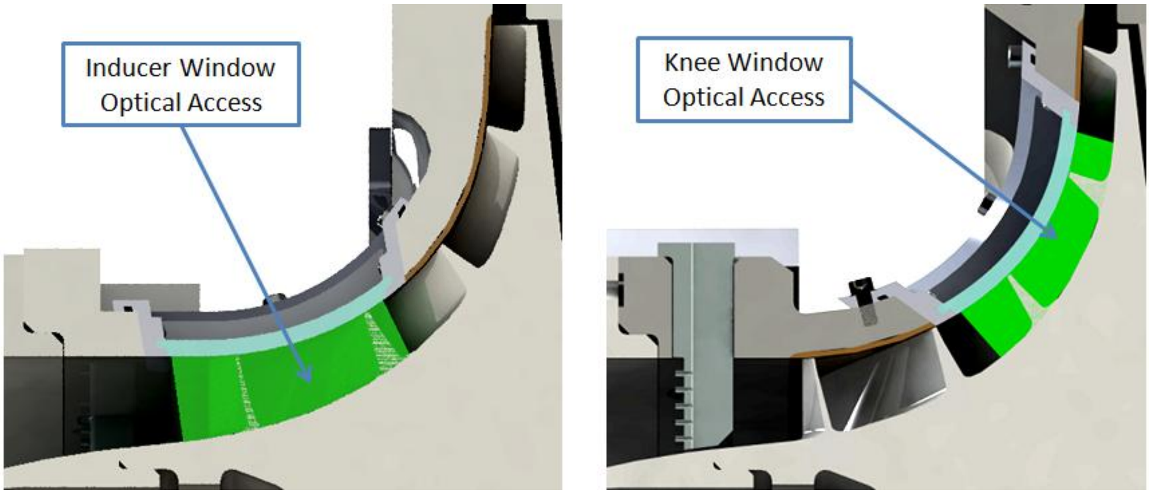

Figure 6.2: LDV optical access in the inducer and knee windows.

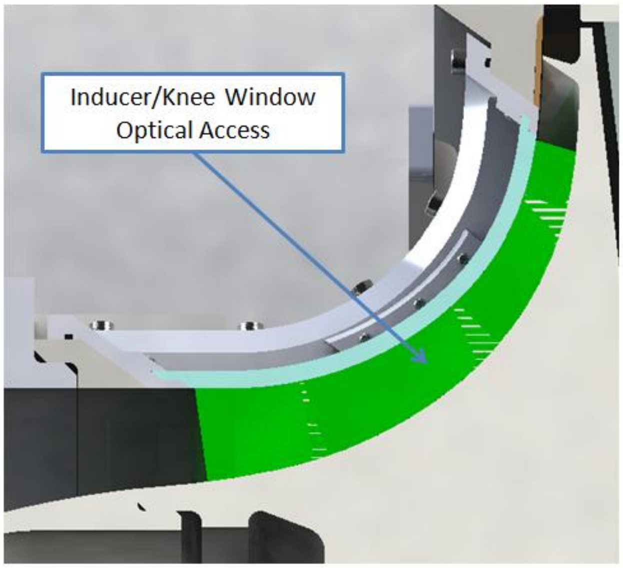

Figure 6.3: LDV optical access in combine inducer/knee window.

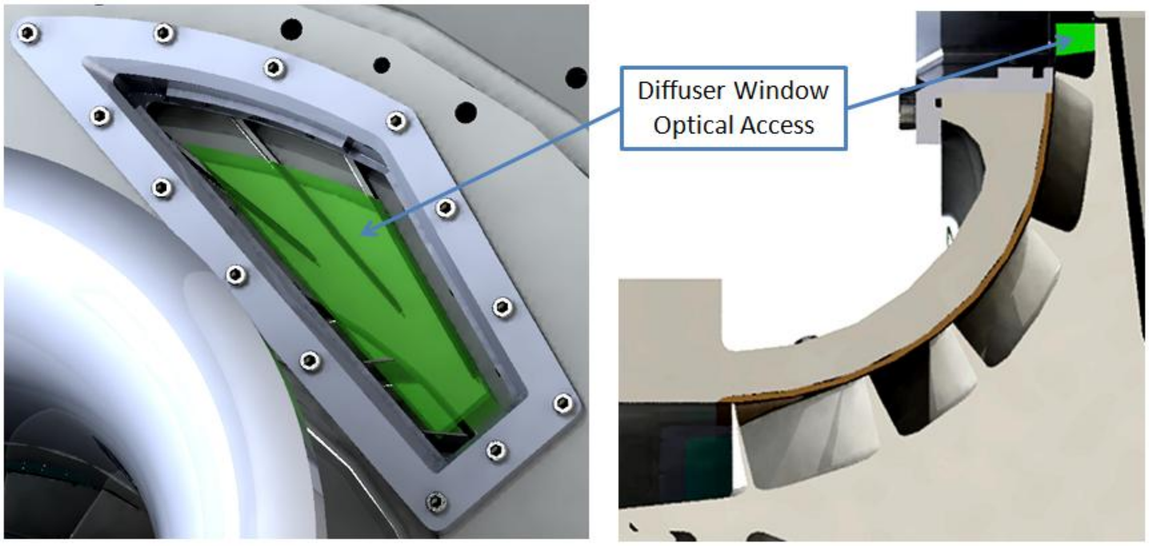

Figure 6.4: LDV optical access in diffuser window.

Each window was optimized to permit the LDV probes to obtain measurements at a large incident angle to reduce the relative error that results from transforming the measurements to a three component coordinate system. Because the blade height decreases from the impeller inlet to the exit, the probe clearance limitation, defined as the angle between the two axes of the two LDV probes, occurs for measurements taken at the hub in the upstream portion of the windows. For the inducer and knee windows this clearance limit is 54˚ and 64˚ degrees, respectively and for the combined inducer/knee window it is 56˚. In the diffuser window, there is no probe clearance limit; rather the clearance angle defines the resolvable upstream and downstream portions of the two vaned passages. Figure 6.4 shows the optical access for a probe clearance angle of 45˚ when the probe measurement plane is parallel to the center vane. The probe measurement plane is defined as the plane that contains the axis of each probe. Decreasing the probe clearance angle will allow more upstream and downstream coverage of the diffuser while increasing the angle will reduce the coverage.

6.3 Current Status of LDV Implementation

The two window design has been chosen to provide optical access to the centrifugal compressor. Though the mechanical design of the LDV windows is complete, several items must be resolved before the centrifugal compressor facility is prepared to obtain LDV measurements. First, a suitable manufacturer must be selected that can fabricate the complex geometry of the window assemblies to the level of precision required. Several vendors have already been identified. Manufacturers must also be selected that can fabricate a new shroud for the LDV windows, in addition to performing modifications to the existing diffuser.

Before LDV can be implemented, a ray tracing analysis must be performed to predict the amount of refraction that the probe beams will have due to the high level of curvature attributed to the inducer and knee. If the 0.18" thick windows distort the beams to a level where alignment is no longer achieved, the acquisition of a beam translator would be required to properly align the beams. Also, a traverse system must be established that will provide the LDV probes with a wide range of movement, allowing the system to easily adapt to the next point of measurement. Additionally, a mirrored system is recommended for diffuser window measurements to make up for the limited clearance offered between the inlet plenum and LDV probes for measurements made in the upstream portion of the window.

Finally, though Alumina is recommended to be used as the seeding material to obtain LDV measurements in the compressor, the method of introducing it to the flow must still be determined. In particular, an apparatus must be acquired that is capable of seeding the flow with the solid particles. The location that the seed particles are introduced to the flow must be decided as well.

LIST OF REFERENCES

LIST OF REFERENCES

[1] W. P. Gizzi, C. Roduner, D. Stahlecker, P. Koppel and G. Gyarmathy, "Time-resolved measurements with fast-response probes and laser Doppler velocimetry at the impeller exit of a centrifugal compressor: a comparison of two measurement techniques," *Proceedings of the Institution of Mechanical Engineers, Part A: Journal of Power and Energy,* vol. 213, p. 291, 1999.

[2] "Laser Doppler Anemometry," Massechusetts Institute of Technology, [Online]. Available: http://web.mit.edu/fluids-modules/www/exper_techniques/. [Accessed 3 January 2014].

[3] X. Ottavy, I. Trebinjac and A. Vouillarmet, "Treatment of L2F anemometer measurement volume distortions created by curved windows for turbomachinery applications," *Measurement Science and Technology,* vol. 9, no. 9, pp. 1511-1521, 1998.

[4] R. Schodl, "A Laser-Two-Focus (L2F) Velocimeter for Automatic Flow Vector Measurements in the Rotating Components of Turbomachines," *ASME Journal of Fluids Engineering,* vol. 102, pp. 412-419, 1980.

[5] I. Roehle, G. Karpinski and R. Schodl, "3-Component-Doppler-Laser-2-Focus: A new kind of three compnent velocimeter," in *Instrumentation in Aerospace Simulation Facilities, 1999. ICIASF 99. 18th International Congress on*, Toulouse, 1999.

[6] Z. Zhang, LDA Application Methods, New York: Springer-Verlag Berlin Heidelberg, 2010.

[7] S. Zaidi, "Practical Problems Associated with Laser Anemometry in High Speed Turbomachines," *SciVerse ScienceDirect Journals: Optics and Lasers in Engineering,* vol. 26, no. 6, pp. 473-486, 1997.

[8] M. Raffel, C. Willert, S. Wereley and J. Kompenhans, Particle Image Velocimetry: A Practical Guide, New York: Springer, 1998.

[9] M. P. Wernet, G. J. Skoch and J. H. Wernet, "Demonstration of a Stabilized Alumina/Ethanol Colloidal Dispersion Technique for Seeding High Temperature Air Flows," in *16th International Congress on Instrumentation for Aerospace Simulation Facilities*, Dayton, 1995.

[10] D. Eckardt, "Detailed Flow Investigations Within a High-Speed Centrifugal Compressor Impeller," *ASME Journal of Fluids Engineering,* vol. 98, pp. 390-402, 1976.

[11] D. Eckardt, "Instantaneous Measurements in the Jet-Wake Discharge Flow of a Centrifugal Compressor Impeller," *ASME - Journal of Engineering Power,* vol. 97, no. 3, pp. 337-345, 1975.

[12] D. Alder and Y. Levy, "A Laser-Doppler Investigation of the Flow Inside a Backswept, Closed, Centrifugal Impeller," *Journal of Mechanical Engineering Science,* vol. 21, no. 1, 1979.

[13] T. I. Allos and R. L. Elder, "Measurement of Flow Velocity in the Vaneless Diffuser of a High-Speed Centrifugal Compressor Using a Laser Doppler Anemometer," *International Journal of Optics,* vol. 27, no. 1, pp. 119-126, 1980.

[14] H. Krain, "A Study on Centrifugal Impeller and Diffuser Flow," *ASME Journal of Engineering for Power,* vol. 103, pp. 688-697, 1981.

[15] H. Krain, "Swirling Impeller Flow," *ASME Journal of Turbomachinery,* vol. 110, pp. 122-128, 1988.

[16] C. P. Hamkins and R. D. Flack, "Laser Velocimeter Measurements in Shrouded and Unshrouded Radial Flow Pump Impellers," *ASME Journal of Turbomachinery,* vol. 109, pp. 70-76, 1987.

[17] J. Fagan and S. Fleeter, "L2F and LDV Velocity Measurement and Analysis of the 3D Flow Field in a Centrifugal Compressor," in *AIAA/ASME/SAE/ASEE 25th Joint Propulsion Conference*, Monterey, 1989.

[18] M. D. Hathaway, R. M. Chriss, J. R. Wood, A. J. Wood and A. J. Strazisar, "Experimental and Computational Investigation of the NASA Low-Speed Centrifugal Compressor Flow Field," *ASME Journal of Turbomachinery,* vol. 115, pp. 527-541, 1993.

[19] G. J. Skoch, P. S. Prahst, M. P. Wernet, J. R. Wood and A. J. Strazisar, "Laser Anemometer Measurements of the Flow Field in a 4:1 Pressure Ratio Centrifugal Impeller," in *Turbo-Expo*, Orlando, 1997.

[20] S. Ibaraki, T. Matsuo, H. Kuma, K. Sumida and T. Suita, "Aerodynamics of a Transonic Centrifugal Compressor Impeller," *ASME Journal of Turbomachinery,* vol. 125, pp. 346-351, 2003.

[21] M. Schleer and R. Abhari, "Clearance Effects on the Evolution of the Flow in the Vaneless Diffuser of a Centrifugal Compressor at Part Load Condition," *ASME Journal of Turbomachinery,* vol. 130, pp. 031009-1, 2008.

[22] N. Bulot, I. Trebinjac, X. Ottavy, P. Kulisa, G. Halter, B. Paoletti and P. Krikorian, "Experimental and numerical investigation of the flow field in a high-pressure centrifugal compressor impeller near surge," *Proceedings of the Institution of Mechanical Engineers, Part A: Journal of Power and Energy,* vol. 223, p. 657, 2009.

[23] I. Trebinjac, N. Bulot and N. Buffaz, "Analysis of the flow in a transonic centrifugal compressor stage from choke to surge," *Proceedings of the Institution of Mechanical Engineers, Part A: Journal of Power and Energy,* vol. 225, p. 919, 2011.

[24] N. Buffaz and I. Trebinjac, "Detailed Analysis of the Flow in the Inducer of a Transonic Centrifugal Compressor," *Journal of Thermal Science,* vol. 21, no. 1, pp. 1-12, 2011.

[25] R. Mehta and P. Bradshaw, "Design Rules for Small Low Speed Wind Tunnels," *Aeronautical Journal,* no. Paper No 718, pp. 443-449, 1979.

[26] E. Laws and J. Livesey, "Flow Through Screens," *Annual Review of Fluid Mechanics,* vol. 10, pp. 247-266, 1978.

[27] R. M. Fleming, The Design and Performance of a Centrifugal Compressor Research Facility, Purdue University, 2010.